

# Engineering Plasmonic Hybridization toward Advanced Optical Sensors

Swagato Sarkar and Tobias A. F. König\*

The requirements for an optical sensor are high: the sensor should be reliable, quick, and simple, and all these features must be provided at ultralow fabrication costs. The requirements go even further, as the sensor may operate without an energy source, and nowadays, the sensor components should be recyclable. Today existing plasmonic concepts and advances in nanofabrication can meet these requirements. This review article describes the available nanoscale components and discusses their reasonable layout to obtain the sensing requirements. It is shown that combining photonic and plasmonic properties helps to get high sensitivity at low losses, where these hybrid modes with simple optical concepts are introduced. The current state of the art in developing lithographic nanostructuring and directed self-assembly to pave the way for future refractive index sensors is also used. By providing a guideline for advanced sensors, how the individual optical components can be used to create hybrid properties that can be realized cost-effectively are shown. The review article ends with a discussion on the perspectives for plasmonic hybridization sensors.

## 1. Introduction

It is evident from the recent pandemic that early sensor diagnosis is the key to rapid and effective treatment.<sup>[1]</sup> A future optical sensor may work like this: If a target molecule or virus is detected, the sensor's color readily changes from green to red, observable through the bare eyes. So far, plasmonic colorimetric sensors show the required spectral shift, requiring mostly

an optical detector for clear identification.<sup>[2]</sup> Theoretically, due to the high sensitivity, plasmonic particles are suitable for this application,<sup>[3]</sup> but the yield from synthesis is often low to detect a clear color contrast.<sup>[4]</sup> Couplings through particle aggregations could improve plasmonic colorimetric sensors, but at the price that the assemblies are unstable and can lead to incorrect results.<sup>[5]</sup> It is time to step back to keep as many optical and chemical parameters constant. Optical losses and robust scalability have so far prevented the breakthrough of such a simple device. The solution lies in the interdisciplinary research field of plasmonics. Remember, plasmonics is a dynamic branch of nanophotonics that encompasses the areas of physics (optics and photonics), chemistry (nanoscale colloids and surface modification), materials (nanofabrication and biodegradability), and engineering (upscaling and mass production). In a dielectric system, such as a resonant cavity or a waveguide, light propagates as waves with specific frequencies and spatial distributions. Photonic modes describe the various ways in which light can be confined or guided within such systems and are characterized by their spatial profile, polarization, and resonant frequencies. On the other hand, the core component of plasmonics related to metallic structures is the light–matter interaction through the coherent oscillation of its free electrons.<sup>[6]</sup> Under excitation with specific wavelengths, the near field at the interface drastically increases due to the significant localization of light energy through the coupling of the incident electromagnetic field with the oscillating charges on the metal surface. Such conditions result in plasmonic resonances, where the resonant modes are associated with specific field distributions and energy enhancements at the resonance frequencies. Two fundamental plasmonic modes are classified depending on the metal structure, such as nanosstructured or bulk: localized surface plasmon resonance (LSPR)<sup>[7]</sup> and surface plasmon polaritons (SPP).<sup>[8]</sup> LSPR modes are characterized by their ability to couple light into nanostructures efficiently, and SPP has the feature that the energy can efficiently propagate at the interface. Both modes share the common characteristic of having a near-evanescent field and are susceptible to changes in the resonance condition. The outstanding review articles by Homola<sup>[9]</sup> or Nuzzo et al.<sup>[10]</sup> best capture the significant impact of the plasmonic modes on the development of chemical and biological sensors. However, the effect is limited because

S. Sarkar, T. A. F. König  
 Leibniz-Institut für Polymerforschung Dresden e.V.  
 Hohe Straße 6, 01069 Dresden, Germany  
 E-mail: koenig@ipfdd.de

T. A. F. König  
 Center for Advancing Electronics Dresden (cfaed)  
 Technische Universität Dresden  
 Helmholtzstraße 18, 01069 Dresden, Germany

T. A. F. König  
 Faculty of Chemistry and Food Chemistry  
 Technische Universität Dresden  
 Bergstraße 66, 01069 Dresden, Germany

 The ORCID identification number(s) for the author(s) of this article can be found under <https://doi.org/10.1002/adsr.202300054>

© 2023 The Authors. Advanced Sensor Research published by Wiley-VCH GmbH. This is an open access article under the terms of the Creative Commons Attribution License, which permits use, distribution and reproduction in any medium, provided the original work is properly cited.

DOI: [10.1002/adsr.202300054](https://doi.org/10.1002/adsr.202300054)

of the strong radiation damping, which leads to a broad resonance spectrum. Dielectric resonance structures can be a solution because they show a sharp resonance feature but lack sensitivity. According to the plasmon hybridization model,<sup>[11]</sup> one can use both resonance's advantages and improve the sensor's performance.<sup>[12]</sup> However, matching the individual resonances given a desired mass production for optimal sensor performance is challenging. Thus, one needs a plasmonic concept and precise control in nanostructured fabrication over large-area to use the hybrid modes for sensing applications.

Soft and interfacial lithography is a reliable fabrication method for fabricating large-area plasmonic nanostructures.<sup>[13,14]</sup> This soft interference lithography works well for sub-100 nm applications: the lithographic patterns are transferred to a poly(dimethylsiloxane) mask. Then the metal can be deposited, or one can treat the pattern wet-chemically to obtain the desired plasmonic array. The review article by Odom describes the fabrication on a wafer scale impressively using metallic nanoholes, nanoparticles, and pyramid-shaped particles.<sup>[15]</sup> In a parallel development, wet chemical synthesis and targeted self-assembly have evolved, allowing defined plasmonic nanoparticles to be placed on surfaces in a selective and controllable pattern.<sup>[16,17]</sup> This self-assembly approach provides plasmonic patterns with defined sizes, shapes, and materials that can be efficiently scaled with soft lithographic templates to high precision.<sup>[18,19]</sup> This method can reliably arrange plasmonic particle chains on glass, polymer films, and semiconductors.<sup>[20]</sup> In addition, Yalcin's group shows that nanoparticles can be produced on an industrial scale in a roll-to-roll processing line.<sup>[21]</sup> With this research, they are paving the way for mass production. Another critical factor is the recent advances in electromagnetic modeling methods, which contribute to the optical concept's design, integration, and verification.<sup>[19]</sup> With little computational effort, one can compute highly symmetric nanoparticles and periodic structures using the Mie theory<sup>[22]</sup> or rigorous coupled-wave analysis<sup>[23]</sup> method. The computational cost increases significantly when the nanoparticles are arranged and embedded in complex geometries because numerical simulation methods such as finite-differences-time domain, finite element method (FEM), or boundary element method (BEM) are necessary. Once the structure is fixed, the sensitivity can be calculated by systematically changing the refractive index. The refractive index is affected by chemical and physical parameters, such as concentration, pressure, temperature, etc. If unique materials such as quantum emitters or electrochemical polymers come into play, the online refractive index database proves to be a very useful data source.<sup>[24]</sup> Especially the arrangement of defined semiconductor materials like titanium dioxide also allows guided modes to improve the sensor properties.<sup>[25]</sup> This break in symmetry through material interfaces shows that low-cost materials and nanostructuring are available. However, their practical design with low losses and high sensitivity is still in its infancy.

This review article addresses using photonic and plasmonic modes to improve the sensing properties. We introduce the basic plasmonic modes and explain how sensitivity benefits from coherent modes such as plasmonic hybridization, where the resonant modes corresponding to individual nanostructures (plasmonic or photonic) couple together due to proximity or specific configuration, forming new hybridized modes with altered prop-

erties. We present this development considering plasmonic concepts and fabrication methods to target a reliable, fast, simple, low-cost sensor. We believe one can achieve high optical quality only if one uses direct writing techniques and self-arrangement methods. Furthermore, we focus on the substrate properties and explain their additional contribution to plasmonic hybridization and sensing properties. The review concludes with an outlook on transitioning from plasmonic to photoluminescent materials and their potential for advanced optical sensors.

## 2. Optically Excited Resonances for Advanced Sensing Application

An optical sensor operates based on different resonance mechanisms broadly classified as photonic or plasmonic. Here we have confined our review to four fundamental modes that can be inter-coupled to realize several advanced sensing schemes. These are shown in the inner circle of **Figure 1** as Rayleigh anomaly (RA) associated with periodic photonic structures, LSPR occurring in isolated metallic nanostructures, guided mode resonances (GMR) generated in grating-waveguide structures, and surface plasmon polaritons (SPP) appearing at metal-dielectric interfaces. For more than three decades, numerous researchers have explored these fundamental resonances where a change in chemical and physical parameters, such as pH,<sup>[26,27]</sup> temperature,<sup>[28,29]</sup> pressure,<sup>[30,31]</sup> strain,<sup>[32,33]</sup> humidity,<sup>[34,35]</sup> electrical conductivity,<sup>[36,37]</sup> and material compositions,<sup>[38,39]</sup> have been quantitatively identified. In most cases, spectroscopy-based investigations demonstrate a shift of the resonant wavelength ( $\Delta\lambda$ ) for such changes where optical readout systems with specific resolutions can calculate the device sensitivity ( $S = \Delta\lambda / \Delta X$ , where  $S$  is the generalized sensitivity and  $X$  are the physical parameters varied, such as temperature T, pressure P, strain L, etc.). The working principle behind the optical sensing mechanism is quite upfront; the resonant wavelength of an optically resonating element, along with its specific field distribution, is directly dependent on its structural and material parameters, changing of which results in this  $\Delta\lambda$ . In some instances, these chemical and physical parameters directly influence the optical refractive index of the surroundings ( $n$ ), affecting the resonance condition and, thus, allowing us to quantify the parametric sensitivity in terms of its refractive index sensitivity ( $S = \Delta\lambda / \Delta n$ ). Our review article focuses mainly on optical sensors and improving this RI sensitivity with a rational design. For details about the exact relationship between physicochemical parameters and refractive index, please refer to these reviews that highlight various types of optical sensors.<sup>[40–43]</sup>

Apart from the fundamental photonic and plasmonic resonances, recent studies have shown that combining these fundamental resonances can instigate different hybrid mechanisms; such hybridization is possible through plasmon-photon coupling, favored by specific engineered metallo-dielectric nanostructures, as shown in the outer circle of Figure 1. This hybridization model offers significant sensitivity improvements but involves additional physical tools to exhibit unique features. As a common platform for the review, we have concentrated mainly on planar devices decorated with periodic architectures that one can operate under normal and oblique incidence cases. Periodic nanostructures have an enormous role in photonics,<sup>[44]</sup> especially

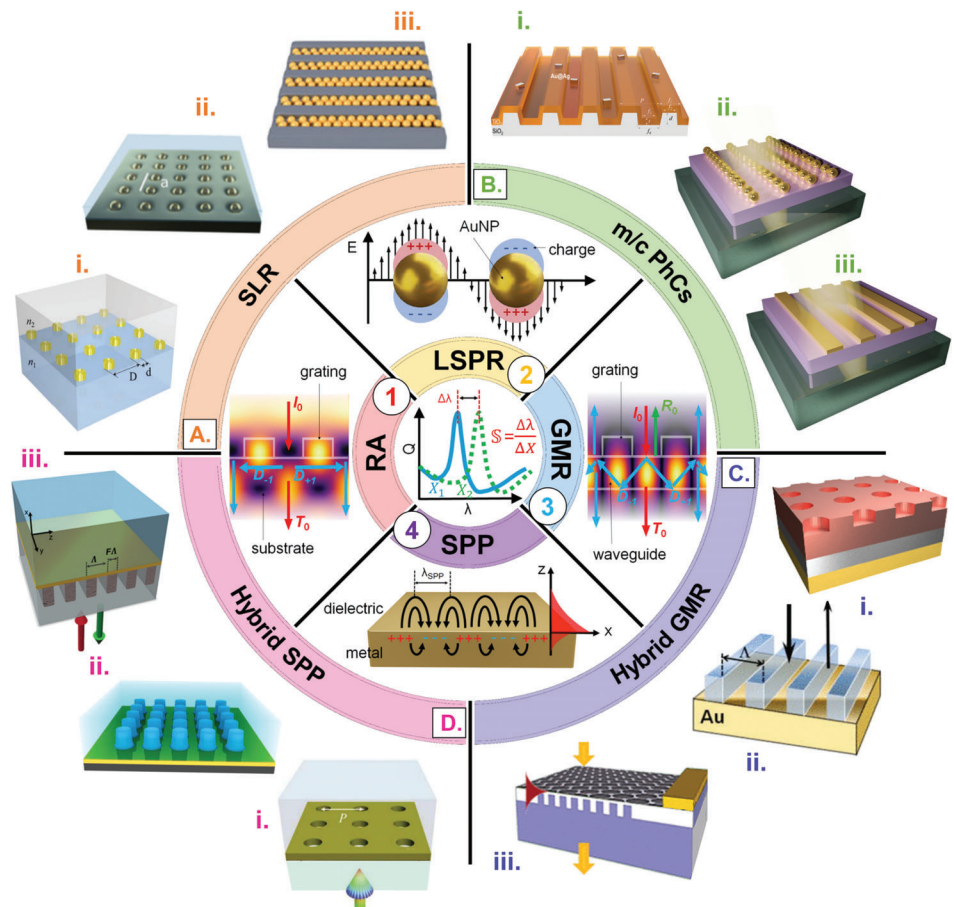


**Figure 1.** Enhanced sensitivity through the coherent coupling of fundamental modes for planar devices. The hybrid resonances results from these photonic (RA, GMR) and plasmonic (LSPR, SPP) modes. A) Surface lattice resonances in metallic lattices: A,i) 2D-array of gold nanodiscs resting on a dielectric substrate with matching cover index. Reproduced under the terms of the Creative Commons CC-BY license.<sup>[46]</sup> Copyright 2017, the authors, published by Optica. A,ii) 2D-array of gold nanoparticles embedded within a PDMS block. Reproduced under the terms of the ACS AuthorChoice License.<sup>[47]</sup> Copyright 2019, the authors, published by ACS. A,iii) 1D-array gold nanoparticles dimer chains within PDMS grating grooves. Reproduced under the terms of the Creative Commons CC-BY license.<sup>[48]</sup> Copyright 2022, the authors, published by Wiley VCH. B) Metallic/colloidal photonic crystal slabs: B,i) silver nanocuboids arranged over a dielectric 1D photonic crystal slab. Reproduced with permission.<sup>[49]</sup> Copyright 2020, American Chemical Society. B,ii) Gold nanoparticle chains on titania waveguide and B-iii) gold nanobars. Reproduced under the terms of the Creative Commons CC-BY license.<sup>[50]</sup> Copyright 2021, the authors, published by Wiley VCH. C) Hybrid guided-mode resonances: C,i) 2D-dielectric grating-waveguide structure with an underlying metallic layer. Reproduced with permission.<sup>[51]</sup> Copyright 2021, Elsevier B.V. C,ii) High-indexed dielectric grating with a sufficient thickness on a metallic surface. Reproduced with permission.<sup>[52]</sup> Copyright 2012, AIP Publishing. C,iii) Plasmonic waves in graphene by guided-mode resonances in a dielectric grating. Reproduced with permission.<sup>[53]</sup> Copyright 2012, American Chemical Society. D) Hybrid surface plasmon polariton resonances: D,i) 2D-nanohole array with asymmetric cover and substrate region. Reproduced under the terms of the Creative Commons CC-BY license.<sup>[54]</sup> Copyright 2021, the authors, published by Wiley VCH. D,ii) Low-indexed dielectric 2D pillar array on a metallic surface. Reproduced with permission.<sup>[55]</sup> Copyright 2020, Wiley-VCH. D,iii) Flat metallic surface with dielectric 1D grating embedded below. Reproduced with permission.<sup>[56]</sup> Copyright 2020, American Chemical Society. Sensitivity ( $S = \Delta\lambda / \Delta X$ ) is calculated as the ratio of change in wavelength and change in a physical parameter  $\Delta X$  ( $X = n, T, P, \dots$ ).

with the concepts of photonic crystal (which is the photonic analogous of semiconductors), offering photonic bandgaps (instead of electronic ones) for considerable significance in molding the flow of light at the nanoscale.<sup>[45]</sup> Under the broadband wavelength interrogation scheme, the pure and the hybrid sensors exhibit characteristic line shapes on the collection of the transmittance or reflectance, which are processed to calculate the change in resonant wavelength ( $\Delta\lambda_R$ ) to the external perturbations. Before proceeding with the plasmonic hybridization concepts, let's briefly overview the pure photonic and plasmonic counterparts of the hybrid geometries targeted in this review.

## 2.1. Basic Optical Resonances for Sensing

### 2.1.1. Diffraction Gratings as Building Blocks for Photonic Sensors

Periodic arrangements of alternating high-low refractive index profiles realized in a planar material constitute a grating structure. For reflected/transmittances collected from a dielectric 1D grating, certain discrepancies can be observed at two particular wavelengths, corresponding to the cover and substrate indices, often known as Rayleigh anomalies (RA). The physical origin is due to the re-distribution of incident energy corresponding to

a particular wavelength into grating orders, propagating parallel to the surface and coupling out. Beyond such wavelengths, the diffracted modes become evanescent, corresponding to the specific media. The RA leads to the modulation in reflection and transmission spectra in terms of sharp peaks/dips that can be useful for sensing purposes. Considering a generalized 2D-array, the occurrence of RA is given by,

$$\lambda_{RA, X} = \frac{\Lambda}{\sqrt{p^2 + q^2}} n_X \quad (1)$$

where  $p$  and  $q$  are the 2D-diffraction orders,  $\Lambda$  is the grating periodicity, and  $n_X$  is the refractive index of the diffracting medium, with  $X$  representing the cover or substrate. Therefore, for an asymmetric environment surrounding a high-indexed 1D grating, the RA at two interfaces (cover-grating and grating-substrate) corresponding to first-order diffraction following a normal incidence occurs at  $\lambda_{RA, C/S} = n_{C,S} * \Lambda$ . Typically for glass, the refractive index (RI) is considered to be  $\approx 1.5$ ; hence, for a 500 nm periodic 1D grating, the RA for cover and substrate occurs at 500 nm and 750 nm, respectively. The electric field profile at  $\lambda_{RA, S} = 750$  nm is shown in Figure 1, highlighting the diffracted orders propagating in the substrate. For a variation of the cover index through a change in analyte concentration, the  $\lambda_{RA, C}$  changes as per  $\Lambda * n_C$ . This setup is reported as a high-sensitivity refractive index sensor based on simple diffraction from phase grating.<sup>[57]</sup> Yet, the drawback of the RA mode lies in the exhibition of a peak/dip of lesser amplitude, resulting in spectral features of low contrast. The shortcomings of RAs in dielectric gratings for their application as a practical sensor can be uplifted by adding a metallic coating to enhance the spectral signal contrast towards RA-based sensing.<sup>[58,59]</sup> Although RA alone fails to offer impressive solutions for practical refractive index sensing, they constitute the basic building blocks for generating several hybrid modes. The cases of dielectric 2D hole-array, coated with a metallic layer, allow the coupling of propagating plasmon modes with the RA, leading to exciting features.<sup>[60]</sup> Also, generating surface lattice resonances (SLR) relies on the RA to assign high-quality (high-Q) photon modes to plasmonic nanostructures, where the Q is the measure of the energy storage and dissipation efficiency of the resonant system and is quantified by the sharpness or narrowness of resonance in terms of its bandwidth relative to its resonant wavelength ( $Q = \lambda / \text{FWHM}$ ; FWHM is the bandwidth defined by full-width at half maxima). These two cases will be discussed in detail in the upcoming sections. Besides such plasmonic encounters, RAs can coexist in dielectric grating-waveguide resonating structures and dielectric metasurfaces, resulting in sharp spectral features.<sup>[61,62]</sup>

### 2.1.2. Localized Field Enhancement and Improved Sensitivity by Metallic Nanoparticles

In metals, the incident light can cause the quasi-free conductance electrons at the interface to oscillate coherently. LSPR occurs when a surface plasmon is limited to a nanoparticle (NP) with a size equivalent to or smaller than the wavelength of light. The LSPR causes electric fields near the particle's surface to be strongly enhanced near the particle's surface, which gradually diminishes with increasing distance. The refractive index of the

surrounding medium determines the extinction peak, which has been mostly exploited to act as a refractive index sensor, as vividly described by Mayer and Hafner et al.<sup>[3]</sup> For a metallic nanoparticle, the respective polarizability ( $\alpha$ ) is defined as follows<sup>[7]</sup>

$$\alpha = 4\pi r^3 \frac{\epsilon_m - \epsilon_d}{\epsilon_m + 2\epsilon_d} \quad (2)$$

where  $r$  is the radius of the metallic nanoparticle, and  $\epsilon_m$  and  $\epsilon_d$  are the relative permittivity (dielectric constant) of the metal and the surrounding media, respectively.  $\alpha$  experiences a resonant enhancement for  $|\epsilon_m + 2\epsilon_d| = 0$ , leading to  $\text{Re}[\epsilon_m] = -2\epsilon_d$ , known as the Fröhlich condition that describes the dipole surface plasmon mode of the metal nanoparticle.  $\text{Im}[\epsilon_m]$  mainly influences the linewidth of the plasmonic resonance via damping of the oscillation. Exciting a metallic particle with an incident light beam thus results in scattering and absorption, expressed in terms of polarizability as:

$$C_{\text{sct}} = \frac{k^4}{6\pi} |\alpha|^2 = \frac{8\pi}{3} k^4 a^6 \left| \frac{\epsilon_m - \epsilon_d}{\epsilon_m + 2\epsilon_d} \right|^2; \\ C_{\text{abs}} = k\text{Im} [\alpha] = 4\pi ka^3 \text{Im} \left[ \frac{\epsilon_m - \epsilon_d}{\epsilon_m + 2\epsilon_d} \right]^2 \quad (3)$$

where the total extinction is given as  $C_{\text{tot}} = C_{\text{sct}} + C_{\text{abs}}$ . For metal nanoparticles, both absorption and scattering (and thus extinction) are resonantly enhanced at the dipole particle plasmon resonance, showing a maximum in the extinction spectra such that,

$$C_{\text{ext}} = 9k\epsilon_d^{3/2} V \frac{\epsilon_2}{|\epsilon_1 + 2\epsilon_d|^2 + \epsilon_2^2} \quad (4)$$

with  $V$  as the volume of the spherical nanoparticle, directly related to its radius  $r$ , and the complex dielectric constant of metal, expressed in terms of its real and imaginary parts as  $\epsilon_m = \epsilon_1 + i\epsilon_2$ . Equations (2) and (3) show that the dielectric constant of the surroundings, as well as the size and composition of the nanoparticle, have a substantial impact on the LSPR wavelength for which the near-field of the metal nanoparticle may also be significantly improved, in addition to obtaining the maximum optical extinction.<sup>[3,63]</sup> The LSPR wavelength can be approximately calculated for the visible and NIR wavelength using the Drude model:

$$\lambda_{\text{LSPR}} = \lambda_p \sqrt{2n_d^2 + 1} \quad (5)$$

where  $\lambda_p$  is the wavelength corresponding to the plasma frequency of the bulk metal and  $n_d$  is the RI of the surrounding dielectric media. Owing to the strong confining of light energy to nanoscaled volume, plasmon-enhanced light-matter interaction<sup>[64]</sup> has found a lot of applications in terms of photodetection,<sup>[65–67]</sup> photovoltaics,<sup>[68–70]</sup> photocatalysis,<sup>[71,72]</sup> as well as SERS signal enhancement.<sup>[73,74]</sup> Still, LSPR is widely renowned for its potential in sensing<sup>[75,76]</sup>; because of its simplicity in design and operation, overwhelming numbers of research have shown the structural and compositional aspects of LSPR sensing.<sup>[77]</sup> Indeed, LSPR sensitivity can be significantly tuned by choosing a suitable material (silver, gold, and alloys

using overgrowths<sup>[78]</sup>), shapes (rods, cubes,<sup>[79]</sup> stars,...), sizes, and other externally applicable fields.<sup>[80]</sup> Since many reviews already highlight LSPR-based sensors,<sup>[43,63,77,81]</sup> we have refrained from repeating them; instead, we want to highlight the hybrid mechanisms involved in advanced sensing with low-loss modes where spherical nanoparticles are considered constituent building blocks.

### 2.1.3. Resonant Grating-Waveguide Structures as a Functional Optical Element

Over the last three decades, diffraction gratings (discussed in Section 2.1.1) have been combined with waveguide structures to create biosensors due to their excellent integration ability and relatively high sensitivity in detecting analytes.<sup>[82,83]</sup> These grating-coupled sensors have been implemented in various configurations. With different materials, these structures achieve label-free detection by modifying the evanescent tail of a waveguide mode close to the interface.<sup>[84]</sup> The basic model of a guided-mode resonant system consists of a 1D dielectric grating placed on top of a dielectric planar waveguide, as shown in Figure 1. For a broadband incident source ( $I_0$ ), a portion of the light gets reflected as zeroth order ( $R_0$ ) while the rest gets diffracted as well as transmitted ( $T_0$ ). The first-order diffraction modes can be coupled to the propagating waveguide modes at specific resonant wavelengths ( $\lambda_R$ ) by choosing GMR structure parameters. This  $\lambda_R$ , while propagating inside the waveguide, can re-encounters the grating and get diffracted out in the directions of  $R_0$  and  $T_0$ .<sup>[85]</sup> The coupled-out waves interfere constructively/destructively to form a sharp resonant peak/dip, respectively. The basic grating diffraction equation,

$$n_w \sin \theta_w = n_c \sin \theta_c \pm p \frac{\lambda}{\Lambda} = n_g \sin \theta_g \pm p \frac{\lambda}{\Lambda} \quad (6)$$

comes from the conservation of momentum, where  $n_c$  and  $n_w$  are the cover and waveguide indices,  $n_g$  is the polarization-dependent average grating index,<sup>[86]</sup>  $p$  is the grating diffraction order,  $\Lambda$  is the grating periodicity, and  $\theta_{c/g/w}$  is the angle between the surface normal and propagation vector for the cover/grating/waveguide media. Following a 3-layered system (grating-waveguide-substrate), waveguiding is possible only for a narrow band of wavelengths that acquires integral multiple of  $2\pi$  phase change in a single round-trip,

$$\Phi_{\text{tot}} = 2\kappa_w d + \Phi_{w,s} + \Phi_{w,g} = 2\pi p; p = 0, 1, 2$$

$$\kappa_w = \frac{2\pi}{\lambda} (n_w^2 - n_{\text{eff}}^2)^{0.5}$$

$$\Phi_{w,s/g} = -2\tan^{-1} \left[ \left( \frac{n_w}{n_{s/g}} \right)^p \left| \frac{n_{s/g}^2 - n_{\text{eff}}^2}{n_w^2 - n_{\text{eff}}^2} \right| \right]^{0.5} \quad (7)$$

with  $n_{\text{eff}}$  is the effective index of the guided mode. The term ( $\phi_{\text{tot}}$ ) is the phase acquired due to the optical distance traversed by the diffracted light in one round trip.  $\phi_{w,s}$  and  $\phi_{w,g}$  are the phase shifts due to total internal reflection at the waveguide-substrate and waveguide-grating interface, respectively, with  $p = 0$  for the

TE and 1 for the TM polarization. So, among the diffracted orders corresponding to several wavelengths coupled inside the waveguide, only specific wavelengths ( $\lambda R \mp \delta \lambda / 2$ ) can propagate infinitely following the waveguiding condition;  $\delta \lambda = \text{FWHM}$ . The grating thus gets correlated to the waveguiding as  $n_{\text{eff}} = n_w \sin \theta_d$ , with regions of waveguiding given by the equation,

$$\max [n_s, n_g] \leq n_{\text{eff}} \leq n_w \quad (8)$$

As the grating-waveguide associated parameters are directly related to the resonant wavelength,<sup>[87,88]</sup> any physical change causing their variation results in the resonant peak/dip shift, thus allowing implementations as practical sensors.<sup>[89–91]</sup> A detailed review by Quaranta et al. discusses the latest developments in the field of GMR, including mathematical modeling, fabrication, and applications in sensing.<sup>[92]</sup> Interestingly, phase measurements using a monochromatic light source offer an extremely sharp variation between the resonance and off-resonance conditions, which can be utilized for ultrasensitive GMR sensors employing phase detection.<sup>[93]</sup> However, while considering the standard wavelength interrogation method, GMR sensors, despite their high-Q factors, have found lesser applications in sensing than LSPR-based sensors due to their overall low bulk sensitivity. Typically, >80% of the total optical power is confined within the waveguide region (instead of the cover) while applying such an evanescent wave-based detection method.<sup>[93,94]</sup> Instead, a low contrast grating layer with a larger aspect ratio and lower fill factor offers a highly sensitive resonant cavity mode,<sup>[95]</sup> operating on Fabry-Perot interference (FP-cavity). Geometries supporting FP-cavity modes have also been utilized for hybridization through LSPR incorporation.<sup>[96]</sup> Thus, one must associate plasmonic sensing capabilities through hybridization to impart higher sensitivities in dielectric grating-waveguide structures.<sup>[97]</sup> Using plasmon-photon coupling, the sensitivity can be enhanced by orders of magnitude while maintaining high-Q modes for improved resolution.<sup>[25]</sup>

### 2.1.4. Propagating Plasmonic Resonances in Metallic Thin Films

As discussed in Section 1.2, surface plasmons at metallic-dielectric interfaces are intensified surface fields generated through the collective oscillation of surface charges.<sup>[7,8]</sup> However, an essential requirement for the excitation of an SPP is the phase-matching conditions for the incoming light with the wave vector of the supported SPP mode; these can be executed using evanescent waves in the form of total internal reflection (TIR) in a prism,<sup>[8,98]</sup> waveguiding,<sup>[99]</sup> fiber grating coupling,<sup>[100]</sup> as well as through diffraction grating.<sup>[101,102]</sup> Compared to bulky prism-coupled SPP excitation architectures, compact grating-coupled SPP sensors in a single centimeter-sized chip offer advantage in establishing hand-held devices for rapid bio-detections.<sup>[103]</sup> For such grating-coupled SPP generation using a nanopatterned metal surface, the evanescent field corresponding to the higher diffracted order is coupled to the SPP modes at the metal-dielectric interface, producing resonant reflection dip.<sup>[104]</sup> A corrugated metallic layer surrounded by dielectrics can support

SPP modes at the two metal–dielectric interfaces, excited by the evanescent grating diffraction order, while following Equation (9)

$$k_0 n_{\text{inc}} \sin \theta_{\text{inc}} \mp \frac{m \cdot 2\pi}{\Lambda} = k_{\text{spp}} = k_0 \sqrt{\frac{\text{Re}(\epsilon_m) \cdot \epsilon_d}{\text{Re}(\epsilon_m) + \epsilon_d}} \quad (9)$$

here  $k_0$  is again the free-space propagation wavelength,  $n_{\text{inc}}$  is the refractive index of the incident medium,  $\theta_{\text{inc}}$  is the incident angle,  $m$  is the diffracted grating order,  $\Lambda$  is the grating period,  $\epsilon_m$  is the complex permittivity of the metal,  $\epsilon_d$  is the real permittivity of the surrounding dielectrics, and  $k_{\text{spp}}$  is the wave vector of the excited SPP mode. For developing SPP sensors with increased sensitivity, various nanostructuring, including nanohole array,<sup>[105–107]</sup> nanopillar with nanogaps,<sup>[108]</sup> metallic grating,<sup>[109]</sup> and metamaterial dispersive grating,<sup>[110]</sup> have been extensively demonstrated. Considering both wavelength and angular interrogation methods,<sup>[111]</sup> SPP sensors have the disadvantage of evaluating the resonance at the intensity minimum (low signal-to-noise ratio). In contrast, SPP signals can be locked much more effectively by implementing the phase-sensitive SPR setup that uses the zero-crossing phase signal.<sup>[112]</sup> In principle, this can also be applied to all plasmonic resonances.<sup>[113]</sup>

## 2.2. Plasmonic Hybridization Concepts for Nanostructures and Their Potential in Sensor Technology

Hybridization in nanophotonics has been of interest to researchers for an extended period. Particularly for plasmonic libraries, consisting of many nanostructures of different shapes, sizes, and morphologies, the distinct optical responses of the individual resonant blocks offer tailored applications that one can predict following theoretical considerations.<sup>[114,115]</sup> In particular, it is essential to predict responses from complex systems or assembled nanostructures that one can evaluate as a combination of the basic plasmonic units. Analogous to the molecular orbital (MO) theory, where atomic orbitals on individual atoms hybridize to form molecular orbitals, the LSPR modes of individual plasmonic blocks can also hybridize to create new hybrid bonding and antibonding modes. For the simplest case of MO theory (**Figure 2A-i**), 1s atomic orbitals of both hydrogen atoms contribute equally to the molecular orbitals of H<sub>2</sub>. The bonding molecular orbital is formed through a constructive interference of two atomic orbitals, resulting in reinforcement or the addition of their wave functions. This MO theory generates the σ<sub>1s</sub> orbital, which is the lower energy of the two molecular orbitals. The electrons in this orbital are primarily located in the space between the two nuclei that exerts attractive forces to stabilize the bond between the atoms and hold them together in a covalent bond. The antibonding molecular orbital σ\*<sub>1s</sub> orbital is produced when two atomic orbitals destructively combine, causing their wave functions to cancel out, resulting in a region of no electron density (node) between the nuclei, causing the energy of the orbital to increase.<sup>[116]</sup> Quite similarly, plasmonic bonding and antibonding modes can be predicted by bringing in a close analogy with the MO theory.<sup>[117]</sup> Figure 2A-ii introduces the hybridization picture where the resonant wavelengths for plasmonic nanoshells can be estimated from the fixed reso-

nant modes (described through charge distribution) of the constituent elementary geometries of a metallic sphere and spherical dielectric cavity.<sup>[11]</sup> Thus, for such nanoshells, the interaction between the nanosphere and nanocavity results in two new resonances: the lower energy symmetric or “bonding” plasmon and the higher energy antisymmetric or “antibonding” plasmons. In addition, multiple concentric metallic shell particles can also be explained by considering how the basic plasmon modes of the different surfaces of the metallic shells interact to form hybridized plasmons.<sup>[118]</sup> With existing knowledge, a complex hybridization model for nanoshells with nonconcentric cores and nanoshell dimers<sup>[119]</sup> can also be established.

In the cases of dimer structures, initial studies reveal the dependency of energy and excitation cross-sections on the interparticle distance between two spherical nanoparticles.<sup>[120]</sup> The comparison to the MO hybridization model can be even more straightforward for such dimers. The existing plasmonic modes can be considered as a result of combining the bonding and antibonding of the individual monomer’s resonant modes. For the case of a homodimer<sup>[115]</sup> (directly comparable to the case of an H<sub>2</sub> molecule), bonding or antibonding mode appears optically bright or dark<sup>[121]</sup> depending on the polarization state of the incoming light, resulting in either a red-shifted or a blue-shifted coupled plasmon mode.<sup>[122]</sup> However, for heterodimers with individual monomers of varied composition,<sup>[123]</sup> varied structural geometry,<sup>[124]</sup> or both,<sup>[125]</sup> the hybrid modes can both be bright, unlike the homodimer cases. The contributions of the monomeric unhybridized states to the hybridized forms of the heterodimers have also been theoretically established recently,<sup>[115,117,126]</sup> considering the interparticle distance and spatial orientations.<sup>[127]</sup> Further, hybridization between metallic nanoparticles and metallic surfaces is also considered,<sup>[127,128]</sup> highlighting the importance of surface separation for coupling localized particle plasmons and delocalized surface plasmons.<sup>[129]</sup> Apart from metallic surfaces, dielectric substrates induce hybridization of multipolar modes; silver (Ag) nanocube resting on the dielectric glass substrate can instigate interaction between bright dipolar and dark quadrupolar modes, resulting in a Fano-line shape.<sup>[130]</sup> These hybridized modes for nanoparticles in an asymmetric media are strongly dependent on the surrounding index,<sup>[131]</sup> thus becoming useful for LSPR-based sensing applications.<sup>[130]</sup> Overall, plasmonic–plasmonic hybridization has resulted in many significant applications, refractive index sensing being one of them. Nanoshells show a prominent redshift due to a change in the surrounding refractive index (1.00 to 1.63 leads to a spectral shift of ≈200 nm<sup>[133]</sup>) and have been utilized in biomedical applications.<sup>[134]</sup> Using FDTD-based simulation studies, Omrani et al. have examined how the plasmon hybridization mechanism impacts the refractive index sensitivity and performance of nanoshell, nanocage, and nano-frame structures.<sup>[135]</sup> An ultrahigh sensitivity of 1460 nm per RIU is obtained theoretically for optimized parameters of a nanocage structure, enhanced ≈5.5 times more than its solid counterpart. Such nanocage structures can be experimentally synthesized using galvanic replacement techniques<sup>[136]</sup> for biological sensing applications with potentially high selectivity.<sup>[137]</sup> Further, plasmonic hybridizations in a split ring stacking consisting of two gold split ring with orthogonal gap orientation along with a sandwiched dielectric (SiO<sub>2</sub>) disk spacer offer a sensitivity ( $S$ ) of 3024

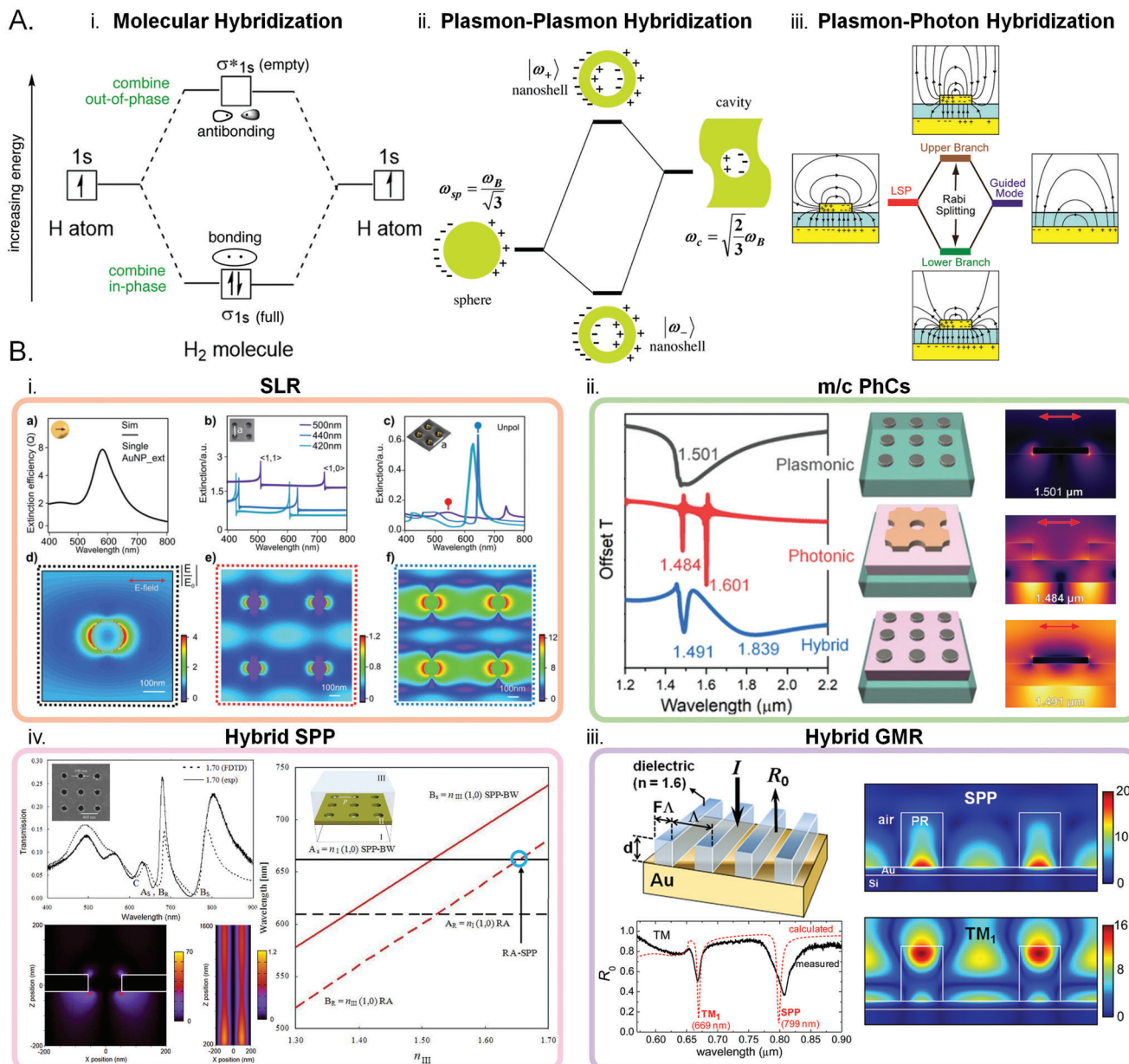


**Figure 2.** Plasmonic hybridization concepts in nanophotonics. A) Different schemes of hybridization energy diagram for (i) hydrogen molecule, (ii) plasmon-plasmon coupling in metallic nanoshells, and (iii) plasmon-photon coupling in 2D metal–insulator–metal cavity array. A,ii) Reproduced with permission.<sup>[11]</sup> Copyright 2003, The American Association for Advancement of Science. A,iii) Reproduced with permission.<sup>[132]</sup> Copyright 2013, American Chemical Society. B) Broad classification of plasmon-photon hybridization into four cases. B,i) Surface lattice resonance (SLR), shown as a combination of single particle localized resonance and lattice diffraction. The corresponding extinction spectra and resultant electric field distribution (normal-view) are shown in the top and bottom rows, respectively. Reproduced under the terms of the ACS AuthorChoice License.<sup>[47]</sup> B,ii) Metallic photonic crystal slabs showing the combination of plasmonic nanodisc resonance with photonic waveguided modes to generate hybrid modes. The transmittance and electric field distribution (cross-sectional view) are shown in the left and right columns, respectively. Reproduced under the terms of the Creative Commons CC-BY license.<sup>[97]</sup> Copyright 2022, the authors, published by Wiley VCH. B,iii) Hybrid guided mode resonances (hGMR) in a resonant element comprised of dielectric grating on a metallic surface. The reflectance spectra show a TM-like GMR mode and an SPP mode at two different resonant wavelengths where the nature of the modes can be distinctively identified from the cross-sectional electric field distribution. Reproduced with permission.<sup>[52]</sup> Copyright 2012, AIP Publishing. B,iv) Hybrid surface plasmon polariton (hSPP) in a metallic nanohole array with asymmetric indices for the substrate and cover region. Through the RI index variation of the cover region, the corresponding RA mode is matched with the SPP mode of the substrate, resulting in sharp peaks in transmittance. The cross-sectional electric field profile is shown at the resonance condition for forming the RA-SPP mode. Reproduced under the terms of the Creative Commons CC-BY license.<sup>[54]</sup> Copyright 2007, the authors, published by Optica.

nm per RIU with a figure of merit ( $FOM = S/\text{FWHM}$ ) of 1.4,<sup>[138]</sup> as calculated numerically. Note, that FOM is defined as the ratio of the sensitivity to the linewidth of the resonant mode and is used to evaluate the performance and capabilities of a sensor in terms of its sensitivity and detection efficiency. Despite the high sensitivity, the major drawback in both these structures is the operational wavelength ( $\approx 2.25 \mu\text{m}$ ) limiting its applicability in the visible optical range. In summary, the plasmonic hybridization concepts offer a refined and easier-to-understand explanation of plasmons and have proven to be a valuable tool in designing intricate metallic nanostructures with predictable resonances for various nanophotonic applications.

So far, the plasmonic hybridizations were related to resonances from isolated metallic nanostructures or non-interacting metallic nanoparticle arrays. While some of the LSPR offers extreme sensitivity,<sup>[76,77]</sup> one of the significant challenges is the intrinsic losses associated with metallic nanostructures due to strong radiative damping<sup>[3]</sup> and shorter plasmon lifetimes (2–10 fs).<sup>[139]</sup> Such losses result in broad FWHM of the line shapes ( $> 50 \text{ nm}$ ), implying low quality ( $Q \approx 1/\text{FWHM}$ ) factor of the resonant modes. Hence, these LSPR-based refractive-index sensors possess a lower FOM<sup>[140]</sup> ( $FOM = S/\text{FWHM}$ ), a standard criterion for evaluating sensor performance, making them impractical in many cases. In contrast, photonic modes like GMR are constrained with considerably lesser sensitivity while characterized by ultralow spectral linewidth due to their extreme confinement inside the dielectric medium. Additionally, photonic modes like RA, which are somewhat more sensitive due to the involvement of leaky modes,<sup>[141]</sup> can also increase the photonic lifetime. Thus, incorporating plasmonic–photonic coupling offer enhanced sensing properties; high sensitivity with low losses can provide an improved FOM and high Q for the hybrid plasmonic sensors.<sup>[142–144]</sup> Figure 2A-iii shows a generalized hybridization concept for a particular case of photonic-plasmonic coupling; photonic guided modes in a waveguide (backed by metallic layer) interact with LSPR modes of Au nanoparticles<sup>[132]</sup> to result in splitting into two branches. Such splitting is a characteristic of metallic photonic crystal slabs, discussed in the upcoming section. Following Figure 1, the plasmon–photon hybridization manifests in different types of resonances such as surface lattice resonance (SLR = RA + LSPR; Figure 2B-i),<sup>[47]</sup> metallic/colloidal photonic crystal slabs (m/c PhCs = LSPR + GMR; Figure 2B-ii),<sup>[97]</sup> hybrid guided mode resonances (hGMR = SPP + GMR; Figure 2B-iii),<sup>[52]</sup> and hybrid surface plasmon polariton (hSPP = RA + SPP; Figure 2B-iv)<sup>[54]</sup> modes. We discuss each of these hybridized modes while highlighting the underlying principles.

### 2.2.1. Surface Lattice Resonance

Surface lattice resonances (SLR), also known as collective lattice resonances (CLR),<sup>[145]</sup> are optical phenomena observed in metallic lattices that involve the hybridization between the photonic modes of RA diffraction in a lattice and plasmonics mode of localized charge oscillation on a single metallic nanoparticle.<sup>[146]</sup> For metallic NPs arranged in an array, a normal incidence of light perpendicular to the plane of NPs gets diffracted/scattered in all directions. Depending on the periodicity, the RA-diffracted waves moving parallel to the nanoparticle array can radia-

tively couple to the individual nanoparticles' LSPR. This coupling shrinks the plasmon resonances significantly, even down to only 1–2 nm in spectral width, thus possessing extremely high-Q factors. Experimentally, first observed in 2D arrays of AuNP<sup>[147,148]</sup> and AgNP<sup>[149]</sup> (around 2008–2009), it soon gained prominence because of exhibiting almost three orders of enhanced Q-factors<sup>[150,151]</sup> compared to the LSPR of the isolated constituent. Most SLR research has concentrated on NP arrays composed of Au and Ag due to their powerful optical reactions within the visible and near-infrared wavelengths. Nevertheless, NPs made of aluminum (Al) have more recently demonstrated the capacity to maintain high-Q SLR throughout the entire range of ultraviolet to near-infrared wavelengths.<sup>[152,153]</sup> By a combination of plasmonic and photonic resonances, one can achieve even higher field enhancements than characteristic plasmonic counterparts, along with long-lived lifetimes from the photonic array structure that can be applied to fields like plasmonic linewidth engineering,<sup>[46]</sup> lasing<sup>[154,155]</sup> and sensing.<sup>[48,140]</sup> Note that a plasmonic array does not necessarily guarantee ultrasharp modes.<sup>[156,157]</sup> Nanostructures with smaller dimensions ( $d$ ) compared to their periodicity ( $\Lambda$ ), i.e., arrays with lower fill-factor ( $F = d/\Lambda$ ), mainly result in sharper features<sup>[46,158]</sup> compared to structures with higher fill-factor.<sup>[159]</sup> Depending on the NPs' geometric properties and their coupled diffraction mode order, the ultra-narrow resonances can possess either dipolar<sup>[139,160]</sup> or quadrupolar<sup>[161,162]</sup> characteristics. Figure 2B-i shows the evolution of SLR in an AuNP array placed in a uniform symmetric index corresponding to its primary constituent resonances.<sup>[47]</sup> FDTD calculated E field and extinction spectra are shown for the plasmonic LSPR and photonic lattice modes, as well as the hybrid SLR. The area immediately surrounding the nanoparticles, i.e., the near-field region, displays a dipolar pattern that is distinctly identifiable. This pattern features significant enhancement of  $|\bar{E}^2|$ , typically ranging from two to three orders of magnitude greater than that of the original incident light, and is concentrated on opposing sides of the NPs in the direction of polarization. The reason behind such enhancements can be explained using coupled dipole approximation (CDA)<sup>[163]</sup> where the array of metallic NPs can be considered as an array of dipoles<sup>[164]</sup> where the  $n^{\text{th}}$  dipole is represented by  $\bar{P}_n = \alpha_n \bar{E}_n$  with  $\alpha_n$  as its polarizability and  $\bar{E}_n$  as the corresponding field. Considering an infinite array and same  $\alpha$  for all particles, the effective polarizability and extinction cross-sections from a particle in the array is<sup>[165]</sup>

$$\alpha_{\text{eff}} = [\alpha_s^{-1} - S]^{-1}; C_{\text{ext}} = 4\pi k \text{Im}(\alpha_{\text{eff}}) \quad (10)$$

Here  $\alpha_s$  is the polarizability of a single isolated particle, and  $S$  is the sum of retarded dipoles from all other particles. By controlling the size and morphology of AuNPs as well as periodicity, one can make  $S = \alpha_s^{-1}$ , leading to  $C_{\text{ext}}$  as infinity.<sup>[144,166]</sup> As seen from simulations and experiments, having a uniform environment for exciting SLRs at normal incidence is essential. For an asymmetric environment, diffractions can be suppressed while considering only a substrate<sup>[167]</sup>; however, embedding the arrays into a uniform background (e.g., using a cover index of 1.33 for sensing) allows for the occurrence of diffractive coupling between light and lattice surface modes, resulting in a sharp spectral line. Besides the conventional lattice, SLR has also been demonstrated in arrays of different lattice symmetries,<sup>[168,169]</sup> like rectangular,

hexagonal, honeycomb, and Lieb arrays. Strong coupling of SLR with an additional layer of organic molecules and electronic materials like Rhodamine 6G (R6G)<sup>[170]</sup> and molybdenum disulfide (MoS<sub>2</sub>)<sup>[171]</sup> respectively, have also been reported. Notably, hybridization between two SLR types in complex metallic lattices is also investigated theoretically<sup>[172]</sup> and experimentally.<sup>[173]</sup> Details about different aspects of SLR, including materials, configuring geometries, and its prospects in various application fields, can be found in recent extensive reviews.<sup>[142,145,166]</sup> The current review focuses on its advanced sensing features discussed in Section 4.1.

### 2.2.2. Metallic/Colloidal Photonic Crystal Slabs (m/C PhCs)

In the early 2000s, it was first observed that by arranging metallic nanoparticles in specific patterns over a waveguide whose guided modes lie within the same wavelength range as the particle-plasmon resonance, the extinction spectra of the metallic nanoparticles can be tuned with possibilities of almost complete suppression of light extinction in small spectral bands through destructive interference.<sup>[174]</sup> For its simpler version of on dielectric waveguide substrates, Christ et al. coined the term ‘metallic photonic crystal slabs’ because of their close analogy to periodic photonic crystal structures. Unlike the 2D case of metallic nanodots, 1D metallic nanowires exhibited only a single plasmon resonance (occurring for light polarized perpendicular to the wires, i.e., TM polarization). By coupling the photonic (waveguide mode) and electronic (localized particle plasmon) resonances, a large Rabi splitting of 240 meV was found in transmission measurements for the coupled resonance condition following the formation of a new polariton state, characterized by anti-crossing behavior.<sup>[175]</sup> For coupling of plasmon to photonic guided modes of the waveguide, plasmon dephasing time for the generated waveguide-particle-plasmon-polaritons (measured with sub-15 fs laser pulses using nonlinear interferometric autocorrelation methods) is prolonged with increasing coupling strength.<sup>[176]</sup> While the TE excitation shows sharp features in the extinction due to the Bragg resonance of TE<sub>0</sub> waveguide modes (Fano lineshape due to the interaction of the discrete waveguide mode with the photon continuum), the TM excitation produces a narrow peak due to TM<sub>0</sub> quasi-guided modes, along with the broad resonance due to particle plasmon in the individual metallic wire. For a change of periodicity or AOI, the broad plasmonic mode exhibits the anti-crossing behavior as a hybridization signature with narrower TM-waveguide resonances.<sup>[177]</sup> Using a scattering matrix-based theoretical description, the effect of the waveguide thickness for such mPhCs is explained in conjunction with the experimentally obtained transmittance (and hence extinction; Ext = - ln T).<sup>[178]</sup> However, coupling phenomena for two harmonic oscillators of different line widths can also be used to well-explain the hybridization process. Let us consider that the displacement, resonant frequency, HWHM (half-width at half maxima), and charges (oscillator strengths) for the uncoupled particle-plasmon oscillator (p) and waveguide oscillator (w) are:  $x_p$ ,  $\Omega_p$ ,  $\gamma_p$ ,  $q_p$  and  $x_w$ ,  $\Omega_w$ ,  $\gamma_w$ ,  $q_w$  respectively. The coupled oscillation equation can be written as:

$$\frac{d^2x_p}{dt^2} + 2\gamma_p \frac{dx_p}{dt} + \Omega_p^2 x_p - \Omega_c^2 x_w = \frac{q_p E(t)}{m} \quad (11)$$

$$\frac{d^2x_w}{dt^2} + 2\gamma_w \frac{dx_w}{dt} + \Omega_w^2 x_w - \Omega_c^2 x_p = \frac{q_w E(t)}{m} \quad (12)$$

with  $m$  as the mass of the oscillating particles, and  $\Omega_c^2$  represents the coupling strength between them. For the case  $\gamma_w \ll \gamma_p$  or  $\gamma_w = 0$ , the absorption coefficient can be derived into

$$\alpha(\omega) = \frac{Nq_p}{V \cdot 2m\epsilon_0c_0} \times \frac{4\gamma_p\omega^2 [\omega^2 - \Omega_w^2 - (q_w/q_p)\Omega_c^2]^2}{[\left(\omega^2 - \Omega_p^2\right)\left(\omega^2 - \Omega_w^2\right) - \Omega_c^2]^2 + 4\gamma_p^2\omega^2(\omega^2 - \Omega_w^2)^2} \quad (13)$$

here  $N$  is the number of plasmon/waveguide oscillator pairs in  $V$  volume. With  $q_w \ll q_p$ , the spectral positions of the absorption maxima are:<sup>[179]</sup>

$$\omega^2 = \frac{\Omega_p^2 + \Omega_w^2}{2} \pm \sqrt{\frac{\left(\Omega_p^2 - \Omega_w^2\right)^2}{4} + \Omega_c^4} \quad (14)$$

The resultant line shape is Fano type denoting the coherent interaction of a single spectrally sharp oscillator with another homogeneously broadened oscillator. For thinner slabs with non-favorable guided modes, RA prevails. In contrast, plasmon modes with sharper line features can be excited at a particular choice of periodicity or by a selection of AOI, whereas for thicker waveguides, the quasi-guided mode existent for all of the periodicities.<sup>[178,180]</sup> This is a crucial advantage of mPhCs over SLR, as strict parameter dependence is unnecessary while trying to narrow down the line shapes for better-resolved sensing applications. Compared to electron-beam lithographic fabrication of Au nanowires<sup>[177]</sup>/nanodisks<sup>[174]</sup> on to deposited ITO waveguide layer, mPhCs formed using interference lithography and dry etching<sup>[181]</sup> or using spin-coating of AuNPs into interference lithographic masks, followed by annealing,<sup>[182]</sup> results in faster and convenient scaling up nanopatterned regions for implementation of the waveguide-plasmon polariton modes in light-emission,<sup>[183]</sup> photochemistry,<sup>[184]</sup> and photoinduced charge transfers.<sup>[185]</sup>

Figure 2B-ii describes such hybridization of plasmonic and photonic resonances where a metallic nanodisc array is arranged over a semiconductor waveguide. The hybridization picture can be idealized from the simulated transmittance results, showing two distinct dips. While the broader mode still represents dipolar single-particle resonance, the sharp mode at a lower wavelength contains a higher lifetime to counter the plasmonic losses. Broad plasmonic resonance (black curve) interacts with the guided modes of a slab waveguide (red curve) to form hybrid modes (blue curve) with Fano-type asymmetric line shapes. The corresponding electric field distributions are given, showing that the pure plasmonic modes are shown in terms of intensified electric fields at the edges of the nanodisc only. The pure photonic/waveguide mode for the 2D lattice results in two guided waves propagating orthogonally to each other; the electric field corresponds to the TM polarization in the figure. For the hybridization, both the plasmonic and photonic modes are simultaneously excited.

A particular case of mPhCs, contains an additional metallic layer below the waveguide, forming metal–insulator–metal nanocavity arrays.<sup>[132]</sup> The sensing features of mPhCs are discussed in Section 4.2.

Compared to metallic photonic crystal slabs, we, as König group, have recently realized colloidal photonic crystal slabs containing colloidally grown plasmonic AuNPs, assembled on top of a photonic waveguide. Similar to 1D metallic nanowire geometry, the plasmonic modes associated with the particle chains can now be coupled to the photonic modes of the grating-waveguide structure. Previously, a simple grating structure with arranged silver nanocube (AgNC) particles on top has demonstrated broadband absorption in the visible spectrum by using the LSPR of the AgNCs.<sup>[186]</sup> For such single nanoparticle structures, adding a waveguide below the grating can generate 1D photonic crystals (PhC) with waveguide modes available for coupling with the nanoparticle LSPR. The Cunningham group has established a plasmon-photon synergy by coupling such discrete metal nanoparticles to surface resonant modes of the PhC for various applications related to Raman spectroscopy.<sup>[187]</sup> The PhC-coupled system has a tunable, cooperative interaction that leads to a significant increase in the local field intensity of the plasmonic nanoparticle, with applications in the enhancement of the SERS signal<sup>[188]</sup> and photocatalysis.<sup>[49]</sup> For our cPhCs, the single LSPR unit can be replaced by a 1D lattice of plasmonic nanoparticle chains, which has higher significance than a single nanoparticle. Following the discussion with particle dimers, adding more particles to the structure forms a linear particle chain, leading to a red shift of the predominant dipolar mode.<sup>[189,190]</sup> The spectral position of this mode converges to a specific wavelength depending on several factors like interparticle spacing, particle size, particle morphology, and surrounding media.<sup>[189,191]</sup> The infinite chain limit for spherical particles can be considered for the range of 8–12 particles,<sup>[192]</sup> where the addition or subtraction of a particle from the chain does not impact the resonant line shapes. Below the infinite chain limit, linear clusters are referred to as plasmonic oligomers.<sup>[193]</sup> Plasmonic particle chains could be used to integrate colloids in various applications, such as waveguiding, energy transfer, and sensing, due to the collective, coherent coupling within such particle chains and the substantial electric field enhancement in the hotspots between the particles.<sup>[189,193,194]</sup> The plasmonic chain modes (super and sub-radiant) have a larger FWHM and experience a higher radiative loss, causing a lower Q-factor with poor resolution. However, by combining plasmonic features with the high-Q photonic modes of a dielectric GMR structure (which has smaller FWHM), the sensitivity of the hybridized cPhC modes can be improved while maintaining their sharpness and quality when compared to the dielectric counterpart (GMR). Following the self-assembly concepts of realizing these plasmonic chain-based resonant grating structures, stacking two of such grating, with nonorthogonal in-between stacking angle, can result in hierarchical 3D structures exhibiting tunable circular dichroism.<sup>[195,196]</sup>

### 2.2.3. Hybrid-Guided Mode Resonance

Similar to metallic photonic crystal slabs, another class of metallic-dielectric structure with periodic patterning involves ex-

citation of hybrid-guided modes, which can be considered coherent excitation of surface plasmon polaritons (SPP) as well as guided waves in grating-waveguide based resonant structures. Depending on the various configurations covered in the literature concerning the metal–dielectric interfaces, the hybrid resonant elements can be classified under the following categories: i) dielectric grating on metal surface,<sup>[52,197,198]</sup> ii) dielectric grating + waveguide on metal surface,<sup>[199,200]</sup> iii) metallic grating (broader width) + dielectric waveguide,<sup>[201]</sup> iv) metal coated dielectric grating + waveguide,<sup>[202]</sup> v) metal coated dielectric grating,<sup>[203]</sup> vi) metal coated dielectric grating + metal coated dielectric waveguide.<sup>[204]</sup> Because of the metallic coating, the structures are optically characterized primarily under the reflection scheme for wavelength/angular-based interrogations. Irrespective of the configurations, the metal–dielectric interface generates SPP waves under TM polarized excitation, matched by the grating vector. In contrast, the waveguiding layer supports the confinement of the modes. A high-indexed grating layer with sufficient thickness acts as the waveguiding medium for structures without any separate waveguide.<sup>[205]</sup> For the first case of dielectric grating on a metallic surface, both theoretical<sup>[206]</sup> and experimental<sup>[52]</sup> investigations have been separately carried out on the structural dependence of the resonant modes. Figure 2B-iii shows such a case where the SPP and the TM<sub>1</sub> modes are spectrally separated, with electric field plots showing the distribution of the modes at a particular wavelength of the resonance, corresponding to the reflectance spectra. Similar to such a study, sensing experiments with hybrid GMR structures are carried out by Canalejas-Tejero et al.<sup>[197]</sup> The hybrid guided modes in the waveguide are more sensitive to index variations for the cover region than the pure SPP mode near the metallic surface. This can again be confirmed from Figure 2B-iii, showing that the hybrid GMR mode extends primarily into the cover region, accounting for higher sensitivity. For an increased grating thickness, even higher-order guided modes can be generated.<sup>[204]</sup> For the second case, metal-assisted guide mode resonant (MaGMR) structures offer enhanced sensitivity; 1D/ 2D structures with asymmetries and compound grating nature have been investigated for sensing<sup>[207]</sup> and bandpass filtering.<sup>[208]</sup> The third case has a similar structural configuration to mPhCs; however, the structure involves coupling between SPP existing in the broad metallic Au bars arranged onto a silicon nitride waveguide and a silicon substrate. The fourth case represents a structure for hybrid plasmon-photon coupling along with the formation of Bound states in the Continuum in a plasmonic grating coupled to a dielectric optical waveguide. The fifth and sixth cases are also similar but include the different positions of the metallic layer, corresponding to the waveguide that has been studied in the upcoming sensing section. Since SPP can also be excited in a graphene layer, they are also associated with dielectric grating-waveguide geometry for forming graphene-based hybrid elements.<sup>[53,209]</sup>

### 2.2.4. Hybrid-Surface Plasmon Polaritons

As a last part of the hybridization picture comes the association of Rayleigh anomaly (RA) with the surface plasmon polariton (SPP) modes. This is predominantly found in two types of structures; a 2D array of metallic nanoholes and low-indexed pillars

supported on metallic film. According to Figure 2B-iv, a metallic 2D nanohole array with asymmetric indices in the cover ( $n_C$ , region III) and substrate ( $n_S$ , region I) region can give rise to two different  $RA_C$  and  $RA_S$ . The corrugated metal surfaces also support SPP Bloch waves (standing waves formed by the superposition of two counter-propagating SPP waves).<sup>[210]</sup> Thus, two different SPP-BWs can be generated on the metal-cover (SPP-BW<sub>C</sub>) and metal–substrate interface (SPP-BW<sub>S</sub>). Keeping other parameters constant, variation of the cover index leads to a variation of  $RA_C$  and the SPP-BW<sub>C</sub>, while the other two remain unaffected. For a particular value of  $n_C$ ,  $RA_C$  becomes co-existent with SPP-BW<sub>S</sub> leading to interference and formation of RA-SPP mode; this, in turn, leads to a sudden rise in the transmission with a sharp spectral feature,<sup>[54,211]</sup> as shown in Figure 2B-iv. The associated FDTD calculated electric field profile verifies the coupling between the (1, 0)  $RA_C$  (high intensity near the film surface) and (1, 0) SPP-BW<sub>S</sub>. Like a 2D hole array, flat metallic surfaces can also generate hybrid-SPP resonances using dielectric grating by coupling RA and SPP modes. For example, low-index contrast dielectric lattices on metal<sup>[55]</sup> can give rise to hybrid SPP mode (located within the dielectric pillars) as opposed to the normal SPP mode generated at the metal–dielectric interface. Details of both these types are discussed in Section 4.4, with respect to the sensing applications.

### 3. Fabrication Overview for Plasmonic Hybridization Sensors

The hybrid geometries discussed in this review consist of periodic building blocks of photonic and plasmonic constituents where defect-free structural arrangements over large areas are crucial in obtaining sharp spectral features. This issue is essential for sensing applications where the sole purpose of introducing hybridization is maintaining the high FOM; structural defects can introduce unwanted losses, resulting in the broadening of line shapes. On the other hand, it is also necessary to have nanopatterning over a large area to control the signal-to-noise ratio. Thus, a feasible, cost-efficient fabrication methodology involving lesser process steps is well-sought. Almost all hybrid nanostructures containing dielectric/plasmonic repeating blocks (either holes or pillars) with associated metallic/dielectric layers can be fabricated using two main process steps: manufacturing the periodic templates that can act as photonic lattices and use these templates to arrange plasmonic blocks in an array.

#### 3.1. Lithographic Approaches for Template Fabrication

While most semiconductor or microprocessor industries use conventional photolithography to design optoelectronic integrated circuits, the spatial resolution of those structures is limited by optical diffraction and hence finds less applicability in the realization of nanophotonic geometries. Thanks to the development of advanced fabrication techniques that allows us to efficiently produce templates of high resolution with tailored shapes and sizes.<sup>[156]</sup> Although there are several lithographic techniques, we discuss the most important ones depending on their repeated usage in the literature, such as electron beam lithography

(EBL),<sup>[212]</sup> nanosphere lithography (NSL),<sup>[213]</sup> laser interference lithography (LIL),<sup>[214]</sup> and nanoimprint lithography (NIL).<sup>[215]</sup> Other notable mentions include focused ion beam lithography (FIBL),<sup>[216]</sup> dip-pen lithography (DPL),<sup>[217]</sup> direct laser writing (DLW),<sup>[218]</sup> laser ablation (LA),<sup>[219]</sup> etc. Indeed, an ideal methodology requires reproducibility, homogeneity, higher throughput, and cost-efficiency; however, these established techniques have their own merits and demerits where a trade-off between such qualities occurs depending on the production of these structures in research or industrial levels.<sup>[220]</sup>

##### 3.1.1. Electron Beam Lithography (EBL)

As one of the most powerful lithographic techniques, EBL uses a scanning beam of tightly focused electrons over a radiation-sensitive polymer resist layer to design custom nanoscale patterns.<sup>[10]</sup> Originating in 1967, EBL has advanced to deliver the highest spatial resolution of sub-10 nm.<sup>[221,222]</sup> Following a raster scan, with intermediate stopping via a blanker, the exposed regions of the resist either get washed off (positive) or stay (negative) during the development process.<sup>[156]</sup> Traditional resists include poly(methyl methacrylate), commonly known as PMMA,<sup>[223]</sup> along with other specialized ones like hydrogen silsesquioxane (HSQ)<sup>[224]</sup> or NaCl crystals.<sup>[225]</sup> As shown in Figure 3A-i, the electrons interact with the polymer and release their energy on scanning, which is used to break the polymeric chains. For PMMA, a developer solution consisting of methyl isobutane ketone (MIBK) in isopropyl alcohol (IPA) can have a faster dissolution rate of the exposed regions with smaller chains.<sup>[226]</sup> This results in holes within the PMMA layer, as shown via an SEM image in Figure 3B-i.<sup>[227]</sup> After succeeding through metal deposition and lift-off processing steps, the positive resist template with a 2D nanohole array can result in plasmonic or hybrid devices. In contrast, Figure 3B-ii shows PMMA/P(MMA 8.5 MAA) bilayer as a negative tone resist resulting in 2D pillars.<sup>[228]</sup> With a 50 nm feature size, these pillars are crucial for generating a metallic nano-hole array through similar processing steps, as further discussed in Section 3.2. Despite the remarkable features like the highest resolution (owing to the electron beam diameter in the Angstrom scale) and possibilities of arbitrary complex patterning (using user-defined CAD layouts), the disadvantage lies in the serial fabrication technique. Because of point-to-point interaction, nanopatterning over a large area (centimeter scale) requires excessive operation time as well as a high cost of production, making EBL less favorable for large-scale industrial production and limited to proof-of-concept purposes mainly. Thus, lithographic techniques producing large patterned areas in parallel have recently gained more interest.

##### 3.1.2. Nanosphere Lithography (NSL)

A comparatively faster route for designing periodic hexagonal templates involves inexpensive NSL with higher throughput.<sup>[10]</sup> Initially termed as “natural lithography,”<sup>[229]</sup> spherical colloids are transferred to substrates through spin-coating,<sup>[213]</sup> dip-coating,<sup>[230]</sup> drop casting,<sup>[231]</sup> or Langmuir-Blodgett arrangement,<sup>[232]</sup> followed by drying-induced capillary forces to

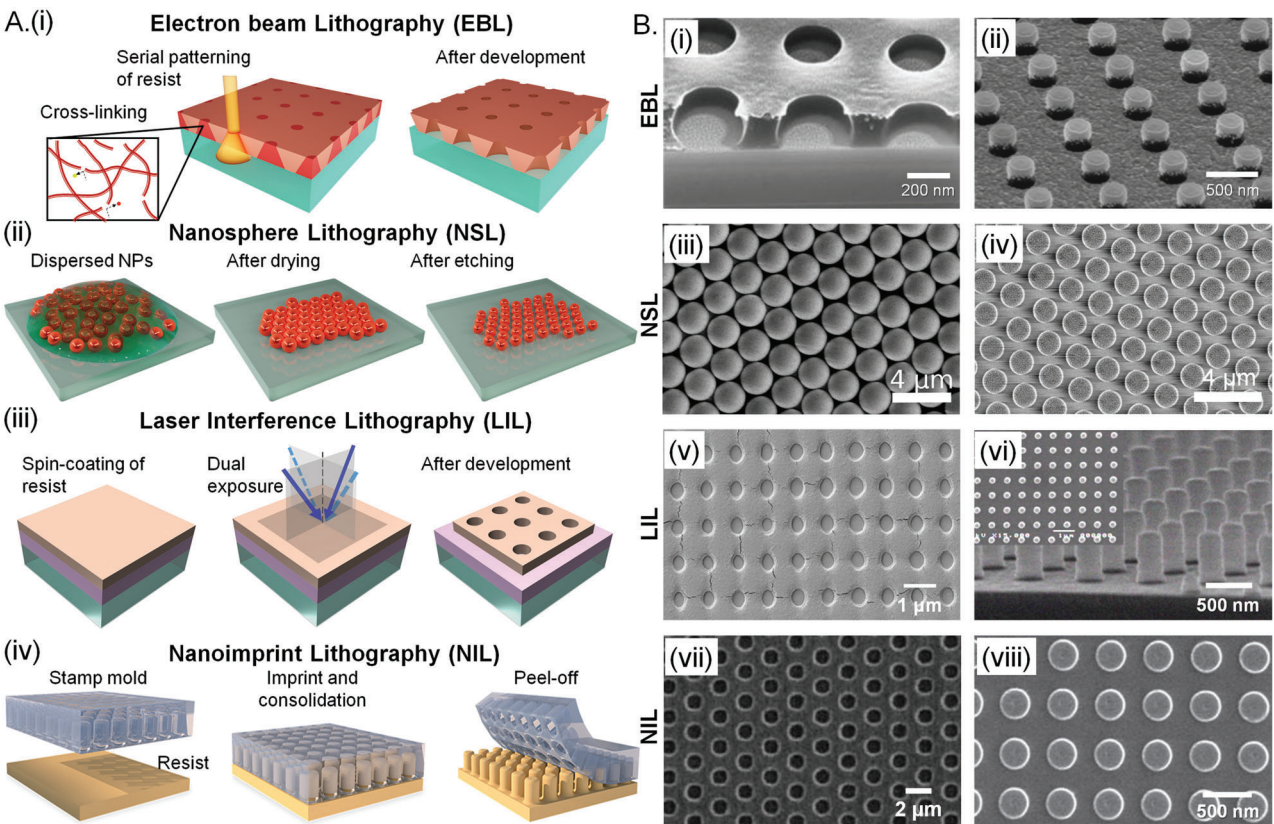


**Figure 3.** Template fabrication through different nanopatterning techniques. A) Schematics of the different approaches are shown. A,i) Electron beam lithography (EBL) showing serial patterning of the resist layer. The resulting undercut structures after development are suitable for material processing. A,ii) Nanosphere lithography (NSL) shows the initial dispersion of NPs in solution, the close-pack assembly formation after solvent drying, and further control of interparticle spacing using etching. A,iii) Laser interference lithography (LIL) via interference of two beams. For generating a 2D pattern, the sample stage is rotated by 90°. Reproduced under the terms of the Creative Commons CC-BY license.<sup>[97]</sup> Copyright 2022, the authors, published by Wiley VCH. A,iv) Nanoimprint lithography (NIL) with a prefabricated stamp mold used to imprint and consolidate resist, followed by peeling-off of the stamp. Reproduced with permission.<sup>[250]</sup> Copyright 2021, American Chemical Society. B) Scanning electron microscopy (SEM) images of the fabricated templates. B,i) EBL induced 2D hole array in the resist layer. Reproduced with permission.<sup>[227]</sup> B,ii) 2D-pillars formed using EBL and negative resist. Reproduced with permission.<sup>[228]</sup> Copyright 2015, AIP Publishing. B-iii,iv) Dielectric spheres assembled before and the after the etching step in NSL. Reproduced under the terms of the Creative Commons CC-BY license.<sup>[233]</sup> Copyright 2017, the authors, published by Optica. B-v) 2D hole array within the resist layer, formed by dual exposure via LIL. Reproduced under the terms of the Creative Commons CC-BY license.<sup>[97]</sup> Copyright 2022, the authors, published by Wiley VCH. B-vi) Vertically standing resist pillars formed by LIL. Inset shows the top view of the 2D-array. Reproduced under the terms of the Creative Commons CC-BY license.<sup>[251]</sup> Copyright 2019, the authors, published by MDPI. B,vii) Nanohole array in a hexagonal lattice produced by NIL. Reproduced with permission.<sup>[252]</sup> Copyright 2009, AIP Publishing. B-viii) 2D array of pillars recorded in Amonil resist using NIL. Inset shows a cross-sectional image of a single pillar. Reproduced under the terms of the Creative Commons CC-BY license.<sup>[253]</sup> Copyright 2011, the authors, published by IntechOpen.

arrange into a hexagonal closed packed (HCP) arrangement. The monolayer can act as a mask, where the periodicity is defined by the distance between the centers of two neighboring spheres. The periodicity is tunable through the choice of the initial size of these nanospheres, whereas further etching steps after drying can control the filling factor for the subsequent deposition process. Figure 3A-ii gives a pictorial image of the fabrication scheme whereas Figure 3B-iii,iv exhibit SEM images of the assembled monolayer of silica spheres, before and after the etching step.<sup>[233]</sup> Although the closed-pack structure of spheres can have defect-free domain up to the size of 100  $\mu\text{m}^2$ ,<sup>[234]</sup> it is challenging to eliminate the defects in centimeter scales.<sup>[235]</sup> Another drawback includes a lack of control over the geometry, as final structures with hexagonal periodicities can only be achieved.

### 3.1.3. Laser Interference Lithography (LIL)

Laser Interference lithography (LIL)<sup>[236]</sup> has gained a lot of attention for producing periodic structures and large-scale gratings with high throughput.<sup>[237]</sup> As the name suggests, it uses optical interference of laser beams originating from a common source in a simple, extremely rapid, defect-free, and cost-effective way toward the fabrication of 1D, 2D, and 2D micro/nanostructures.<sup>[214,238]</sup> Also known as holographic lithography, this method is very flexible in controlling the fabrication parameters, thus resulting in the tunability of the lattice constants. Interference of multiple collimated beams, with desired wavelength and beam propagation direction, can decide the resultant photonic lattice.<sup>[239]</sup> Due to interference of two or more beams, a time-independent spatial variation of intensity is

transferred into a light-sensitive medium, such as a photoresist, that can uniformly record the intensity distribution or its inverse, depending upon its nature. Being an interference process, LIL offers large scaled nanopatterning, with beam width in tens of centimeters, while the spatial resolution still being as low as 300 nm. Unlike photolithography, LIL does not use any physical mask and hence is free of the diffraction limit. The angle of interference can manipulate the interference pattern, the number of beams,<sup>[240,241]</sup> as well as by the polarization,<sup>[242]</sup> intensity,<sup>[241]</sup> and phases<sup>[243,244]</sup> of the interfering beams. For a simple case of two-beam interference, the periodicity is defined by  $\Lambda = \lambda/(2\sin\theta)$  with  $\Lambda_{\min} = \lambda/2$ . Thus, spatial resolution is limited to half of the laser wavelength (mostly in UV because the available photoresists have their maximum absorption in this range). However, LIL requires precise alignment control and optimization of exposure dosage and development time to achieve the desired grating profile and depth. Figure 3-iii shows the process steps for obtaining a 2D hole array<sup>[97]</sup>: spin-coating of a negative resist (ma-N 405) followed by dual-exposure of a two-beam interference ( $\lambda = 325$  nm) with in-between 90° rotation of the sample stage. A 2D hole array etched up to the substrate can be produced for an optimized development time. Figure 3B-v shows an SEM image of such a resist-based 2D hole array that is succeeded with processing steps for realizing plasmonic nanodisks. Conversely, 2D resist pillars can be produced by LIL while using a positive-tone photoresist. Figure 3B-vi shows an SEM image of 2D pillars of positive resist (SC-1827, Rohm, and Haas), produced by an interferometric setup using 300 mW Melles Griot solid-state laser operating at  $\lambda = 458$  nm.

### 3.1.4. Nanoimprint Lithography (LIL)

NIL offers a solution to the low-cost, high-resolution, and high-throughput fabrication methods for creating nanostructures. Developed by Chou in 1995,<sup>[245]</sup> NIL has advanced over time to meet real-world industrial demands like sub-10 nm imprinting.<sup>[246]</sup> The process of NIL is exceptionally straightforward and involves a prefabricated master as a stamp mold that is mechanically pressed against a resist-coated substrate for pattern transfer.<sup>[247,248]</sup> Once pressed, UV exposure/ thermal heating<sup>[249]</sup> can cure and solidify the resist, after which the stamp mold can be peeled off. Figure 3A-iv schematically describes the process flow.<sup>[250]</sup> A flexible stamp mold is preferable for a more straightforward peeling-off process, often in the form of polydimethylsiloxane (PDMS) stamps. A silicon master with desired parameters can be precisely produced using the EBL technique, followed by reactive ion etching. Soft-lithography can obtain an inverse structure on a PDMS mold.<sup>[254]</sup> When further used as a stamp for the NIL technique, this PDMS mold can be repeatedly used to produce many resist templates with identical features of the master. However, the resolution of the NIL is limited by the prefabricated master that controls the structural morphology and resolution of the NIL output. Thus, nanoholes<sup>[252]</sup> and nanopillars<sup>[253]</sup> can be formed using NIL, as shown by the SEM images in Figure 3B-vii,viii, respectively. Further, sheet-to-sheet and roll-to-roll NIL or injection molding<sup>[255]</sup> processes have been used commercially for high-throughput 1D/2D grating pattern replication.<sup>[256]</sup>

Thus, an overall comparison between these different lithographic/patterning techniques is essential for template fabrication. While the EBL offers a wide range of customized patterning of complex arbitrary shapes with possibilities of sub-10 nm feature sizes, it has a very low throughput, and a very high operating cost, making it non-suitable for scaled-up fabrication processes. Nanosphere lithography, in that sense, is extremely cost-effective and has a high throughput in producing sub-100 nm features. However, it has limitations in designing complex patterns and inevitable defects. Laser-interference lithography, on the other hand, is a scalable technique with the possibility of forming complex structures by manipulating the interfering light beams in amplitude, polarization, and phase. Despite having a high throughput, the technique is limited by large feature size (lowest periodicities in the range of 200 nm, resulting in feature size of  $\approx 100$  nm). For high-throughput processes, yet with sub-10 nm features, the nanoimprint lithography serves as the best alternative to manufacture templates; the only limitation lies in the requirement of a master to produce a stamp, where the morphology of the master also restricts the stamp.

## 3.2. Formation of Plasmonic Array

Once the dielectric templates (photonic lattices) are formed using the techniques above, it is crucial to introduce plasmonic components to create hybrid plasmonic lattices. Depositing a continuous yet thin metallic layer on top can generate SPP modes with phase-matching conditions from the gratings for different injection orientations. On the other hand, isolated metallic units can support LSPR, which gets coupled to the photonic diffraction from the grating, as well as underlying cavities and waveguides, as per the desired hybrid configurations. Thus, by either a direct deposition, deposition combined with lift-off, or by an assembly of nanoparticles, different routes lead to various morphologies with distinct underlying resonance mechanisms.

### 3.2.1. Metal Deposition and Lift-off

**Figure 4A** describes the general procedure for forming plasmonic nanostructures using thin metal layer deposition, followed by lift-off. Depending on the template, one can produce nanoslits,<sup>[227,260]</sup> nanobars,<sup>[261]</sup> nanodisks,<sup>[261,262]</sup> nanorods,<sup>[263]</sup> nanocubes,<sup>[130,264]</sup> nanoholes,<sup>[265,266]</sup> nanorings,<sup>[267,268]</sup> splitting resonators,<sup>[261]</sup> nanotriangles,<sup>[261]</sup> nanopyramids,<sup>[269]</sup> V-grooves<sup>[270]</sup> and all other similar kinds of structures. Further, by choosing the underlying material (metal, dielectric, or metal + dielectric spacer), different coupling schemes can be introduced to these resonating plasmonic units. One can produce nanostructured metallic arrays with the same morphology as the templates by depositing metal films without any dissolution. Sputtering techniques<sup>[271]</sup> deposit a continuous metallic throughout the template, thus connecting the regions within the peaks and valleys. However, for electron beam or thermal evaporation-based deposition, the metals do not get deposited on the side walls of the template<sup>[210,272]</sup> producing discontinuous metallic layers. By applying high oblique angled depositions (OAD), one can also produce periodic metallic structures using

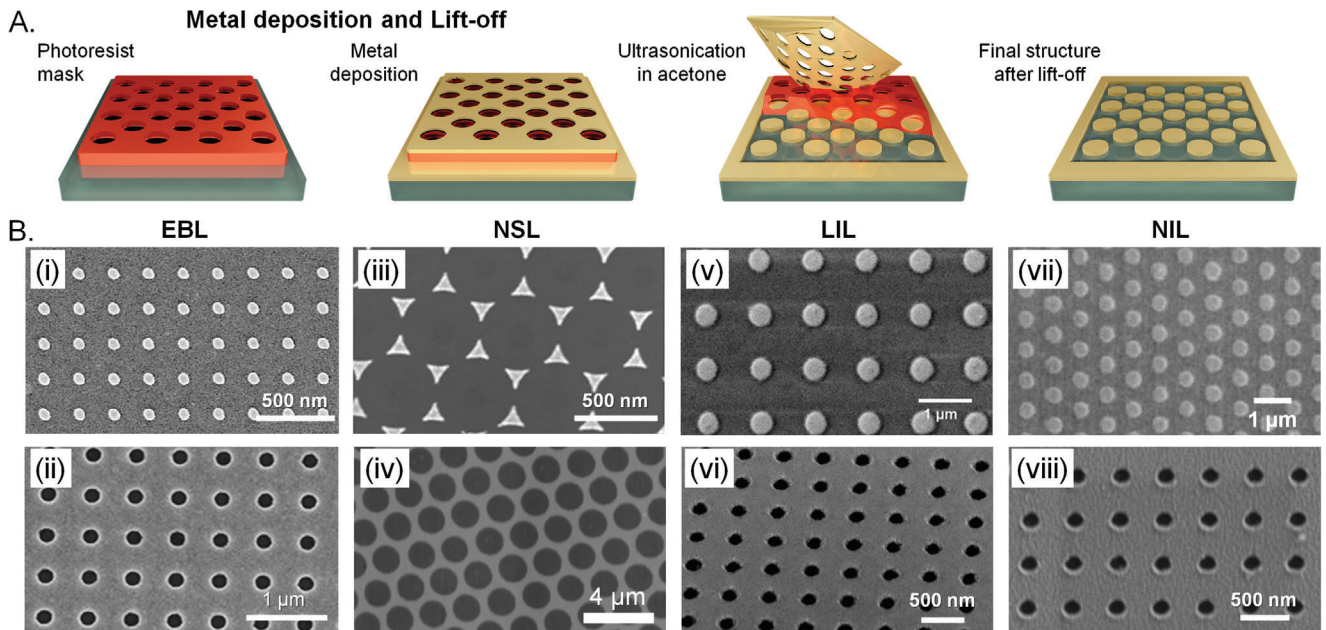


**Figure 4.** Nanopatterning with plasmonic blocks using the bulk approach. A) Schematic showing plasmonic array formed through metal deposition and lift-off techniques. B) SEM images of the produced nanostructures, obtained from the templates procured through different lithographic techniques: B-i) Gold nanodiscs on ITO-coated glass-substrate obtained using EBL masks (nanoholes). Reproduced with permission.<sup>[257]</sup> Copyright 2013, AIP Publishing. B-ii) Square-array of nanoholes in a gold film using EBL mask (nanopillars). Reproduced with permission.<sup>[228]</sup> Copyright 2015, AIP Publishing. B-iii) Gold nanotriangles formed using NSL (unetched assembly). Reproduced with permission<sup>[258]</sup> Copyright 2020, AIP Publishing. B-iv) Hexagonal nanoholes in a gold layer using NSL (etched) templates. Reproduced under the terms of Creative Commons CC-BY license.<sup>[233]</sup> Copyright 2017, the authors, published by Optica. B-v) Square-array of platinum nanodisks on titanium-dioxide thin-film using LIL mask. Reproduced under the terms of the Creative Commons CC-BY license.<sup>[97]</sup> Copyright 2022, the authors, published by Wiley VCH. B-vi) 2D nanohole array on gold film using LIL mask. Reproduced under the terms of the Creative Commons CC-BY license.<sup>[251]</sup> B-vii) Hexagonal array of titanium nanodisks formed using NIL template. Reproduced with permission.<sup>[252]</sup> Copyright 2009, AIP Publishing. B-viii) Gold nanohole array using NIL template. Reproduced under the terms of the Creative Commons CC-BY license.<sup>[259]</sup> Copyright 2013, the authors, published by MDPI.

the shadowing effect from the template structures.<sup>[273,274]</sup> The separate second metallic layer formed within the trenches/ holes complements the resist template for proceeding with lift-off processes using the normal deposition. By dissolution of the in-between resist layer, one can remove both the resist and the top sacrificial layer to produce the complementary metallic array. There are certain important things to be considered while targeting lift-off processes; i) undercut profile is necessary for a successful liftoff along with a metal: resist layer thickness of 1:3 ratio to prevent any connections between the top and bottom metal layer, ii) the template needs to be etched off till the substrate along with a presence of an adhesive layer like Chromium (Cr) or Titanium (Ti) to adhere the deposited metallic layer to the substrate strongly, iii) an ultrasonication process with controlled parameters can be included to increase the dissolution speed. Figure 4B shows the SEM images of some successful lift-off approaches where the templates were formed by the different lithographic processes discussed in Section 3.1. Using an EBL template (2D hole array formed by patterning on 180 nm thick PMMA and developing in 1:3, methyl-isobutyl-ketone and IPA mixture), 25 nm of Au was deposited, followed by lift-off technique in n-methyl-2-pyrrolidone to result in Au nanodisks, as shown in Figure 4B-i.<sup>[257]</sup> On the contrary, using a 2D array of pillars as a template (formed using bilayer patterning of P(MMA 8.5 MMA) copolymer and PMMA 950 with thicknesses 340 and

75 nm, respectively, and developing in acetone) complementary nanohole array was formed by further depositing 100 nm of Au layer, followed by stripping of the resist layers using oxygen plasma and ultrasonication.<sup>[228]</sup> For templates fabricated with the NSL technique, metal deposition along with the removal of the nanospheres through sonication produces arrays of surface-bound triangular NPs (Figure 4B-iii) that can be useful for LSPR-based biosensing<sup>[258]</sup> and SERS detection.<sup>[275]</sup> However, an additional oxygen-plasma etching step on the NSL template (HCP polystyrene nanospheres) can reduce their diameter to form hexagonal nanoholes (Figure 4B-iv) after removing spheres in tetrahydrofuran bath under ultrasonication.<sup>[233]</sup> Following a similar process flow, LIL-fabricated photoresist templates of nanohole and nanopillar arrays also result in metallic (Platinum) nanodisks<sup>[97]</sup> and Au nanoholes<sup>[266]</sup> (Figure 4B-v,vi), where the final structures also have applications in RI sensing<sup>[97]</sup> and SERS probing,<sup>[266]</sup> respectively. The same conclusion can also be drawn for the NIL-produced templates; Figure 3B-vii shows a hexagonally arranged nanohole array in M-PDMS-based resin, obtained from a quartz master after imprinting and oxygen plasma treatment whereas Figure 4B-vii shows lifted-off titanium (Ti) nanodisks after the process flow.<sup>[252]</sup> Depending on the choice of the initial master (nanohole array), the imprinted resist can also have nanopillars, resulting again in metallic nanoholes after the process flow.<sup>[259]</sup> However, NIL has severe advantages,

as discussed previously, one of which is its applicability in forming nanopatterning of different inorganic materials with a high dielectric constant, such as metal oxides, as well as a variety of chemical compositions offered by sol-gel chemistry.<sup>[250]</sup> Thus, apart from producing metallic nanostructures for hybrid geometries, NIL is indeed a flexible, high-throughput, and extremely accurate microfabrication process with possibilities of scaling up.

### 3.2.2. Template-Assisted Self-Assembly of Colloidal NPs

As a faraway approach from the methods discussed in the previous section, template-assisted self-assembly (TASA) also offers a practical route for forming large-scale plasmonic arrays using colloidally grown metallic nanoparticles. Colloidal NPs can be created through various polymerization methods,<sup>[276]</sup> such as suspension, emulsion, dispersion, and precipitation, depending on the material properties like gold, silica, or polystyrene. The pH value, catalyst concentration, reagent composition, solvent type, and reaction temperature are the factors that can influence the size and polydispersity of the particles.<sup>[277]</sup> In contrast to lithographically fabricated nanostructures, colloidal NPs play an essential role in plasmonics because of certain factors<sup>[19]</sup>: i) easy tuning of plasmonic properties by changing their size, shape, and composition,<sup>[278]</sup> ii) large extinction cross-section, allowing the NPs to absorb efficiently and scatter light for sensing and imaging, iii) presence of enhanced local electromagnetic field as “hot spots” for surface-enhanced spectroscopy and SERS applications, iv) ease of synthesis using a variety of cost-effective and scalable techniques, such as chemical reduction, seed-mediated growth, and electrochemical deposition, as well as v) biocompatibility offered by Au/Ag-NPs for usage in biosensing, bioimaging, and drug delivery. The power of TASA lies in its ability to organize numerous colloidal NPs simultaneously into precise formations by combining physical templating and capillary forces, which differs from the step-by-step structuring process of direct writing techniques. When left to dry on a patterned surface, aqueous solutions of colloidal NPs in a water-based mixture are confined into the trenches/holes in clusters where the template’s shape and size influence the arrangements.<sup>[279]</sup> Even without any lithographically fabricated patterned templates, self-assembly (SA), i.e., spontaneous organization of colloidal nanostructures into 2D assemblies,<sup>[280]</sup> has formed colloidal crystals and other interesting shapes.<sup>[281]</sup> A systematic study, giving a broad background of the self-assembly techniques for such nanopatterning (also termed colloidal lithography), is provided by Dommelen et al.<sup>[282]</sup> However, certain drawbacks that limit the SA are difficulty in assembling arrays of isolated or groups of nanostructures such as dimers and trimers, poor adhesion causing non-feasibility of post-processing steps for device fabrication due to lack of contact between the NPs and substrate for charge transfer, and catalytic activities due to presence of surface ligands, etc. To solve these challenges, lithographically fabricated templates provide additional controls over the SA, making TASA operable in length scales extending from nano to mesoscale. Being a method from two well-established fields, when used together, provide capabilities that makes TASA unparalleled as discussed in recent reviews.<sup>[283,284]</sup>

Although the list is long, some of the basic categories of TASA for fabricating different types of plasmonic arrays can be discussed. One of the most successful techniques for producing a well-organized plasmonic array is illustrated in Figure 5A-i. As the schematic shows, colloidal suspension between two parallel plates, with the top plate remaining stationary. The bottom plate (lithographically patterned template) is mounted on a translation stage, allowing linear movement while maintaining a parallel configuration. As a result, because of the attraction between the liquid and substrate, a meniscus shape is formed where the front edge has a wedge-like shape, spanning across the width of the substrate at the three-phase contact line. A heating element is used to control the evaporation of the solvent that is necessary for moving the NPs to the contact line to create a high concentration of NPs at the front edge of the meniscus. The motorized stage moves at a constant speed, causing the meniscus (which contains the NPs) to glide over the surface of the substrate. This enables suitable structures to be trapped in the recessed features where the capillary force acts in a downward direction. Directed assembly and structure build-up in the accumulation zone can be observed in real-time using a bright/dark field optical microscope.<sup>[25]</sup> Such assembly can be carried out on both soft and rigid substrates. 2D hole array can be created on the PDMS surface using a replica molding of LIL-formed 2D pillars, on which AuNPs are further assembled,<sup>[47]</sup> as shown via SEM image (Figure 5A-ii, left panel). Alternatively, by directly assembling on a LIL fabricated 1D resist grating, AuNP chains supporting longitudinal modes are fabricated (Figure 5A-ii, right panel).<sup>[50]</sup> Unlike the aforementioned spherical cases, the TASA of asymmetric NPs requires specialized templates with predesigned orientations of the holes/ traps. For instance, the assembly of gold nanorods (AuNR)<sup>[285]</sup> requires a funnel-shaped trap geometry and additional sidewalls on a solid surface to guide the assembly of AuNRs through capillary action accurately. Simultaneous control of position, orientation, and distance between the AuNRs at the nanoscale level with a 100% filling fraction for a large-scale assembly are made possible through precise EBL fabricated templates over large areas.<sup>[286]</sup> On the other hand, the schematic in Figure 5B-i shows that the NPs in well-defined holes/trenches of a soft template (PDMS) after a successful TASA can further be transferred to a different substrate using microcontact printing.<sup>[18]</sup> Figure 5B-ii shows the assembled nanorods in different orientations in PDMS (left) after TASA and onto a silicon substrate (right) after the microprinting process.<sup>[18]</sup> Such contact printing is also carried out by Hanske et al., where AuNPs assembled within a PDMS grating via spin-coating are transferred to a separate substrate.<sup>[189]</sup> One can use confinement self-assembly techniques to avoid the transfer process, as shown in Figure 5C-i. A PDMS replica mold from the LIL fabricated master can be used for stamping where a colloidal solution drop gets confined between the substrate and grating surface. After drying, the linearly arranged NPs tend to stick to the substrate with PDMS mold waiting to be lifted off. Figure 5C-ii shows the outcome of such confinement assembly where AuNP lines of 360 nm period are printed on titania layer.<sup>[20]</sup> Stepping from 1D and 2D assemblies into the realm of 3D, an exciting yet straightforward approach is shown in Figure 5D-i. Following a TASA on a 1D PDMS mold (Figure 5D-ii, SEM image showing a successful TASA), a second identical layer can be stacked with a rotational offset of 45° while

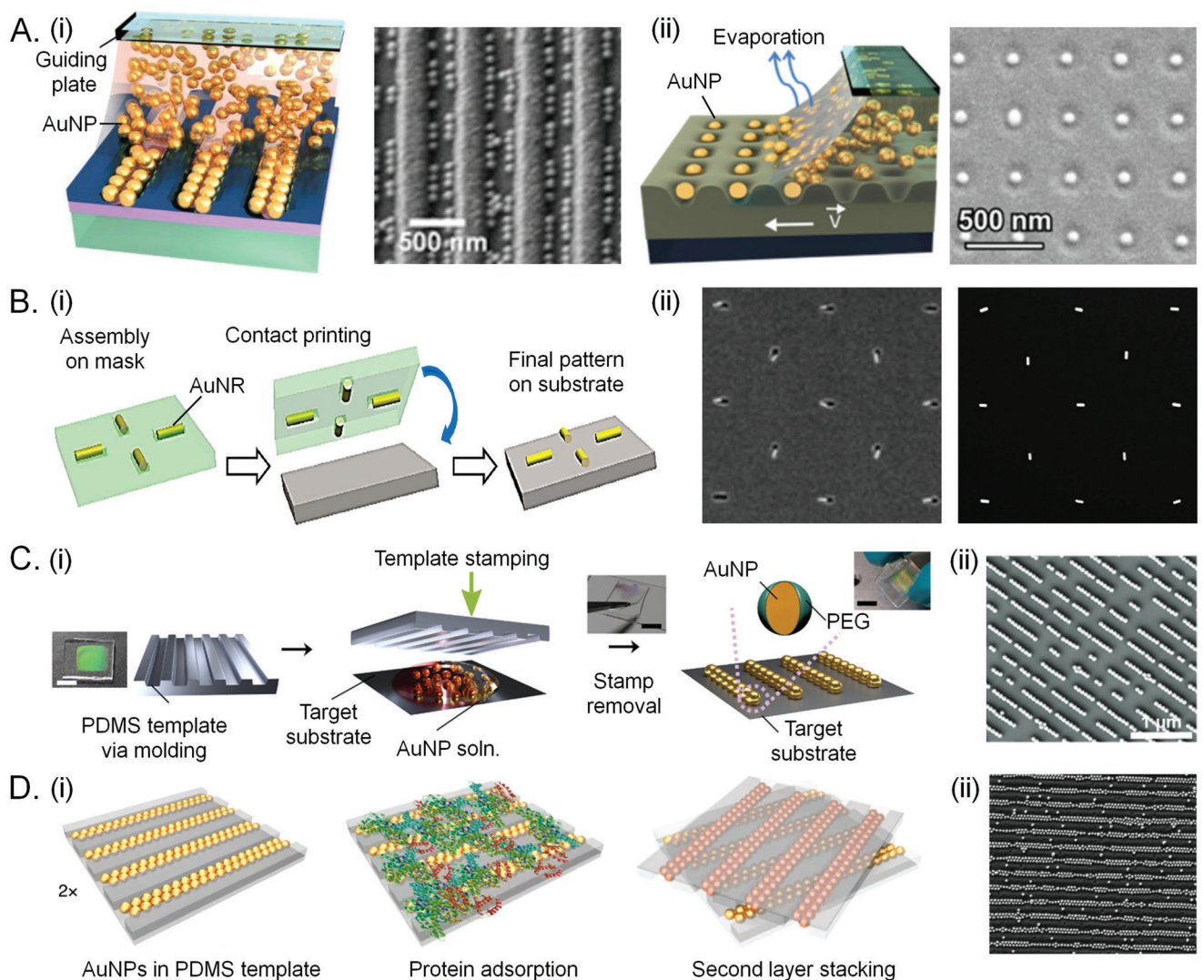


**Figure 5.** Nanopatterning with plasmonic blocks using the colloidal approach. A,i) Schematic showing TASA of AuNPs within channels of a 1D-grating along with SEM image of the assembled 1D array. Reproduced under the terms of the Creative Commons CC-BY license.<sup>[50]</sup> Copyright 2021, the authors, published by Wiley VCH. A,ii) Similar schematic of TASA using a PDMS template for arranging AuNPs into a square array. The corresponding SEM image confirms the same. Reproduced under the terms of the ACS AuthorChoice License.<sup>[47]</sup> Copyright 2019, the authors, published by ACS. B-i) Schematic showing arrangement of Au nanorods in templates followed by microcontact printing, (ii) SEM images showing trapped AUNRs assembled in a soft template (left) and on target substrate (right). B-i,ii) Reproduced with permission.<sup>[285]</sup> Copyright 2011, Wiley-VCH. C-i,ii) Direct printing of nanoparticles on target substrate using convective self-assembly with SEM image showing assembled AuNP chains on titania thin-film. Reproduced under the terms of the Creative Commons CC-BY license.<sup>[20]</sup> Copyright 2021, the authors, published by Wiley VCH. D-i) Schematic showing offset stacking of particle chains for chiral sensing of sandwiched protein layer. (ii) Corresponding SEM image shows assembled AuNPs for a single layer. D-i,ii) Reproduced with permission.<sup>[196]</sup> Copyright 2021, The Author(s), under exclusive license to Springer Nature Limited.

keeping the plasmonic AuNP chains of both layers in contact. Such structure supports strong circular dichroism (CD) that can also be used for biosensing by placing analytes (e.g., proteins) between the stacking.<sup>[196]</sup>

#### 4. Sensing Performance Overview for Hybridized Plasmonic Sensors

Among the scientific community, a trend always persists of experimenting with various plasmonic and photonic structures to assess their sensing capabilities. Different comparisons depend-

ing on the sensitivity and FOM have been argued for supremacy. Undoubtedly, plasmonic sensing is one of the most promising emerging technologies of the last decade, as metal-based plasmonic sensors offer much higher general sensitivity than dielectric-based photonic sensors. Still, the quest to find the ‘best of the best’ has resulted in new findings in which a new class of sensors benefits from the plasmonic and photonic concepts. Based on the plasmonic hybridization concepts, researchers have explored advanced hybrid RI sensors, showing exceptional sensing capabilities. These sensors can similarly be classified into five cases, per this review article’s theme. These innovative works on

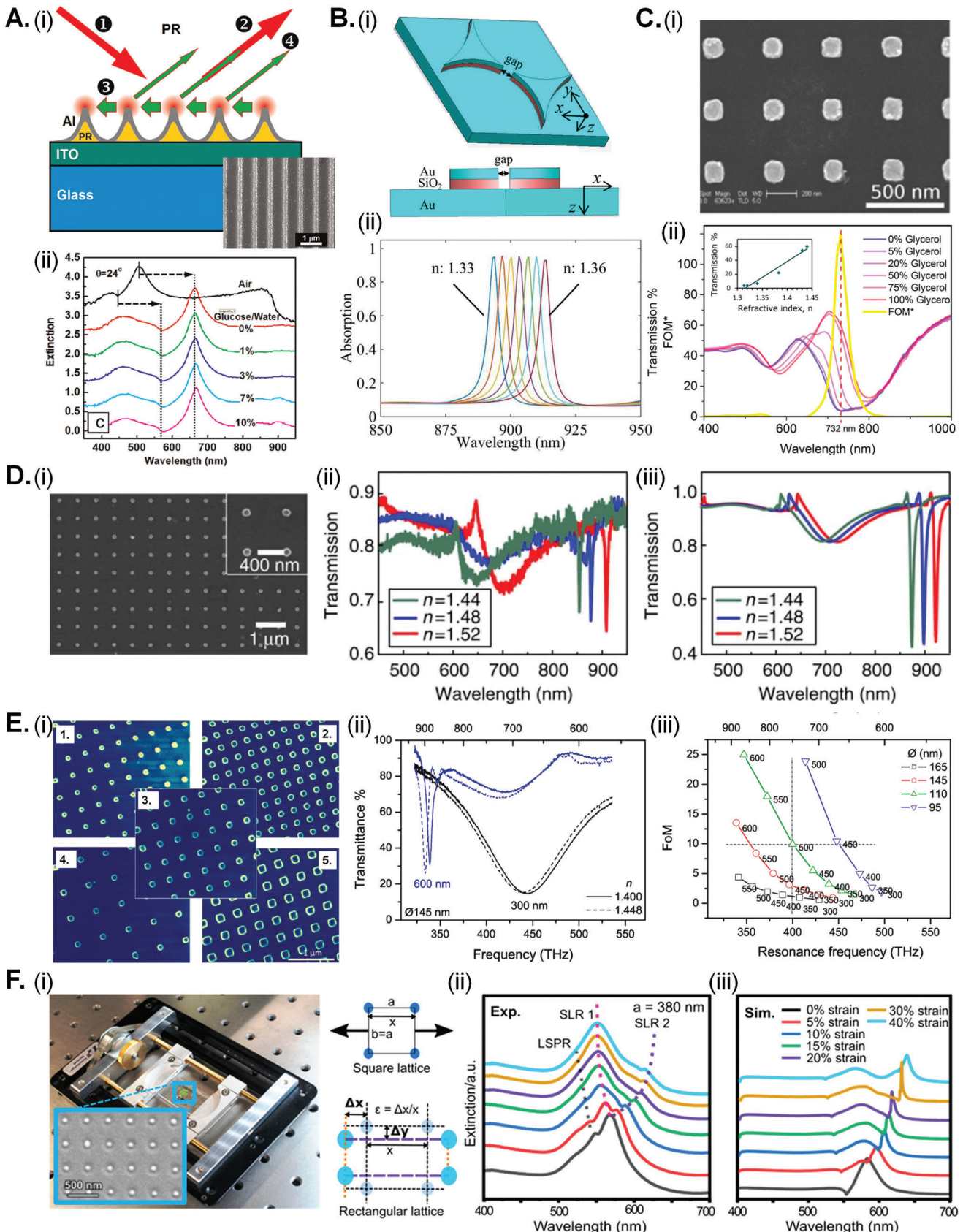
advanced hybrid RI sensors are expected to inspire more exciting hybridization ideas.

#### 4.1. SLR Sensing

SLR sensors generally show an improved FOM<sup>[287]</sup> and high bulk RI sensitivity<sup>[288]</sup> for sensing performances, verified also using analytical models.<sup>[289,290]</sup> SLR sensing has been carried out with several kinds of arrays of metallic nanoantennas, including nanowires, nanoslits, nanotriangles, nanopillars, nanodisks, etc., discussed in this section. Starting with the simplest 1D grating of metallic nanowires formed by LIL and Al deposition, SLR is described as Fano coupling between the RA and the LSPR, resulting in sharp lineshapes in the broad-band reflective optical extinction spectra.<sup>[291]</sup> Figure 6A-i shows the structural configuration with an inset showing an SEM image of the fabricated nanowires. In contrast, Figure 6A-ii shows extinction spectra (baseline corrected Fano shape with transmission from pure water as reference) for the case of AOI = 24°. For increasing the concentration of glucose/water solution (3% to 10% corresponding to a RI change from 1.3363 to 1.3454), the peak amplitude also increases, thus providing a sensitivity of 20.68 OD per RIU. Using a nano slit-antenna array milled in a thick layer of gold,<sup>[292]</sup> first-order coupled surface waves in the metallic surface (Woods anomaly<sup>[293]</sup>) produce Bragg lobes on non-normal incidence due to lifting of degeneracy. The sharp notch ( $\approx$ 5 nm) formed between the two lobes corresponding to left and right propagating surface waves can be used for sensing, showing a sensitivity of 1060 nm per RIU and a FOM of 208 for AOI = 0.2°. For plasmonic arrays through NSL/metal deposition/lift-off, the gap between two nanotriangles can support a highly localized field.<sup>[294]</sup> Simulated results shown in Figure 6B-ii show a sensitivity of 660 nm per RIU with a FOM of 132. Nanotriangles array with a sufficient thickness (60 nm), formed by EBL/metal coating/lift-off, can provide simultaneous information about local and bulk sensitivity from extinction dip and peak through excitation of quadrupolar SLR.<sup>[295]</sup> By varying bulk indices, 399 nm per RIU and 211 nm per RIU were obtained experimentally for the dip and peak positions. One of the most exciting sensing results is reported by Shen et al., where a plasmonic Au mushroom array is formed by depositing Au on EBL-formed resist nanopillars.<sup>[140]</sup> Experimentally obtained sensitivity values of 1015 nm per RIU demonstrate high sensing capabilities of the supported SLR mode, with FOM ranging from 80 to 108, almost reaching the theoretical values. Although sensitivities and FOM are calculated following general protocol, as discussed before, certain structures have complex resonances that may not fit the Lorentzian profile to estimate the FWHM properly, likewise the Q-factors and the FOM. Thus an alternative FOM defined as  $FOM^* = ((\Delta I/\Delta n)/I)_{max}$  has been used for LSPR based sensing.<sup>[296]</sup> Thackrey et al. have reported narrow collective plasmon resonances from array of gold nanocubes for simplified sensing in asymmetric air and water environments.<sup>[297]</sup> Figure 6C-i shows SEM image of the fabricated AU nanocube square array with a lattice periodicity of 450 nm. Figure 6C-ii shows the transmission variation with refractive index and FOM\* variation with wavelength for the sample with the highest measured FOM\* of 120 for the same structure in water medium.

Although different structures have drawn interest to the research, most SLR-related studies are confined to metallic nanodisks on substrates. As one of the earliest experimental observations of SLR sensing with EBL-formed Au nanodisks ( $d = 118$  nm,  $\Lambda = 316$  nm) on a glass substrate, gas sensing was carried out at an AOI of 71° to record a sensitivity of 620 nm per RIU and FOM of 180.<sup>[288]</sup> While EBL techniques may limit scalability, other methods, described in Section 3, offer large-scale nanopatterning for sensing applications. Figure 6D-i shows an SEM image of Au nanodisk 2D-array by the Odom group using their established multi-step process.<sup>[160]</sup> A copper hole array (mask) combines phase-shifting photolithography, etching, electron-beam deposition, and lift-off (PEEL), followed by wet-etching and transfer to a glass substrate. Further, deposition of Au followed by etching-based removal of the mask results in efficient liftoff/peeling with the final product of an Au nanohole array over a centimeter square area. Figure 6D-ii shows the experimentally obtained transmittances from the fabricated structure as a function of varied cover refractive index ( $n = 1.44$  to 1.58), where the SLR dip varies from 858 to 913 nm showing a bulk sensitivity  $\approx$ 393 nm per RIU. Figure 6D-iii exhibits the simulation counterpart, indicating good agreement between both. A critical study on the FOM of the SLR-based plasmonic sensors and its dependence on structural parameters is provided by Offermans et al.<sup>[287]</sup> Figure 6E-i shows SEM images of five of the samples produced in the study with various disc diameters and periodicities. Keeping a fixed diameter and increasing the periodicity or keeping a fixed periodicity while decreasing the diameter narrows the SLR peak. Figure 6E-ii shows that for a 145 nm diameter disc, 300 nm periodicity results only in a broad LSPR dip, whereas increasing the periodicity to 600 nm results in sharper SLR mode. As an overall overview, Figure 6E-iii exhibits measured FOM values as a function of spectral positions, disc diameters, and array periodicities. Another interesting case for SLR sensing is the hybridization in metallic nanoantenna (m-ANT) consisting of Au elliptical discs on silica substrates,<sup>[146]</sup> where an additional Si layer up to a critical thickness boosts high sensitivity through the hybridization phase. By varying cover indices through methanol (1.3284), acetone (1.3586), and IPA (1.3772) inclusion, a bulk SLR sensitivity of 163 nm per RIU with FOM of  $\approx$ 9 compared to bulk LSPR sensitivity of 422 nm per RIU with FOM of  $\approx$ 3.5. Because of the structural asymmetry, polarization-dependent spectral features and sensitivities can also be observed. Plasmonic nanoantennas with higher aspect ratios like nanorods,<sup>[298,299]</sup> have also been investigated in arrays for ultrahigh sensing applications.

Shifting from RI sensing, a separate category of pressure/strain sensors can be investigated using the plasmonic responses of metallic nanoparticle arrays suspended in flexible platforms.<sup>[162,193]</sup> Recently, we, as König group, have demonstrated a new cost-effective and efficient method for creating mechanotunable SLR by using soft lithography and colloidal TASA of AuNPs, over large areas.<sup>[47]</sup> Since the size distribution of the AuNPs has a significant effect on the optical properties, a comparison was drawn between lattices made up of narrowly distributed particles and those with polydisperse ones, showing better results for the former. Figure 6F-i shows the fabricated sample within a stretching device (inset shows SEM image of the lattice) that was operated over 100 cycles for the strain sensing studies. Figure 6F-ii,iii shows the array's experimental and simulated



extinction spectra, where because of the stretching, the lattice changes from a square to a rectangle and exhibits polarization-dependent extinction peaks in the optical spectra. These findings suggest that the nanostructures could be used as strain sensors and mechanically tunable filters.

#### 4.2. m/c PhC Sensing

Similar to SLR structures, metallic photonic crystal slabs (mPhCs) can tailor the optical plasmonic properties of metallic nanostructures by periodically arranging them on top of a waveguide material. Principally, it is similar to SLR in terms of coupling electronic resonance in the particle plasmons to the photonic quasi-guided mode in the waveguide material, forming polariton-type quasiparticles with narrowed-down resonant line shapes and enhancement of the FOM.<sup>[300]</sup> However, mPhCs possess certain advantages; unlike SLR, it does not need any index matching layer and hence can be implemented for a range of analyte indices and gases. Accordingly, the Giessen group has proposed and demonstrated the mPhC-based hydrogen gas sensor.<sup>[301]</sup> For mPhCs with sputter-deposited tungsten trioxide ( $\text{WO}_3$ ) waveguide and EBL fabricated Au grating (Figure 7A-i), incorporation of a gas changes the  $\text{WO}_3$  dielectric properties, resulting in variation of the photonic waveguiding conditions. Additionally, the plasmonic resonance is also affected because of changing environmental conditions. Figure 7A-ii shows measured extinction spectra for both the polarization of the mPhCs at various hydrogen pressures. For the TM pol. supporting hybridization, increasing hydrogen concentration from 0% to 20% results in an extinction increment of 0.63 (247%) with a slight blueshift of the minima between the split branches of 13 nm (1.9%). In contrast, the single extinction peak at TE pol. decreases by 0.5(36%). Thus, intensity-based sensing using a photodetector highlights the advantage of the plasmon-photon coupling under TM configuration. Au grating/ITO waveguide-based 1D mPhCs have been investigated as lab-on-chip biosensors in cryogenic environments<sup>[302]</sup> (300 to 180 K), as shown in Figure 7B-i. For a fixed period, different mPhCs with varied metallic grating widths, formed using EBL and lift-off (Figure 7B-ii) on ITO waveguides, show that wider grating widths exhibit more sensitivity to the local environment. For such sensors, the plasmon

resonance intensity is more sensitive to the lower temperature than the coupled mode (13% compared to 5%), showing relative temperature stability due to hybridization. By varying wt% of a glycerol-water mixture (corresponding change in cover RI from 1.33 to 1.47), bulk RI sensitivity of 146 nm per RIU (for  $w = 300$ ) versus 110 nm per RIU (for  $w = 250$ ) is observed (Figure 7B-iii). On a separate note, introducing a spacer layer between the metallic grating and the underlying ITO waveguide layer may appear beneficial for controlling the coupling strength between the plasmonic and photonic resonances where coupling strengths can be directly correlated to the calculated electric field at the resonances.<sup>[303]</sup> By varying the spacer layer thickness, thus, one can design highly sensitive plasmonic sensors with narrow spectral features. Other concepts include considering a spacer array between the metallic array and the waveguide layer and embedding the metallic array within the waveguide.<sup>[303]</sup> Figure 7C-i,ii describes a mesoporous silica layer with an embedded Al cylinder lattice for sensing studies with localized and extended modes.<sup>[304]</sup> The extended modes are generated due to hybridization between the LSPR resonances and the photonic quasi-guided modes. Such a system is studied under controlled pressure of isopropanol vapor (IPA) where reflectance spectra (Figure 7C-iii) show larger shifts for the quasi-guided modes than LSPR ones. For a relative pressure change ( $P/P_s$ ;  $P$  = IPA pressure,  $P_s$  = IPA saturation vapor pressure) from 0.002 to 1.0, the quasi-guided mode shifts from 505 to 551 nm ( $\Delta\lambda = 46$  nm). In contrast, the LSPR mode shifts from 601 to 618 nm ( $\Delta\lambda = 17$  nm), making the hybridization important for generating these quasi-modes. Note that due to the usage of a 2D array, the hybridization is polarization insensitive, unlike the 1D cases that respond to hybridization only under TM excitation. Similar polarization insensitivity can also be observed in a regular mPhC when a 2D metallic lattice is considered. Sarkar et al. have recently proposed and demonstrated FOM enhancement in a 2D-mPhCs-based sensor composed of platinum (Pt) nanodisc array and underlying titania ( $\text{TiO}_2$ ) waveguide.<sup>[97]</sup> Figure 7D-i provides a schematic representation of the hybrid structure with its simulated and experimental sensing characteristics provided in Figure 7D-ii,iii. For a variation of the cover RI using different concentrations of a glycerol solution, the changes in the transmittance spectra are evaluated for the hybrid and the photonic and plasmonic constituents. Experimental results show mPhCs sensitivity and FOM of (223 nm per

**Figure 6.** Surface lattice resonance (SLR) based sensors. A-i) Schematic showing 1D-Au lines on the ITO layer with incoming (1), reflected (2), diffracted/scattered lights (4), and RA (3). Inset shows a top-view SEM image of the fabricated structure. (ii) Sensing performance for AOI of 24° for increased glucose/water solution concentration. A-i-iii) Reproduced with permission.<sup>[291]</sup> Copyright 2015, Elsevier B.V. B-i) Schematic showing the perspective and cross-sectional view of gold nanotriangles (supported through NSL templates) on a gold surface with an underlying spacer layer. Numerical simulations showing absorption peaks as a function of environmental RI variation. B-i-iii) Reproduced under the terms of the Creative Commons CC-BY license.<sup>[294]</sup> Copyright 2018, the authors, published by Springer Nature. C-i) SEM image showing plasmonic sensor based on gold nanocube array. (ii) Transmission spectra for cover index variation with an alternative figure of merit (FOM\*) variation as a function of wavelength. C,i-iii) Reproduced under the terms of the ACS AuthorChoice License.<sup>[297]</sup> Copyright 2014, the authors, published by ACS. D-i) SEM image of a 2D array of Au disks formed through PEEL. (ii,iii) Transmission experiment and simulation performed on the fabricated array. D-i-iii) Reproduced under the terms of the Creative Commons CC-BY license.<sup>[160]</sup> Copyright 2018, the authors, published by Springer Nature. E-i) SEM images of AuNP arrays with varying diameter “ $d$ ” and periodicity “ $p$ ”: (1)  $d = 95$  nm,  $p = 400$  nm; (2)  $d = 110$  nm,  $p = 300$  nm; (3)  $d = 110$  nm,  $p = 400$  nm; (4)  $d = 110$  nm,  $p = 600$  nm; (5)  $d = 165$  nm,  $p = 400$  nm. (ii) transmission spectra for  $p = 300$  nm and 600 nm, with a fixed  $d = 150$  nm. (iii) FOM calculated from the SLR resonances as a function of  $d$  (165 nm: square, 145 nm: circle, 110 nm: triangle-up, and 95 nm: triangle-down) as well as  $p$  (300–600 nm). E-i-iii) Reproduced with permission.<sup>[287]</sup> Copyright 2011, American Chemical Society. F-i) 2D array (inset: SEM image) of assembled AuNPs for mechanical strain sensing. The effect of transformation from square to rectangular lattice upon stretching is also shown schematically. (ii,iii) Experimental and simulated extinction spectra obtained under varying strain. F-i-iii) Reproduced under the terms of the ACS AuthorChoice License.<sup>[47]</sup> Copyright 2019, the authors, published by ACS.

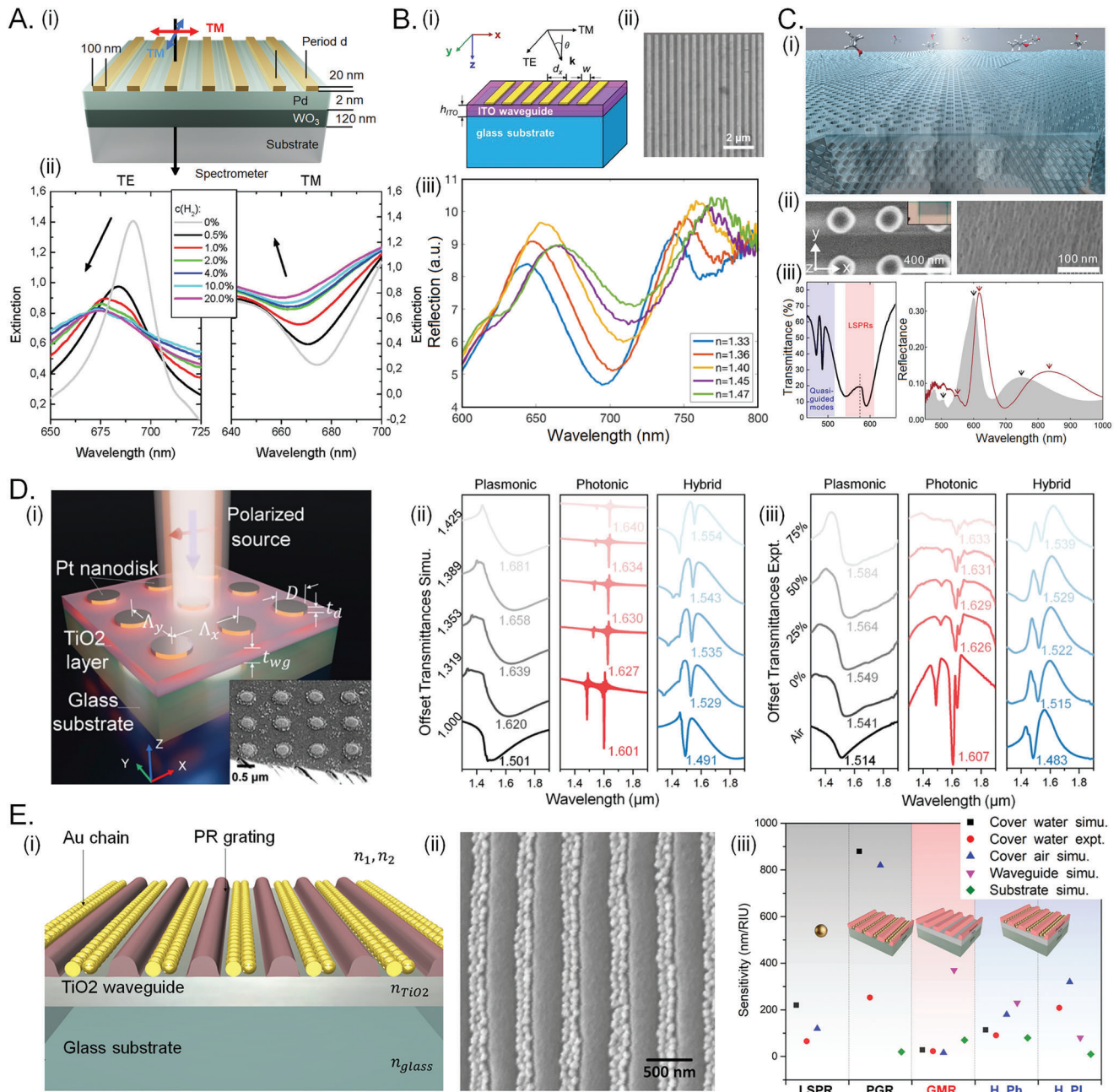


**Figure 7.** Metallic/colloidal photonic crystal slabs for sensing applications. A) Hydrogen sensing using metallic PhCs. (i) schematic of the structure, (ii) sensing of hydrogen for varied concentrations. A-ii-iii) Reproduced with permission.<sup>[301]</sup> Copyright 2010, Optica Publishing Group. B) Stable RI sensing in a cryogenic environment. (i) Schematic of the mPhCs, (ii) SEM image of the fabricated mPhCs, (iii) reflectance measurements for sensitivity calculations. B-i-iii) Reproduced under the terms of the Creative Commons CC-BY license.<sup>[302]</sup> Copyright 2019, the authors, published by Optica. C) Isopropanol vapor sensing using plasmonic Al nanocylinder array embedded in a mesoporous silica layer. (ii) SEM image of the Al cylinders (left) and the silica layer (right). (iii) Transmittance spectra for mode identification with sensing study, carried under reflectance measurements. C-i-iii) Reproduced under the terms of the ACS AuthorChoice License.<sup>[304]</sup> Copyright 2020, the authors, published by ACS. D) 2D-mPhCs composed of Pt nanodisc array and  $\text{TiO}_2$  waveguide. Inset shows an SEM image of the plasmonic lattice over the photonic waveguide. (ii,iii) Simulated and experimental sensitivity performance of the hybrid structure compared to its constituent photonic and plasmonic blocks. D-i-iii) Reproduced under the terms of the Creative Commons CC-BY license.<sup>[97]</sup> Copyright 2022, the authors, published by Wiley VCH. E) Colloidal PhCs formed using plasmonic AuNP grating arranged over a dielectric grating-waveguide structure. (i,ii) Schematic of the cPhCs structure and its SEM image (top-view). (iii) Sensitivity comparison for different modes. E-i-iii) Reproduced under the terms of the Creative Commons CC-BY-NC-ND license.<sup>[25]</sup> Copyright 2019, the authors, published by ACS.

RIU, 6), in contrast to (65 nm per RIU, 2) and (408 nm per RIU, 1) for the photonic and plasmonic counterparts, respectively. It is also noteworthy to mention that, apart from RI sensing, mPhCs with 1D metallic grating and polymer waveguide have also been fabricated and introduced as microforce detectors for detecting angle, strain, force, and torque.<sup>[305]</sup>

Following the concepts of metallic PhCs, we, as the König group, have proposed and demonstrated novel colloidal PhCs, where the plasmonic counterpart in the hybridization model comprises plasmonic nanoparticle chains. Previously, single nanoparticle-based coupling of particle plasmon resonance with a 1D guided-mode resonant photonic crystal has been demonstrated by Liu et al.<sup>[188]</sup> The nanoantenna–microcavity hybrid strategy was employed to enhance localized fields of AuNR for increasing SERS signal intensity under resonant conditions. A similar structure has also been used for the digital detection of microRNA under photonic resonator absorption microscopy.<sup>[306]</sup> Compared to a single NP, a plasmonic NP chain can offer additional longitudinal modes existing along the chain length that has found applications in sensing,<sup>[307]</sup> energy transportation,<sup>[308]</sup> and the formation of plasmonic NP grating.<sup>[189]</sup> It has also been previously demonstrated that the aggregation of nanoparticles into pores can result in higher RI sensing<sup>[309]</sup>; the plasmonic chains as AuNPs within trenches of the resist template (without any waveguide) have shown higher sensitivity to surrounding index variation in comparison to single AuNPs in solution form.<sup>[25]</sup> Hence, an effective assembly of colloidally grown NPs as plasmonic chains into the trenches of a dielectric grating-waveguide resonator (Figure 7E-i,ii) through the TASA technique results in a new type of hybrid resonant device,<sup>[25]</sup> aka the cPhCs.<sup>[50]</sup> The photonic guided mode can be coupled to the longitudinal chain modes by choice of grating periodicity and waveguide thickness, making plasmon-photon coupling possible under TE excitation. By selection of periodicity, the TM mode corresponding to single particle resonance can also be coupled in such cPhCs.<sup>[20]</sup> A systematic comparison is carried out by different region-specific (cover/waveguide/substrate) alterations of the RI and according to relevance in the FDTD-calculated sensitivity of the observed modes. For the experimental counterpart, the cover RI is varied using different concentrations of salt solution and sensitivity of the constituent and hybrid modes are obtained. The values of sensitivity single particle LSPR, plasmonic grating resonance, photonic waveguide resonance and the hybrid resonances are given in Figure 7E-iii. Such cPhCs, also find notable importance in plasmon-induced hot electron generation, charge transfer, and photocatalysis due to the high-Q values of the hybrid mode.<sup>[20,50]</sup>

#### 4.3. Hybrid GMR Sensing

For hybrid GMR-based sensing, the structure itself is a hybrid; these contain both metallic–dielectric interfaces for generating surface plasmon polariton modes and grating-waveguide configuration for excitation of the GMR modes. Unlike mPhCs, a continuous metallic layer is present below the waveguide, which only allows the structures to be characterized in reflectance. Due to this additional metallic layer, a spectrum-inversed response can be found in metal-assisted guided-mode resonant (MaGMR) systems.<sup>[199]</sup> Figure 8A-i exhibits an SEM cross-sectional image

of the structure fabricated in sequential processes of e-beam deposition of Au layer, PECVD of silicon nitride ( $\text{Si}_3\text{N}_4$ ) layer, resist coating, LIL patterning, transfer of 1D-grating onto  $\text{Si}_3\text{N}_4$  surface using dry etching. A large-scale photograph of the actual sample is also provided, showing the advantages of LIL for sample fabrication. Figure 8A-ii provides the spectral response under TM polarization where, instead of a GMR reflectance peak, a MaGMR reflectance dip is experimentally observed and supported by FDTD modeling. The inset shows an asymmetric electric field in the waveguide region, obtained at the calculated reflectance minima. Figure 8A-iii provides a real-time sensorgram of the MaGMR dip that corresponds to the spectral position of the dip as a function of cover RI. Compared to a normal GMR, involving a metallic layer allows enhanced bulk RI sensitivity due to strong asymmetric field distribution towards the cover region; MaGMR shows a sensitivity of 376.78 nm per RIU in contrast to 103.29 nm per RIU from a typical GMR structure, operating at similar wavelength. Next, a 2D-MaGMR structure is explored (Figure 8B-i,ii) that consists of EBL-fabricated SU-8 nanopillars (nelloid configuration) on top of an aluminum layer.<sup>[197]</sup> Instead of a separate waveguide layer, the grating layer can also participate in waveguiding<sup>[205]</sup> to exhibit hybrid modes. Using FDTD modeling and experimental spectroscopy, the TM polarized reflectance spectra show the presence of two resonant dips, i.e., the D (640 nm) and M (840 nm) modes. From the electric field distribution, it can be identified that the “D-mode” is the MaGMR existing within the waveguiding layer, whereas the ‘M-mode’ is the SPP existing in the metal-grating interface. For the sensing measurements, the change of spectral position is recorded as a function of surface layer growth ( $S = \Delta\lambda/\Delta t$ ;  $t$  = grown layer thickness), whereas  $\text{FOM} = S/\text{FWHM} = (\Delta\lambda/\Delta t)/\text{FWHM}$ ;  $\text{FOM}_D$  and  $\text{FOM}_M$  are experimentally obtained as  $0.127 \text{ nm}^{-1}$  and  $0.021 \text{ nm}^{-1}$ , respectively, showing an advantage of the hybrid D mode, over the regular M mode. Using such a D-mode, biosensing is confirmed through spectral shifts for HEPES and BSA adsorption, as shown in Figure 8B-iv. Note that in the 1D-MaGMR case discussed in Figure 8A, having a separate waveguide, only the D-mode is observed. Similar to the 2D-square array, a 2D-hexagonal array of the grating can also support MaGMR modes<sup>[51]</sup>; however, it is convenient to describe the modes as TE-like and TM-like, according to the polarization configurations for such a hexagonal lattice. Using FDTD-based theoretical analysis on the 1D grating, 2D-square grating, and 2D hexagonal grating, MaGMR structures retain supremacy over GMR structures regarding the calculated sensitivities.<sup>[51]</sup>

In contrast to MaGMR structures, where the metallic film lies below the waveguiding layer, specific hybrid geometries can also have a metallic layer above the grating. Such mixed metal–dielectric nanograting structures<sup>[203]</sup> exhibit GMR-SPP resonances under TM polarized excitations. Electric field distributions generally confirm the dual nature of the GMR-SPP mode with simultaneous waveguiding and SPR excitation. A more general case is exhibited in Figure 8C-i, where a metal–dielectric grating is placed over a metal-dielectric waveguide (MDMD) structure<sup>[204]</sup> with a material composition of  $\text{Ag}/\text{Si}_3\text{N}_4/\text{Ag}/\text{Si}_3\text{N}_4/\text{SiO}_2$ . The magnetic field distribution ( $|H_y|$ ) at two resonant wavelengths are plotted in Figure 8C-ii, where the left panel shows the GMR-SPP mode in comparison to the SPP mode in the right panel. The sensing capabilities

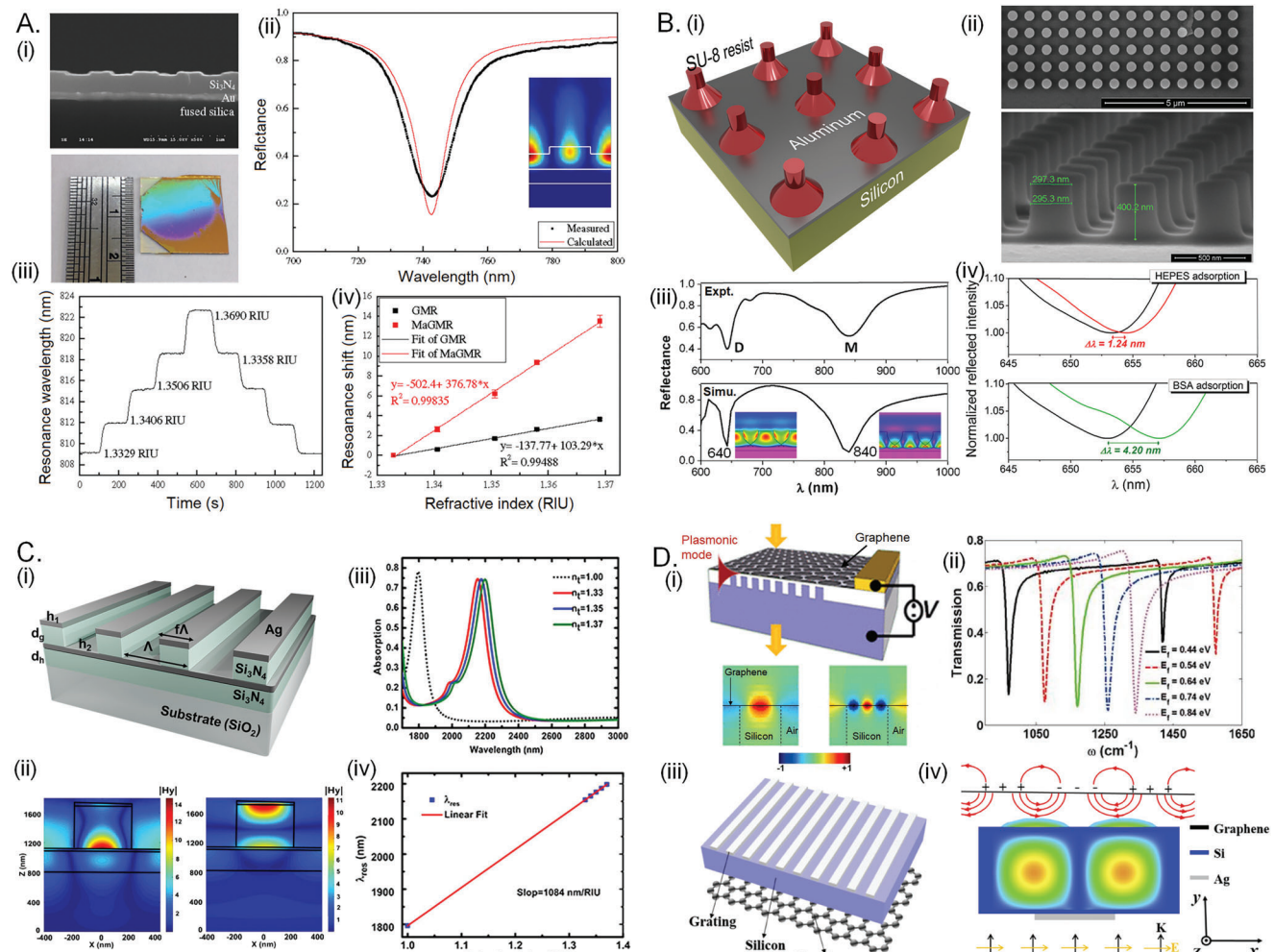


**Figure 8.** Hybrid GMR geometries for sensing applications. A) MaGMR structure with a spectrum-inverse response and high sensitivity. (i) SEM cross-section of the structure along with a real-life photograph of the fabricated sample. (ii) Measured calculated reflectance spectra under TM polarization. (iii,iv) Sensing response of the structure in comparison to normal GMR. A-i-iv) Reproduced under the terms of the Creative Commons CC-BY license.<sup>[199]</sup> Copyright 2012, the authors, published by Optica. B) 2D-MaGMR structure in SU-8 pillar array. (i) Schematic of the configuration, (ii) SEM image of the fabricated structure in top and cross-sectional view. (iii) Experimental and calculated reflectance spectra with inset showing electric field plot. (iv) Spectral shift for biosensing application using the sensitive D mode. B-ii-iv) Reproduced with permission.<sup>[197]</sup> Copyright 2015, Elsevier B.V. C) Mixed metal-dielectric nanograting-waveguide structures. (i) Schematic showing MDMD structure on a substrate, (ii) Magnetic field distribution showing two modes. (iii,iv) Sensitivity for cover RI variation is numerically calculated. C-ii-iv) Reproduced with permission.<sup>[204]</sup> Copyright 2018, Optica Publishing Group. D) Hybrid GMR structures composed of plasmonic graphene. (i) Schematic showing graphene plasmonic excitation by a silicon grating. Electric field distributions are provided for fundamental (left) and higher-order (right) hybrid GMR modes. (ii) Simulated transmission spectra for variation of Fermi energy level in graphene. (iii) metal grating-dielectric waveguide structure with a graphene layer. (iv) Mechanism of excitation of hybrid GMR modes. D-i,ii) Reproduced with permission.<sup>[53]</sup> Copyright 2012, American Chemical Society. D-iii,iv) Reproduced under the terms of the Creative Commons CC-BY license.<sup>[209]</sup> Copyright 2020, the authors, published by Optica.

of such MDMD design are shown in Figure 8C-iii,iv, where a sensitivity of 1084 nm per RIU and a FOM of  $\approx 23$  are reported by changing the cover index. For a more straightforward case of metallic grating on a dielectric waveguide to result in hybrid GMR, Tan et al. have fabricated as well as calculated electric field profiles showing SPP at metal/cover and metal/waveguide interface and GMR within waveguide under normal incidence. By changing the angle of incidence, hybrid modes can be excited in such structures.<sup>[201]</sup> The concepts of hybridization in grating-waveguide-based structures can be further extended by considering multi-layered nanopillar grating. For the

nanopillar array, composed of metal–dielectric–metal, the applications get broadly categorized into the development of perfect absorbers,<sup>[310]</sup> SERS detection,<sup>[311]</sup> and sensing.<sup>[312]</sup> For hybrid GMR-based sensing,<sup>[313]</sup> composite nanopillars of entirely dielectric materials (silicon nitride–silica–silicon nitride) placed over gold-coated substrate give rise to a combination of three sensing mechanisms: magnetic dipole resonance, substrate mode resonance, and metal-assisted guided-mode resonance. Numerical investigation on cover RI sensing highlights the highest sensitivity of the hybrid GMR mode of 672 nm per RIU with an FWHM of 0.64 nm and FOM of 1050.

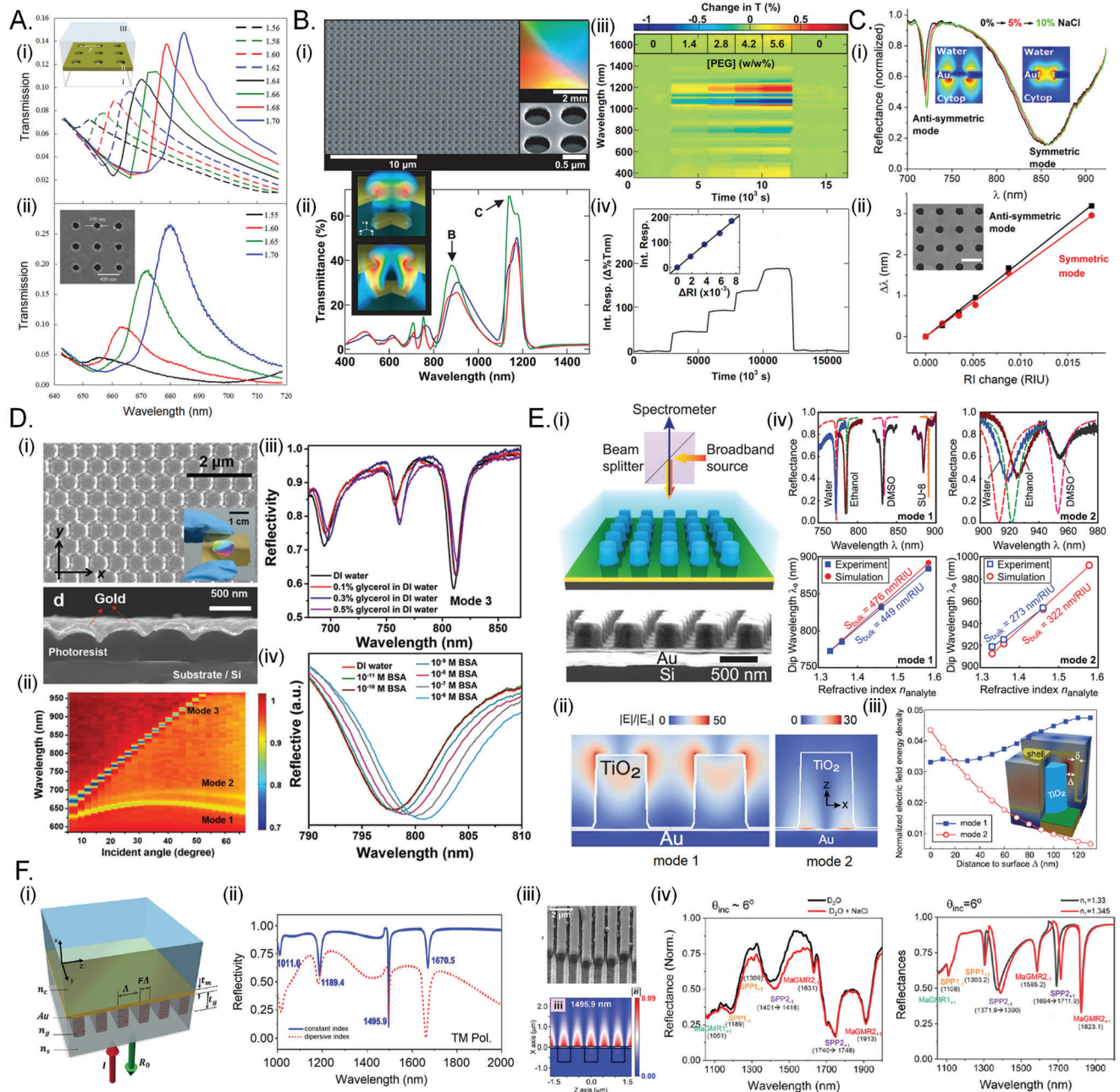
Incorporating a graphene layer as an active plasmonic component is an important addition to this hybrid-GMR-based resonators/sensors category. Figure 8D-i exhibits an etched diffractive grating on silicon that can effectively generate tightly confined plasmonic waves (shown via electric field distribution) in a single graphene layer.<sup>[53]</sup> Combining this structure with guided-wave resonance results in a distinct dip in the transmission spectra when the incident optical wave interacts with the graphene plasmonic wave at normal incidence. The proposed hybrid-GMR configuration holds potential for versatile applications such as a tunable optical filter. Since the resonant wavelength can be easily and extensively adjusted by making minor modifications to the Fermi energy level of the graphene, this can act as a sensor to detect the variation of external bias voltage. Further, by associating a metallic grating-dielectric waveguide to the graphene layer (Figure 8D-iii), graphene-surface plasmon polaritons (GSPP) can be excited to form hybrid GMR-GSPP modes.<sup>[209]</sup> The associated mechanism is described in Figure 8D-iv. Metallic grating enables efficient coupling of TM waves at specific resonant frequencies into the GMR modes of the dielectric waveguide. The GMR modes experience total internal reflection at the interface between the waveguide and vacuum, generating evanescent fields in the empty space. When the energy and momentum conservation requirements are met, the evanescent-field-mediated GMR-GSPP modes can be initiated, effectively concentrating the electromagnetic energy into the subwavelength vacuum gap. In contrast to conventional GSPPs with low-quality factors, the strongly-coupled GMR-GSPP hybrid modes introduce highly sharp features in the reflection spectra. The hybridization mechanism allows the production of highly sensitive sensors, compatible with planar fabrication techniques, that can be spectrally tuned through electrical or mechanical perturbations. On a separate note, wavelength interrogation-based sensing studies have been considered throughout the section. Instead, angular-based interrogation using a monochromatic light source can also be performed on such a hybrid GMR structure, where TE and TM excitation classifies the resonance type without and with the involvement of SPP modes.<sup>[198]</sup> For a photore sist grating on gold thin film, a sensitivity of 123° per RIU and an FWHM of 1.2° was experimentally observed (TE pol. excitation) using a 632.8 nm laser source.

#### 4.4. Hybrid SPP Sensing

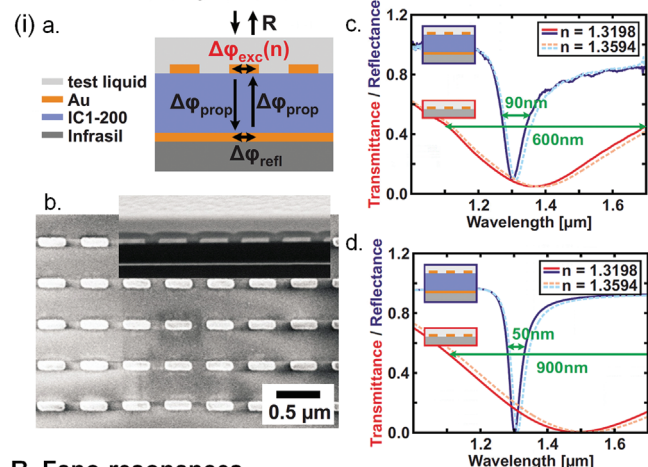
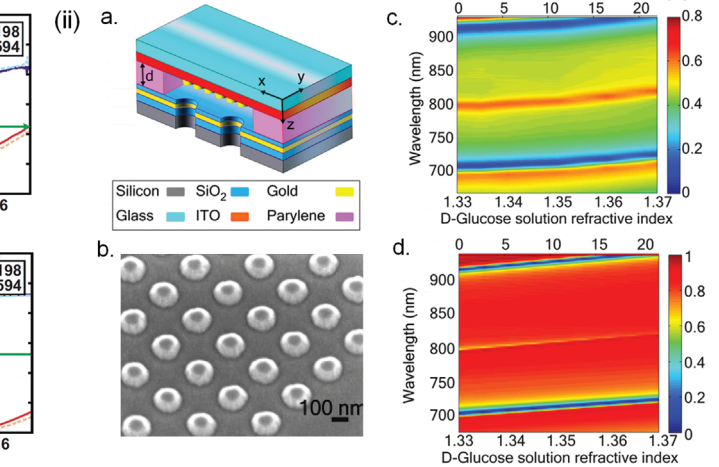
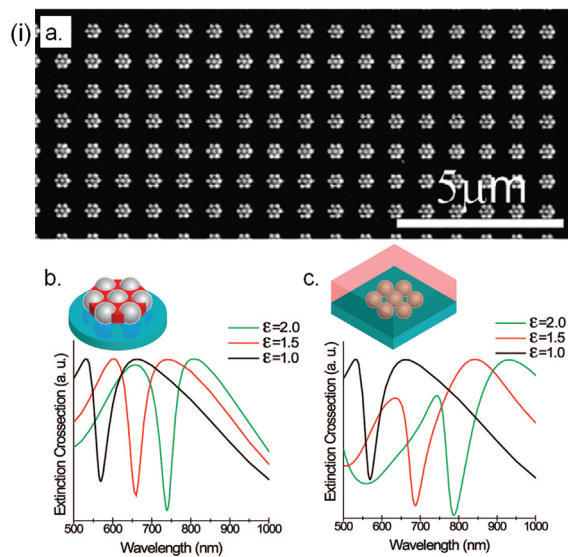
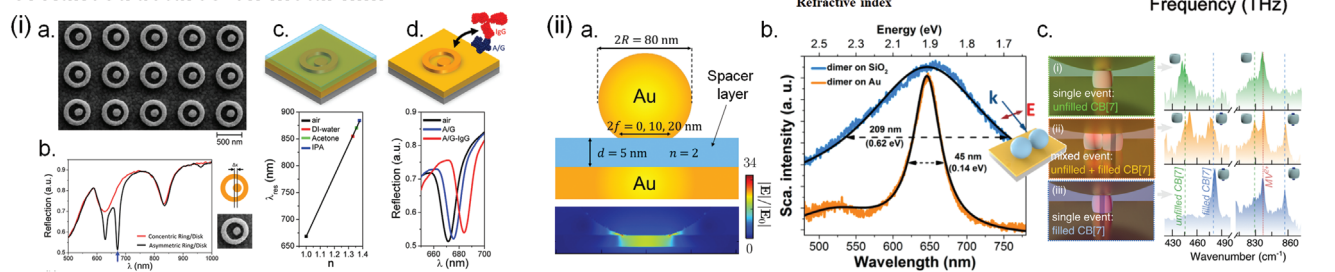
Generally, the hybrid SPP referred to in this review consists of the interaction of SPP modes with the RA. As discussed before, RA is sensitive to the refractive index of the diffracted medium. Figure 9A-i,ii shows the simulated and experimental transmittances of a 2D nanohole Au array supported on a glass substrate. When the cover index is gradually increased and attains a value close to 1.7, there is a coupling of the RA mode of the cover with the SPP mode of the metal–substrate interface, showing an increase in amplitude by 65% per RIU for simulation and 150% per RIU for the experiment, with a spectral sensitivity of  $\approx$ 200 nm per RIU for both the cases. Inset shows the design geometry and SEM image of the nanohole array.<sup>[54]</sup> For such a metallic nanohole array, the geometric features of the holes affect the lifetimes of the excited SPP-BWs.<sup>[314]</sup> As an extension of RA-SPP

hybridization, an additional nanodisc array near the nanohole array can result in a quasi-3D plasmonic crystal.<sup>[210]</sup> Because of the plasmonic disc, LSPR modes can couple with the RA-SPP mode, leading to complex transmission spectra with high sensitivity to structural features. Figure 9B-i shows an SEM image of such plasmonic crystal, formed by NIL in photocurable polyurethane, followed by directional deposition of the Au layer, without any lift-off step. Figure 9B-ii shows the transmission spectra with two peaks corresponding to LSPR behavior from the rims of a single nano well (peak B) and the other at higher wavelengths corresponding to the coupling of LSPR with the RA-SPP mode (Peak C). These are confirmed by the corresponding field profiles provided in the inset. Figure 9B-iii,iv corresponds to the sensing performance of the structure on increased injection of PEG solution over time, where a change in transmittance is recorded for varied PEG concentration along with a spectral sensitivity of 700–800 nm per RIU and intensity-based sensitivity of 2.5–3.5 Abs per RIU, which are relatively higher compared to that of a single 2D nanohole array. Next, an Au nanohole array with water-index matched cytop film coating<sup>[315]</sup> (to create a symmetric environment for sensing) is shown in Figure 9C. Bulk RI sensing offers symmetric and anti-symmetric bright dipolar modes with a measured Q factor of 10.3 and 143, respectively, and corresponding surface sensitivities of 10.62 nm per RIU and 1.85 nm per RIU.

Shifting our focus from nanohole structures, a highly sensitive plasmonic sensor with ultrahigh FOM<sup>[316]</sup> is discussed in Figure 9D. Periodic plasmonic array structures with minimized feature sizes can narrow the resonance line widths. Figure 9D-i shows the hexagonal array formed from LIL and the e-beam vacuum deposition technique. The FWHM of the SPP mode from a hexagonal lattice is directly related to the size of the scatters, reducing which (in this case, the depth of the crevices) can result in a narrowing of line widths. Increasing the exposure time for negative resist-based LIL can efficiently reduce the depths, resulting in lineshapes with FWHM as low as 3 nm. Figure 9D-ii shows the reflectance as a function of the incident angle. For bulk solution sensing, a shift of 3.5 nm is observed for a  $\Delta n$  of 0.0006, leading to a sensitivity of 5833 nm per RIU and a FOM of 730 for the sensor operating at an AOI of  $\approx$ 8° (Figure 9D-ii). Figure 9D-iii shows actual biosensing with the SPP sensor for detecting BSA with concentration as low as  $10^{-10}$  M. Shifting from corrugated structures, Figure 9E-i exhibits the dielectric nanopillars on a metallic surface, with a corresponding SEM image of the sample, fabricated using soft lithography techniques. It should be noted that the hybrid-SPP mode is not a guiding mode but a lattice mode<sup>[317,318]</sup> formed by the coupling of RA and SPP modes, unlike the hybrid-GMR modes (Section 4.3). The simulated reflectance spectra of such structure exhibit a narrow line shape for the hybrid SPP mode (mode 1) and moderate lineshape for the regular SPP mode (mode 2), along with the electric fields, shown in Figure 9E-ii. As seen from the figure, one can confirm that the hybrid-SPP modes are positioned on the upper portion of the pillars, thus more exposed to the surrounding. Mode 1, having more electric fields located within the analyte, is more sensitive to the external index variation. The distribution of the modes is quantified in Figure 9E-iii by calculating the normalized electric field energy density within a shell volume plotted as a function of the distance from the pillar surface. Figure 9E-iv shows the sensing performance of both modes for the experimental cover index vari



**Figure 9.** Hybrid SPP geometries for sensing applications. A) RA-SPP hybridization in a 2D array of nanoholes in Au film, supported with a glass substrate. (i,ii) Simulated and experimental transmission characteristics near the hybridization with insets showing the fabricated structure's structural geometry and the SEM image, respectively. A-i,ii) Reproduced under the terms of the Creative Commons CC-BY license.<sup>[54]</sup> Copyright 2007, the authors, published by Optica. B) Quasi-3D plasmonic crystals for biosensing. (i) SEM image of the fabricated structure, (ii) experimental and modeled transmittances with 3D field profiles. (iii,iv) change of transmittance as a function of increased PEG concentration. B-i-iv) Reproduced under the terms of the Creative Commons CC-BY license.<sup>[210]</sup> Copyright 2006, the authors, published by NAS. C) Sensing studies with high Q hybrid modes in plasmonic nanohole array. (i) Reflectance profile showing two modes and their electric field profile. (ii) Shifting of resonant wavelength for both modes as a function of RI of the cover (datapoints at 0%, 1%, 2%, 3%, 5%, and 10% of NaCl soln.). Reproduced with permission.<sup>[315]</sup> Copyright 2019, American Chemical Society. D) Plasmonic array sensor with ultrahigh FOM. (i) SEM image of the fabricated structure. Inset shows a photographic image of the actual sample. (ii) Angular dependence of reflectance. (iii-iv) sensing studies of the sensor, showing ultrahigh FOM of 730. D-i-iv) Reproduced with permission.<sup>[316]</sup> Copyright 2018, Wiley-VCH. E) Hybrid SPP modes in low-index-contrast dielectric lattices on metal. (i) Structural design with SEM image of the nanopillar array. (ii) Simulated reflectance spectra. (iii) Electric field profile of the two modes. (iv) sensing performance of the hybrid resonant structure. E-i-iv) Reproduced with permission.<sup>[55]</sup> Copyright 2020, Wiley-VCH. F) Grating coupled SPP at the flat metal-analyte interface using a hybrid geometry. (i) Schematic configuration, (ii) FDTD calculated reflectance under TM pol., considering both constant and dispersive dielectric grating index. (iii) H-field plot for the SPP resonance at the cover region, (iv) SEM image of the fabricated structure, (v) Sensing study under experimental and simulation conditions. F-i-v) Reproduced with permission.<sup>[56]</sup> Copyright 2020, American Chemical Society.

**A. LSPR + Cavity modes****B. Fano resonances****C. Nanostructures on metal film**

**Figure 10.** LSPR coupling to other modes for sensing applications. A) Fabry Perot cavity modes. (i) Cavity-enhanced LSPR sensing: a cross-sectional schematic of the structure with dielectric cavity enclosed between AuNR array and Au mirror; b) SEM image of the AuNR array with inset showing FIB-cut cross-sectional profile; c) Transmittance for “bare AuNR array” and reflectance for “AuNR array + cavity” plotted experimentally as a function of two different cover indices; d) same comparison obtained via simulations. A,i) Reproduced with permission.<sup>[326]</sup> Copyright 2010, AIP Publishing. (ii) Cavity coupled device with enhanced S and FOM: a) schematic of the cavity-coupled plasmonic device; b) 2D-array of Au nanodisks on ITO-coated substrate; c) experimental reflection spectra as a function of wavelength and D-glucose solution refractive index; d) similar color plots obtained through numerical simulations. A,ii) Reproduced with permission.<sup>[96]</sup> Copyright 2015, American Chemical Society. B) Fano resonances in plasmonic nanostructures. (i) Sensing with plasmonic oligomers: a) SEM image of Au heptamer array formed through EBL; b,c) extinction spectra as a function of dielectric permittivity for partial and complete surroundings. B-i) Reproduced with permission.<sup>[327,328]</sup> Copyright 2010 and 2009, American Chemical Society. (ii) Asymmetric coupling between sub- and super-radiant modes in split ring resonators (SRR): a) transmission spectra for single SRR (both narrow and wide, upper row) and asymmetrically coupled SRR (with different spacing, lower row); b) sensitivity studies for single, symmetric, and asymmetric SRRs. B,ii) Reproduced under the terms of the Creative Commons CC-BY license.<sup>[329]</sup> Copyright 2009, the authors, published by Optica. (iii) Planar metamaterial for plasmonic sensing: a. Image of the sample with inset showing magnified view; b. reflectance spectra as a function of cover refractive index with an inset

ation. Bulk RI sensitivity of 448 nm per RIU for the hybrid-SPP mode in contrast to 273 nm per RIU of the normal SPP mode is experimentally achieved. The hybrid-SPP mode also shows a Q-factor of 300 and a FOM of 180, which is quite impressive. Interestingly, a similar hybrid-SPP mode in a recent numerical calculation-based work reports a sensitivity of 717 nm per RIU with  $Q \approx 16\,000$  and FOM of 15930 per RIU.<sup>[319]</sup>

Other configurations of hybrid SPP sensors can be introduced by considering a flat metallic surface for sensing. Most resonant geometries discussed so far contain grating in the cover region, which may create a hindrance when sensing large biomolecules is considered. Instead, a flat metallic film with underneath dielectric grating (in the substrate region) can produce hybrid SPP and hybrid GMR resonances within the dielectric grating and a pure SPP mode on the cover side, given that the light is incident from the substrate side.<sup>[320]</sup> Following the simulation-based works of Abutoama et al.,<sup>[321]</sup> Joseph group has established an SPP sensor in hybrid configuration<sup>[56,322]</sup> that uses SPP modes on a flat surface with larger penetration depth for biosensing purposes. Figure 9F-i,ii shows the proposed structure with its TM polarized normal incidence reflectance spectra. The plasmonic mode of interest arising in the analyte medium is demonstrated via the magnetic field plot (Figure 9F-iii) with SEM images of the fabricated device in Figure 9F-iv. The sensing performances are evaluated experimentally under oblique incidence for an AOI of 6° for cover index variation using a salt solution, with similar studies performed using FDTD simulations. An experimental sensitivity of 1133 nm/RIU is reported with a FOM of 12. It should also be noted that similar dielectric grating on the metallic surface has been of current research interest for producing a bound state in a continuum<sup>[323,324]</sup> using plasmonic–photonic hybridization in resonant metal-dielectric grating<sup>[202,325]</sup> that offers high-Q modes for different applications.

#### 4.5. Other Architectures of Plasmonic Hybridization-Based Sensors

Apart from the hybridization between the defined plasmonic (SPP, LSPR) and photonic (RA, GMR) constituents, other types of hybridization can also occur for nanophotonic architectures. The LSPR modes from metallic nanostructures can also couple with different photonic and plasmonic modes to produce high Q-modes in distinct hybrid geometries. Figure 10A-i,ii shows

LSPR and photonic Fabry-Perot (FP) cavity modes in dielectric thin films. By arranging a metallic nanorod array on one of the surfaces of the cavity, the photonic cavity modes can be coupled to the LSPR modes of the nanorods for cavity-enhanced LSPR sensing.<sup>[326]</sup> Such FP-LSPR-based coupled systems can signifi-

cantly lower the spectral linewidth and increase the near-field intensity compared to the plasmonic nanostructure, making it applicable for RI sensing with high FOM.<sup>[326,335]</sup> Figures 10B-i discusses the existence of Fano-type asymmetric line shapes<sup>[336,337]</sup> in plasmonic oligomers or clusters due to the radiative coupling between broad dipolar LSPR mode (super-radiant) and narrow multipolar (sub-radiant) modes.<sup>[143,338]</sup> These Fano-modes in plasmonic nanostructures hold promising implementations in SERS detection<sup>[339]</sup> and sensing applications.<sup>[328–330,340]</sup> For example, Figure 10B-ii shows the RI sensing capabilities of different types of uncoupled and coupled split ring resonators (SRR), with the highest sensitivity for the asymmetrically coupled case. For metamaterial structures (cut-out gold film, Figure 10B-iii) supporting optically bright dipole antenna and optical dark quadrupole antenna, reflectance spectra show features similar to electromagnetic-induced transparency. Using such coupling effects, a sensitivity of 588 nm per RIU and FOM of 3.8 is reported.<sup>[330]</sup> Figure 10C discusses the cases of nanostructure array on additional metallic film. Figure 10C-i shows a Fano resonant asymmetric ring/disk plasmonic nanocavity system offering enhanced electromagnetic fields with RI sensitivity of 648 nm per RIU and a large FOM of value 72.<sup>[331]</sup> Reliable protein mono- and bilayer detection have also been demonstrated (Figure 10C-ic,d). Figure 10C-ii shows the investigation of the plasmonic gap mode while considering nanostructures on the metal film, separated by a spacer layer (Figure 10C-ii-a). These gap modes can exist between two plasmonic nanoparticles<sup>[341]</sup> as well as between a single particle and a metal film,<sup>[332]</sup> leading to near-field coupling/hybridization of the plasmonic resonances and red-shifting of the nanoparticle-associated LSPR mode. Figure 10C-ii-b shows the direct effect of this metallic layer in the narrowing of the resonance line widths, which is desired in sensing techniques. Due to the tight localization of the optical modes within the nano-volumed gaps, highly intensified electric fields provide extremely high sensitivity, down to a single molecular reaction for SERS detection.<sup>[342]</sup> Figure 10C-ii-c shows the Raman signals observed for the various gap contents, and its arrangements showcase the capacity to observe molecular reactions on a nanoscale level.<sup>[334]</sup>

#### 5. Conclusion and Prospects for Plasmonic Hybridization Sensors

We have shown that one efficiently realizes the demanding requirements for the next generation of refractive index sensors by applying innovative concepts through available optical design, materials, and fabrication methods. The game changer for this development is the concept of plasmonic hybridization combined with the development of lithographic nanostructuring, synthesis

showing an enlarged figure of reflectance peaks as highlighted by the dashed box. B,iii) Reproduced with permission.<sup>[330]</sup> Copyright 2010, American Chemical Society. C) Nanostructures on a metallic mirror. (i) Asymmetric ring-disc system on conducting layer: a) SEM image of the fabricated array; b) experimental reflectance, compared with symmetric structure; c,d) sensitivity study with bulk solutions and antigen-antibody. C,i) Reproduced with permission.<sup>[331]</sup> Copyright 2012, American Chemical Society. (ii) nanoparticle on mirror geometry: a) schematic of AuNP on Au film, separated by spacer layer that allows strong electric field confinement in the gap region; b) plasmon hybridization through the metal mirror for linewidth narrowing; c) single molecular reaction observation through SERS enhancement. C-ii-a) Reproduced under the terms of the Creative Commons CC-BY license.<sup>[332]</sup> Copyright 2018, the authors, published by EDP Sciences. C-ii-b,c) Reproduced with permissions.<sup>[333,334]</sup> Copyright 2017 and 2016, American Chemical Society.

of plasmonic nanoparticles, and directed self-assembly. We have comprehensively reviewed five main categories of plasmonic hybridization and their application as sensors. These are i) surface lattice resonances, ii) metallic/colloidal photonic crystal slabs, iii) hybrid guided-mode resonances, iv) hybrid surface plasmon polariton, and v) other hybrid plasmon resonance-based sensing studies. For this, we have covered the basic principles of the underlying core components of plasmonic LSPR and SPP sensors, along with the photonic RA and GMR properties. The plasmonic LSPR and SPP-based sensors can offer higher bulk RI sensitivities, in general, because of the more extensive interaction of the resonant modes and the analyte in the cover region, along with options to tune the resonant wavelength over the visible and NIR wavelengths. On the other hand, photonic sensors like GMR offer very high FOM due to low losses but comparatively lower sensitivity due to the lesser interaction of the resonant modes with the analyte. Using hybrid modes with low losses and high-Q factors, we come closer to the challenges of a reliable, fast, and inexpensive sensor that can read out quickly, even without using an energy source (utilizing significant color change through resonance wavelength shift).

We believe changes can be made to the following components to exploit the potential of hybrid modes for sensing fully. The most straightforward solution would be to reduce the operating temperatures, which contradicts the need for mass production. Nevertheless, the study at low temperatures shows the potential, where the metal has almost no scattering of free electrons. Zayats' group shows this with metallic nanostructures and metal films, where the extinction changes by nearly a factor of 10, while the temperature effects are relatively weak in plasmonic crystals.<sup>[343]</sup> This low-temperature study shows that the plasmonic structure also influences the temperature dependence of the optical properties.

Much potential for improvement lies in the interaction between the nanoparticles and the interaction with the substrate. Videen's group shows that the plasmonic modes are susceptible to the illumination angle and polarization in a way that depends on the nanostructures' size, shape, and substrate.<sup>[344]</sup> This numerical analysis demonstrates the critical potential of plasmonic nanoparticles in direct contact with substrates, a potential that is currently being leveraged. Lithographically fabricated metal structures can meet these requirements at the price of surface roughness, limited size, and shape. Synthesized plasmonic nanoparticles are compelling in their shape diversity and crystallinity at the expense of having a stabilizing ligand. The surface functionalization required for this to induce desired reactions is covered by other review articles<sup>[345,346]</sup> and can be adapted for hybrid optical sensors.

So far, an underutilized component to improve sensors' optical performance is the use of gain materials. Dereux's group used a doped plasmonic waveguide and showed a 27% increase in propagation length from stimulated emission.<sup>[347]</sup> A similar approach was followed by Cai and co-workers, who used a gain-assisted resonator to compensate for the caused losses many times.<sup>[348]</sup> A precise optical design is mandatory for gain-assisted plasmonic setups to fully exploit the coherent coupling between plasmonics and the gain material.<sup>[349]</sup> Furthermore, photostable quantum emitters are also suitable for using nonlinear optical properties for sensing.<sup>[232]</sup> With the so-called semiconductor nanocrystals, a

stable, versatile, and inexpensive gain material is available,<sup>[350,351]</sup> which is currently in the early stages of being used for sensing.

## Acknowledgements

The Volkswagen Foundation financially supports this project through a Freigeist Fellowship to TAFK.

## Conflict of Interest

The authors declare no conflict of interest.

## Author Contributions

S.S. and T.A.F.K. have written the manuscript. All authors have provided critical feedback and helped to shape the research, analysis, and manuscript.

## Keywords

lithographic nanofabrication, metallic nanoparticles, nanostructures, plasmonic hybridization, self-assembly, sensing

Received: March 24, 2023

Revised: June 7, 2023

Published online: August 24, 2023

- [1] Ö. Erdem, E. Derin, K. Sagdic, E. G. Yilmaz, F. Inci, *Emergent Mater.* **2021**, 4, 169.
- [2] H. Wei, S. M. H. Abtahi, P. J. Vikesland, *Environ. Sci.: Nano* **2015**, 2, 120.
- [3] K. M. Mayer, J. H. Hafner, *Chem. Rev.* **2011**, 111, 3828.
- [4] P. Baptista, E. Pereira, P. Eaton, G. Doria, A. Miranda, I. Gomes, P. Quaresma, R. Franco, *Anal. Bioanal. Chem.* **2008**, 391, 943.
- [5] Z. Zhang, H. Wang, Z. Chen, X. Wang, J. Choo, L. Chen, *Biosens. Bioelectron.* **2018**, 114, 52.
- [6] V. M. Shalaev, S. Kawata, *Nanophotonics with Surface Plasmons*, Elsevier, Amsterdam **2006**.
- [7] S. A. Maier, *Plasmonics: Fundamentals and Applications*, Springer, Berlin **2007**.
- [8] H. Reather, *Surface Plasmons on Smooth and Rough Surfaces and on Gratings*, Springer Tracts in Modern Physics, Vol. 111, Springer, Berlin **1988**, p. 345.
- [9] J. Homola, *Chem. Rev.* **2008**, 108, 462.
- [10] M. E. Stewart, C. R. Anderton, L. B. Thompson, J. Maria, S. K. Gray, J. A. Rogers, R. G. Nuzzo, *Chem. Rev.* **2008**, 108, 494.
- [11] E. Prodan, C. Radloff, N. J. Halas, P. Nordlander, *Science* **2003**, 302, 419.
- [12] P. Nordlander, E. Prodan, *Nano Lett.* **2004**, 4, 2209.
- [13] Y. Xia, G. M. Whitesides, *Annu. Rev. Mater. Sci.* **1998**, 28, 153.
- [14] J. H. Moon, A. Small, G.-R. Yi, S.-K. Lee, W.-S. Chang, D. J. Pine, S.-M. Yang, *Synth. Met.* **2005**, 148, 99.
- [15] J. Henzie, J. Lee, M. H. Lee, W. Hasan, T. W. Odom, *Annu. Rev. Phys. Chem.* **2009**, 60, 147.
- [16] Y. Xia, N. J. Halas, *MRS Bull.* **2005**, 30, 338.
- [17] M. Grzelczak, J. Vermant, E. M. Furst, L. M. Liz-Marzán, *ACS Nano* **2010**, 4, 3591.
- [18] T. Kraus, L. Malaquin, H. Schmid, W. Riess, N. D. Spencer, H. Wolf, *Nat. Nanotechnol.* **2007**, 2, 570.

- [19] M. Mayer, M. J. Schnepf, T. A. König, A. Fery, *Adv. Opt. Mater.* **2019**, *7*, 1800564.
- [20] V. Gupta, S. Sarkar, O. Aftenieva, T. Tsuda, L. Kumar, D. Schletz, J. Schultz, A. Kiriy, A. Fery, N. Vogel, *Adv. Funct. Mater.* **2021**, *31*, 2105054.
- [21] M. Cakmak, S. Batra, B. Yalcin, *Polym. Eng. Sci.* **2015**, *55*, 34.
- [22] C. Mätzler, *Res. Rep. 2002–08*, Inst. für Angew. Phys., Bern. **2002**.
- [23] M. Moharam, T. Gaylord, *J. Opt. Soc. Am.* **1983**, *73*, 451.
- [24] M. N. Polyanskiy, Refractive index database, <https://refractiveindex.info> (accessed: March 2023).
- [25] S. Sarkar, V. Gupta, M. Kumar, J. Schubert, P. T. Probst, J. Joseph, T. A. F. König, *ACS Appl. Mater. Interfaces* **2019**, *11*, 13752.
- [26] D. Wencel, T. Abel, C. McDonagh, *Anal. Chem.* **2014**, *86*, 15.
- [27] N. H. Mack, J. W. Wackerly, V. Malyarchuk, J. A. Rogers, J. S. Moore, R. G. Nuzzo, *Nano Lett.* **2007**, *7*, 733.
- [28] G. Turhan-Sayan, *J. Lightwave Technol.* **2003**, *21*, 805.
- [29] U. Biswas, J. K. Rakshit, J. Das, G. K. Bharti, B. Suthar, A. Amphawan, M. Najjar, *Silicon* **2021**, *13*, 885.
- [30] L. Fu, Y. Liu, W. Wang, M. Wang, Y. Bai, E. L. Chronister, L. Zhen, Y. Yin, *Nanoscale* **2015**, *7*, 14483.
- [31] S. Foland, B. Swedlove, H. Nguyen, J.-B. Lee, *J. Microelectromech. Syst.* **2012**, *21*, 1117.
- [32] T. Maurer, J. Marae-Djouda, U. Cataldi, A. Gontier, G. Montay, Y. Madi, B. Panicaud, D. Macias, P.-M. Adam, G. Lévéque, *Front. Mater. Sci.* **2015**, *9*, 170.
- [33] M. Arjadi, K. U. Kyung, I. Park, M. Sitti, *Adv. Funct. Mater.* **2016**, *26*, 1678.
- [34] J. Jang, K. Kang, N. Raeis-Hosseini, A. Ismukhanova, H. Jeong, C. Jung, B. Kim, J. Y. Lee, I. Park, J. Rho, *Adv. Opt. Mater.* **2020**, *8*, 1901932.
- [35] S. A. Kolpakov, N. T. Gordon, C. Mou, K. Zhou, *Sensors* **2014**, *14*, 3986.
- [36] P. Berini, *Laser Photonics Rev.* **2014**, *8*, 197.
- [37] Y. Li, J. G. DiStefano, A. A. Murthy, J. D. Cain, E. D. Hanson, Q. Li, F. C. Castro, X. Chen, V. P. Dravid, *ACS Nano* **2017**, *11*, 10321.
- [38] H. Huang, S. Chen, F. Liu, Q. Zhao, B. Liao, S. Yi, Y. Zeng, *Anal. Chem.* **2013**, *85*, 2312.
- [39] Y. Zhang, Q. Fu, J. Ge, *Nat. Commun.* **2015**, *6*, 7510.
- [40] G. Gauglitz, *Anal. Bioanal. Chem.* **2005**, *381*, 141.
- [41] N. Sabri, S. Aljunid, M. Salim, R. B. Ahmad, R. Kamaruddin, *J. Phys.: Conf. Ser.* **2013**, *423*, 012064.
- [42] M. F. Ferreira, E. Castro-Camus, D. J. Ottaway, J. M. López-Higuera, X. Feng, W. Jin, Y. Jeong, N. Picqué, L. Tong, B. M. Reinhard, *J. Opt.* **2017**, *19*, 083001.
- [43] Y. Xu, P. Bai, X. Zhou, Y. Akimov, C. E. Png, L. K. Ang, W. Knoll, L. Wu, *Adv. Opt. Mater.* **2019**, *7*, 1801433.
- [44] K. Busch, G. Von Freymann, S. Linden, S. Mingaleev, L. Tkeshelashvili, M. Wegener, *Phys. Rep.* **2007**, *444*, 101.
- [45] J. D. Joannopoulos, P. R. Villeneuve, S. Fan, *Nature* **1997**, *386*, 143.
- [46] D. Khlopin, F. Laux, W. P. Wardley, J. Martin, G. A. Wurtz, J. Plain, N. Bonod, A. V. Zayats, W. Dickson, D. Gérard, *J. Opt. Soc. Am. B* **2017**, *34*, 691.
- [47] V. Gupta, P. T. Probst, F. R. Goßler, A. M. Steiner, J. Schubert, Y. Brasse, T. A. König, A. Fery, *ACS Appl. Mater. Interfaces* **2019**, *11*, 28189.
- [48] V. Gupta, O. Aftenieva, P. T. Probst, S. Sarkar, A. M. Steiner, N. Vogel, A. Fery, T. A. König, *Adv. Photonics Res.* **2022**, *3*, 2200152.
- [49] Q. Huang, T. D. Canady, R. Gupta, N. Li, S. Singamaneni, B. T. Cunningham, *ACS Photonics* **2020**, *7*, 1994.
- [50] S. Sarkar, V. Gupta, T. Tsuda, J. Gour, A. Singh, O. Aftenieva, A. M. Steiner, M. Hoffmann, S. Kumar, A. Fery, *Adv. Funct. Mater.* **2021**, *31*, 2011099.
- [51] V. Pandey, S. Pal, *Photonics Nanostruct.-Fundam. Appl.* **2021**, *43*, 100901.
- [52] R. Magnusson, H. G. Svavarsson, J. Yoon, M. Shokoh-Saremi, S. H. Song, *Appl. Phys. Lett.* **2012**, *100*, 091106.
- [53] W. Gao, J. Shu, C. Qiu, Q. Xu, *ACS Nano* **2012**, *6*, 7806.
- [54] J. M. McMahon, J. Henzie, T. W. Odom, G. C. Schatz, S. K. Gray, *Opt. Express* **2007**, *15*, 18119.
- [55] J. Dong, S. Chen, G. Huang, Q. Wu, X. Huang, L. Wang, Y. Zhang, X. Ao, S. He, *Adv. Opt. Mater.* **2020**, *8*, 2000877.
- [56] S. Joseph, S. Sarkar, J. Joseph, *ACS Appl. Mater. Interfaces* **2020**, *12*, 46519.
- [57] P. K. Sahoo, J. Joseph, R. Yukino, A. Sandhu, *Opt. Lett.* **2016**, *41*, 2101.
- [58] F. Liu, X. Zhang, *Opt. Mater. Express* **2016**, *6*, 682.
- [59] Y. Su, Z. Geng, Z. Fan, S. Wang, X. Lv, W. Fang, W. Pei, H. Chen, *Opt. Express* **2019**, *27*, 14152.
- [60] J. Yao, A. P. Le, S. K. Gray, J. S. Moore, J. A. Rogers, R. G. Nuzzo, *Adv. Mater.* **2010**, *22*, 1102.
- [61] Y. H. Ko, R. Magnusson, *Optica* **2018**, *5*, 289.
- [62] M. Shyiq Amin, J. Woong Yoon, R. Magnusson, *Appl. Phys. Lett.* **2013**, *103*, 131106.
- [63] P. Strobbia, E. Languirand, B. M. Cullum, *Opt. Eng.* **2015**, *54*, 100902.
- [64] H. Yu, Y. Peng, Y. Yang, Z.-Y. Li, *npj Comput. Mater.* **2019**, *5*, 45.
- [65] M. W. Knight, H. Sobhani, P. Nordlander, N. J. Halas, *Science* **2011**, *332*, 702.
- [66] W. Li, J. Valentine, *Nano Lett.* **2014**, *14*, 3510.
- [67] H. Chalabi, D. Schoen, M. L. Brongersma, *Nano Lett.* **2014**, *14*, 1374.
- [68] V. Dusastre, *Materials for Sustainable Energy: A Collection of Peer-Reviewed Research and Review Articles from Nature Publishing Group*, World Scientific, Singapore **2010**.
- [69] S. Mubeen, J. Lee, W.-r. Lee, N. Singh, G. D. Stucky, M. Moskovits, *ACS Nano* **2014**, *8*, 6066.
- [70] C. Clavero, *Nat. Photonics* **2014**, *8*, 95.
- [71] I. Mondal, H. Lee, H. Kim, J. Y. Park, *Adv. Funct. Mater.* **2020**, *30*, 1908239.
- [72] S. Linic, P. Christopher, D. B. Ingram, *Nat. Mater.* **2011**, *10*, 911.
- [73] X. Wang, S.-C. Huang, S. Hu, S. Yan, B. Ren, *Nat. Rev. Phys.* **2020**, *2*, 253.
- [74] S.-Y. Ding, J. Yi, J.-F. Li, B. Ren, D.-Y. Wu, R. Panneerselvam, Z.-Q. Tian, *Nat. Rev. Mater.* **2016**, *1*, 16021.
- [75] P. Kvasnička, J. Homola, *Biointerphases* **2008**, *3*, FD4.
- [76] A. V. Kabashin, P. Evans, S. Pastkovsky, W. Hendren, G. A. Wurtz, R. Atkinson, R. Pollard, V. A. Podolskiy, A. V. Zayats, *Nat. Mater.* **2009**, *8*, 867.
- [77] J. N. Anker, W. P. Hall, O. Lyandres, N. C. Shah, J. Zhao, R. P. Van Duyne, *Nat. Mater.* **2008**, *7*, 442.
- [78] S. W. Verbruggen, M. Keulemans, J. A. Martens, S. Lenaerts, *The Journal of Physical Chemistry C* **2013**, *117*, 19142.
- [79] R. Kodiyath, S. T. Malak, Z. A. Combs, T. Koenig, M. A. Mahmoud, M. A. El-Sayed, V. V. Tsukruk, *J. Mater. Chem. A* **2013**, *1*, 2777.
- [80] T. A. Konig, P. A. Ledin, J. Kerszulis, M. A. Mahmoud, M. A. El-Sayed, J. R. Reynolds, V. V. Tsukruk, *ACS Nano* **2014**, *8*, 6182.
- [81] J. J. Giner-Casares, L. M. Liz-Marzán, *Nano Today* **2014**, *9*, 365.
- [82] R. Kunz, K. Cottier, *Anal. Bioanal. Chem.* **2006**, *384*, 180.
- [83] R. Magnusson, D. Wawro, S. Zimmerman, Y. Ding, *Sensors* **2011**, *11*, 1476.
- [84] X. Fan, I. M. White, S. I. Shopova, H. Zhu, J. D. Suter, Y. Sun, *Anal. Chim. Acta* **2008**, *620*, 8.
- [85] S. Sarkar, S. Poulose, P. K. Sahoo, J. Joseph, *OSA Continuum* **2018**, *1*, 1277.
- [86] T. K. Gaylord, W. E. Baird, M. Moharam, *Appl. Opt.* **1986**, *25*, 4562.
- [87] R. Magnusson, S. Wang, *Appl. Phys. Lett.* **1992**, *61*, 1022.
- [88] S. Wang, R. Magnusson, *Appl. Opt.* **1993**, *32*, 2606.
- [89] W. J. Kim, B. K. Kim, A. Kim, C. Huh, C. S. Ah, K. H. Kim, J. Hong, S. H. Park, S. Song, J. Song, G. Y. Sung, *Anal. Chem.* **2010**, *82*, 9686.

- [90] D. U. Yildirim, A. Ghobadi, M. C. Soydan, M. Gokbayrak, A. Toprak, B. Butun, E. Ozbay, *J. Phys. Chem. C* **2019**, *123*, 19125.
- [91] A. Kenaan, K. Li, I. Barth, S. Johnson, J. Song, T. Krauss, presented at *Optics and Photonics for Sensing the Environment*, San Jose, California, June **2019**.
- [92] G. Quaranta, G. Basset, O. J. Martin, B. Gallinet, *Laser & Photonics Reviews* **2018**, *12*, 1800017.
- [93] X. Wei, S. M. Weiss, *Opt. Express* **2011**, *19*, 11330.
- [94] M. Maleki, M. Mehran, *J. Opt. Soc. Am. B* **2022**, *39*, 1634.
- [95] S. Joseph, S. Sarkar, J. Joseph, *IEEE Sens. J.* **2022**, *22*, 16856.
- [96] M. Bahramipanah, S. Dutta-Gupta, B. Abasahl, O. J. Martin, *ACS Nano* **2015**, *9*, 7621.
- [97] S. Sarkar, A. K. Ghosh, M. Adnan, O. Aftenieva, V. Gupta, A. Fery, J. Joseph, T. A. König, *Adv. Opt. Mater.* **2022**, *10*, 2200954.
- [98] P. Arora, E. Talker, N. Mazurski, U. Levy, *Sci. Rep.* **2018**, *8*, 9060.
- [99] R. Zia, M. D. Selker, M. L. Brongersma, *Phys. Rev. B* **2005**, *71*, 165431.
- [100] V. Marquez-Cruz, J. Albert, *J. Lightwave Technol.* **2015**, *33*, 3363.
- [101] D. Kotlarek, M. Vorobii, W. Ogielko, W. Knoll, C. Rodriguez-Emmenegger, J. Dostálek, *ACS Sens.* **2019**, *4*, 2109.
- [102] A. P. Hibbins, University of Exeter **2000**, British Library EThOS.
- [103] J. Homola, *Anal. Bioanal. Chem.* **2003**, *377*, 528.
- [104] A. Shalabney, I. Abdulhalim, *Laser Photonics Rev.* **2011**, *5*, 571.
- [105] M. Couture, Y. Liang, H.-P. P Richard, R. Faid, W. Peng, J.-F. Masson, *Nanoscale* **2013**, *5*, 12399.
- [106] A. Barik, L. M. Otto, D. Yoo, J. Jose, T. W. Johnson, S.-H. Oh, *Nano Lett.* **2014**, *14*, 2006.
- [107] M.-P. Murray-Méthot, M. Ratel, J.-F. Masson, *J. Phys. Chem. C* **2010**, *114*, 8268.
- [108] W. Kubo, S. Fujikawa, *Nano Lett.* **2011**, *11*, 8.
- [109] B. Zeng, Y. Gao, F. J. Bartoli, *Nanoscale* **2015**, *7*, 166.
- [110] P. Wang, M. E. Nasir, A. V. Krasavin, W. Dickson, Y. Jiang, A. V. Zayats, *Acc. Chem. Res.* **2019**, *52*, 3018.
- [111] J. Divya, S. Selvendran, A. S. Raja, A. Sivasubramanian, *Biosens. Bioelectron.: X* **2022**, *11*, 100175.
- [112] T. König, M. Weidemüller, A. Hemmerich, *Appl. Phys. B* **2008**, *93*, 545.
- [113] T. A. König, P. A. Ledin, M. Russell, J. A. Geldmeier, M. A. Mahmoud, M. A. El-Sayed, V. V. Tsukruk, *Nanoscale* **2015**, *7*, 5230.
- [114] K. L. Kelly, E. Coronado, L. L. Zhao, G. C. Schatz, *J. Phys. Chem. B* **2003**, *107*, 668.
- [115] V. Myroshnychenko, J. Rodríguez-Fernández, I. Pastoriza-Santos, A. M. Funston, C. Novo, P. Mulvaney, L. M. Liz-Marzán, F. J. G. De Abajo, *Chem. Soc. Rev.* **2008**, *37*, 1792.
- [116] D. W. Ball, J. A. Key, *Introductory Chemistry*, BCcampus, Victoria, British Columbia **2014**.
- [117] H. M. Abdulla, R. Thomas, R. S. Swathi, *J. Phys. Chem. C* **2018**, *122*, 7382.
- [118] E. Prodan, P. Nordlander, *J. Chem. Phys.* **2004**, *120*, 5444.
- [119] Y. Wu, P. Nordlander, *J. Chem. Phys.* **2006**, *125*, 124708.
- [120] P. Nordlander, C. Oubre, E. Prodan, K. Li, M. Stockman, *Nano Lett.* **2004**, *4*, 899.
- [121] S.-C. Yang, H. Kobori, C.-L. He, M.-H. Lin, H.-Y. Chen, C. Li, M. Kanehara, T. Teranishi, S. Gwo, *Nano Lett.* **2010**, *10*, 632.
- [122] P. K. Jain, S. Eustis, M. A. El-Sayed, *J. Phys. Chem. B* **2006**, *110*, 18243.
- [123] E. R. Encina, E. A. Coronado, *J. Phys. Chem. C* **2011**, *115*, 15908.
- [124] L. S. Slaughter, Y. Wu, B. A. Willingham, P. Nordlander, S. Link, *ACS Nano* **2010**, *4*, 4657.
- [125] S. Sheikholeslami, Y.-w. Jun, P. K. Jain, A. P. Alivisatos, *Nano Lett.* **2010**, *10*, 2655.
- [126] M. A. Basyooni, A. M. Ahmed, M. Shaban, *Optik* **2018**, *172*, 1069.
- [127] B. Willingham, D. Brandl, P. Nordlander, *Appl. Phys. B* **2008**, *93*, 209.
- [128] A. Aubry, D. Y. Lei, S. A. Maier, J. B. Pendry, *ACS Nano* **2011**, *5*, 3293.
- [129] Y. Zhang, J. Wang, J. Shen, Z. Man, W. Shi, C. Min, G. Yuan, S. Zhu, H. P. Urbach, X. Yuan, *Nano Lett.* **2014**, *14*, 6430.
- [130] S. Zhang, K. Bao, N. J. Halas, H. Xu, P. Nordlander, *Nano Lett.* **2011**, *11*, 1657.
- [131] A. Movsesyan, A. Muravitskaya, M. Castilla, S. Kostcheev, J. Proust, J. Plain, A.-L. Baudrion, R. Vincent, P.-M. Adam, *J. Phys. Chem. C* **2020**, *125*, 724.
- [132] W. Zhou, J. Y. Suh, Y. Hua, T. W. Odom, *J. Phys. Chem. C* **2013**, *117*, 2541.
- [133] S. Lal, S. Link, N. J. Halas, *Nat. Photonics* **2007**, *1*, 641.
- [134] H. Liao, C. L. Nehl, J. H. Hafner, *Nanomedicine* **2006**, *1*, 201.
- [135] M. Omrani, H. Mohammadi, H. Fallah, *Sci. Rep.* **2021**, *11*, 1.
- [136] J. Chen, B. Wiley, Z. Y. Li, D. Campbell, F. Saeki, H. Cang, L. Au, J. Lee, X. Li, Y. Xia, *Adv. Mater.* **2005**, *17*, 2255.
- [137] Z. A. Combs, S. T. Malak, T. König, M. A. Mahmoud, J. L. Chávez, M. A. El-Sayed, N. Kelley-Loughnane, V. V. Tsukruk, *Part. Part. Syst. Charact.* **2013**, *30*, 1071.
- [138] S. M. Kandil, I. A. Eshrah, I. S. El Babli, A. H. Badawi, *Opt. Express* **2016**, *24*, 30201.
- [139] W. Zhou, T. W. Odom, *Nat. Nanotechnol.* **2011**, *6*, 423.
- [140] Y. Shen, J. Zhou, T. Liu, Y. Tao, R. Jiang, M. Liu, G. Xiao, J. Zhu, Z.-K. Zhou, X. Wang, *Nat. Commun.* **2013**, *4*, 2381.
- [141] R. Magnusson, D. Wawro, S. Zimmerman, Y. Ding, M. Shokoh-Saremi, K. J. Lee, D. Ussery, S. Kim, S. H. Song, *Proc. SPIE* **2010**, *7604*, 143.
- [142] W. Wang, M. Ramezani, A. I. Väkeväinen, P. Törmä, J. G. Rivas, T. W. Odom, *Mater. Today* **2018**, *21*, 303.
- [143] B. Wang, P. Yu, W. Wang, X. Zhang, H.-C. Kuo, H. Xu, Z. M. Wang, *Adv. Opt. Mater.* **2021**, *9*, 2001520.
- [144] K. Yang, X. Yao, B. Liu, B. Ren, *Adv. Mater.* **2021**, *33*, 2007988.
- [145] A. D. Utushev, V. I. Zakomirnyi, I. L. Rasskazov, *Rev. Phys.* **2021**, *6*, 100051.
- [146] R. R. Gutha, S. M. Sadeghi, C. Sharp, W. J. Wing, *Nanotechnology* **2017**, *28*, 355504.
- [147] Y. Chu, E. Schonbrun, T. Yang, K. B. Crozier, *Appl. Phys. Lett.* **2008**, *93*, 181108.
- [148] V. Kravets, F. Schedin, A. Grigorenko, *Phys. Rev. Lett.* **2008**, *101*, 087403.
- [149] S. Buzzi, M. Galli, M. Agio, J. F. Löffler, *Appl. Phys. Lett.* **2009**, *94*, 223115.
- [150] S. Deng, R. Li, J.-E. Park, J. Guan, P. Choo, J. Hu, P. J. Smeets, T. W. Odom, *Proc. Natl. Acad. Sci. USA* **2020**, *117*, 23380.
- [151] M. S. Bin-Alam, O. Reshef, Y. Mamchur, M. Z. Alam, G. Carlow, J. Upham, B. T. Sullivan, J.-M. Ménard, M. J. Huttunen, R. W. Boyd, *Nat. Commun.* **2021**, *12*, 974.
- [152] G. Lozano, G. Grzela, M. A. Verschuuren, M. Ramezani, J. G. Rivas, *Nanoscale* **2014**, *6*, 9223.
- [153] J. Zheng, W. Yang, J. Wang, J. Zhu, L. Qian, Z. Yang, *Nanoscale* **2019**, *11*, 4061.
- [154] D. Wang, M. R. Bourgeois, W.-K. Lee, R. Li, D. Trivedi, M. P. Knudson, W. Wang, G. C. Schatz, T. W. Odom, *Nano Lett.* **2018**, *18*, 4549.
- [155] W. Zhou, M. Dridi, J. Y. Suh, C. H. Kim, D. T. Co, M. R. Wasielewski, G. C. Schatz, T. W. Odom, *Nat. Nanotechnol.* **2013**, *8*, 506.
- [156] S. Kasani, K. Curtin, N. Wu, *Nanophotonics* **2019**, *8*, 2065.
- [157] R. R. Gutha, S. M. Sadeghi, W. J. Wing, *Appl. Phys. Lett.* **2017**, *110*, 153103.
- [158] M. Kularia, O. Aftenieva, S. Sarkar, A. M. Steiner, V. Gupta, A. Fery, J. Joseph, M. A. Schmidt, T. A. König, *J. Polym. Sci.* **2023**, <https://doi.org/10.1002/pol.20230024>.
- [159] S. Sadeghi, W. Wing, Q. Campbell, *J. Appl. Phys.* **2016**, *119*, 244503.
- [160] A. Yang, T. B. Hoang, M. Dridi, C. Deep, M. H. Mikkelsen, G. C. Schatz, T. W. Odom, *Nat. Commun.* **2015**, *6*, 6939.
- [161] A. D. Humphrey, N. Meinzer, T. A. Starkey, W. L. Barnes, *ACS Photonics* **2016**, *3*, 634.

- [162] A. Yang, A. J. Hryni, M. R. Bourgeois, W.-K. Lee, J. Hu, G. C. Schatz, T. W. Odom, *Proc. Natl. Acad. Sci. USA* **2016**, *113*, 14201.
- [163] S. Zou, N. Janel, G. C. Schatz, *J. Chem. Phys.* **2004**, *120*, 10871.
- [164] B. Auguié, W. L. Barnes, *Phys. Rev. Lett.* **2008**, *101*, 143902.
- [165] L. Lin, Y. Zheng, *Nanoscale* **2015**, *7*, 12205.
- [166] V. G. Kravets, A. V. Kabashin, W. L. Barnes, A. N. Grigorenko, *Chem. Rev.* **2018**, *118*, 5912.
- [167] B. Auguié, W. L. Barnes, *Opt. Lett.* **2009**, *34*, 401.
- [168] A. D. Humphrey, W. L. Barnes, *Phys. Rev. B* **2014**, *90*, 075404.
- [169] R. Guo, T. K. Hakala, P. Törmä, *Phys. Rev. B* **2017**, *95*, 155423.
- [170] A. Väkeväinen, R. Moerland, H. Rekola, A.-P. Eskelinen, J.-P. Martikainen, D.-H. Kim, P. Törmä, *Nano Lett.* **2014**, *14*, 1721.
- [171] W. Liu, B. Lee, C. H. Naylor, H.-S. Ee, J. Park, A. C. Johnson, R. Agarwal, *Nano Lett.* **2016**, *16*, 1262.
- [172] S. Baur, S. Sanders, A. Manjavacas, *ACS Nano* **2018**, *12*, 1618.
- [173] S. D. Liu, P. Yue, S. Zhang, M. Wang, H. Dai, Y. Chen, Z. Q. Nie, Y. Cui, J. B. Han, H. Duan, *Adv. Opt. Mater.* **2020**, *8*, 1901109.
- [174] S. Linden, J. Kuhl, H. Giessen, *Phys. Rev. Lett.* **2001**, *86*, 4688.
- [175] A. Christ, S. Tikhodeev, N. Gippius, J. Kuhl, H. Giessen, *Phys. Status Solidi C* **2003**, *0*, 1393.
- [176] K. Schubert, J. Kuhl, H. Giessen, *Phys. Status Solidi C* **2003**, *0*, 1412.
- [177] A. Christ, S. Tikhodeev, N. Gippius, J. Kuhl, H. Giessen, *Phys. Rev. Lett.* **2003**, *91*, 183901.
- [178] A. Christ, T. Zentgraf, J. Kuhl, S. Tikhodeev, N. Gippius, H. Giessen, *Phys. Rev. B* **2004**, *70*, 125113.
- [179] M. Klein, T. Tritschler, M. Wegener, S. Linden, *Phys. Rev. B* **2005**, *72*, 115113.
- [180] S. G. Tikhodeev, N. A. Gippius, A. Christ, T. Zentgraf, J. Kuhl, H. Giessen, *Phys. Status Solidi C* **2005**, *2*, 795.
- [181] H. Guo, D. Nau, A. Radke, X. Zhang, J. Stodolka, X. Yang, S. Tikhodeev, N. Gippius, H. Giessen, *Appl. Phys. B* **2005**, *81*, 271.
- [182] X. Zhang, B. Sun, R. H. Friend, H. Guo, D. Nau, H. Giessen, *Nano Lett.* **2006**, *6*, 651.
- [183] S. Rodriguez, S. Murai, M. Verschueren, J. G. Rivas, *Phys. Rev. Lett.* **2012**, *109*, 166803.
- [184] C. Ng, S. Dligatch, H. Amekura, T. J. Davis, D. E. Gómez, *Adv. Opt. Mater.* **2015**, *3*, 1582.
- [185] P. Zeng, J. Cadusch, D. Chakraborty, T. A. Smith, A. Roberts, J. E. Sader, T. J. Davis, D. E. Gómez, *Nano Lett.* **2016**, *16*, 2651.
- [186] J. Geldmeier, T. König, M. A. Mahmoud, M. A. El-Sayed, V. V. Tsukruk, *Adv. Funct. Mater.* **2014**, *24*, 6797.
- [187] S.-m. Kim, W. Zhang, B. T. Cunningham, *Opt. Express* **2010**, *18*, 4300.
- [188] J.-N. Liu, Q. Huang, K.-K. Liu, S. Singamaneni, B. T. Cunningham, *Nano Lett.* **2017**, *17*, 7569.
- [189] C. Hanske, M. Tebbe, C. Kuttner, V. Bieber, V. V. Tsukruk, M. Chanana, T. A. König, A. Fery, *Nano Lett.* **2014**, *14*, 6863.
- [190] S. J. Barrow, D. Rossouw, A. M. Funston, G. A. Botton, P. Mulvaney, *Nano Lett.* **2014**, *14*, 3799.
- [191] M. Mueller, M. Tebbe, D. V. Andreeva, M. Karg, R. A. Alvarez Puebla, N. P Perez, A. Fery, *Langmuir* **2012**, *28*, 9168.
- [192] L. S. Slaughter, B. A. Willingham, W.-S. Chang, M. H. Chester, N. Ogden, S. Link, *Nano Lett.* **2012**, *12*, 3967.
- [193] A. M. Steiner, M. Mayer, M. Seuss, S. Nikolov, K. D. Harris, A. Alexeev, C. Kuttner, T. A. König, A. Fery, *ACS Nano* **2017**, *11*, 8871.
- [194] M. Tebbe, M. Mayer, B. A. Glatz, C. Hanske, P. T. Probst, M. B. Müller, M. Karg, M. Chanana, T. A. König, C. Kuttner, *Faraday Discuss.* **2015**, *181*, 243.
- [195] O. Aftenieva, M. Schnepf, B. Mehlhorn, T. A. König, *Adv. Opt. Mater.* **2021**, *9*, 2001280.
- [196] P. T. Probst, M. Mayer, V. Gupta, A. M. Steiner, Z. Zhou, G. K. Auernhammer, T. A. König, A. Fery, *Nat. Mater.* **2021**, *20*, 1024.
- [197] V. Canalejas-Tejero, A. López, R. Casquel, M. Holgado, C. A. Barrios, *Sens. Actuators, B* **2016**, *226*, 204.
- [198] A. Mizutani, S. Urakawa, H. Kikuta, *Appl. Opt.* **2015**, *54*, 4161.
- [199] S.-F. Lin, C.-M. Wang, T.-J. Ding, Y.-L. Tsai, T.-H. Yang, W.-Y. Chen, J.-Y. Chang, *Opt. Express* **2012**, *20*, 14584.
- [200] V. Pandey, S. Pal, *IEEE Sens. J.* **2019**, *19*, 4412.
- [201] C. Tan, J. Simonen, T. Niemi, *Opt. Commun.* **2012**, *285*, 4381.
- [202] S. I. Azzam, V. M. Shalaev, A. Boltasseva, A. V. Kildishev, *Phys. Rev. Lett.* **2018**, *121*, 253901.
- [203] A. L. Fannin, B. R. Wenner, J. W. Allen, M. S. Allen, R. Magnusson, *Opt. Eng.* **2017**, *56*, 121905.
- [204] L. Wang, T. Sang, J. Gao, X. Yin, H. Qi, *Appl. Opt.* **2018**, *57*, 7338.
- [205] L. Qian, K. Wang, W. Zhu, C. Han, C. Yan, *Opt. Commun.* **2019**, *452*, 273.
- [206] X. Li, D. Han, F. Wu, C. Xu, X. Liu, J. Zi, *J. Phys.: Condens. Matter* **2008**, *20*, 485001.
- [207] L. Qian, T. Gu, S. Xu, X. Zhang, K. Wang, *Opt. Express* **2023**, *31*, 1844.
- [208] R. Hu, Y. Liang, S. Qian, W. Peng, *Opt. Commun.* **2015**, *336*, 110.
- [209] Y. Ren, X. Guo, G. Zhang, A. V. Balakin, A. P. Shkurinov, A. Yu, Y. Zhu, *Opt. Express* **2020**, *28*, 13224.
- [210] M. E. Stewart, N. H. Mack, V. Malyarchuk, J. A. Soares, T.-W. Lee, S. K. Gray, R. G. Nuzzo, J. A. Rogers, *Proc. Natl. Acad. Sci. USA* **2006**, *103*, 17143.
- [211] H. Gao, J. McMahon, M. Lee, J. Henzie, S. Gray, G. Schatz, T. Odom, *Opt. Express* **2009**, *17*, 2334.
- [212] C. Vieu, F. Carcenac, A. Pepin, Y. Chen, M. Mejias, A. Lebib, L. Manin-Ferlazzo, L. Couraud, H. Launois, *Appl. Surf. Sci.* **2000**, *164*, 111.
- [213] J. C. Hulteen, R. P. Van Duyne, *J. Vac. Sci. Technol., A* **1995**, *13*, 1553.
- [214] C. Lu, R. Lipson, *Laser Photonics Rev.* **2010**, *4*, 568.
- [215] F. Hua, Y. Sun, A. Gaur, M. A. Meitl, L. Bilhaut, L. Rotkina, J. Wang, P. Geil, M. Shim, J. A. Rogers, *Nano Lett.* **2004**, *4*, 2467.
- [216] K. Arshak, M. Mihov, *J. Optoelectron. Adv. Mater.* **2005**, *7*, 193.
- [217] C. A. Mirkin, *ACS Nano* **2007**, *1*, 79.
- [218] M. Deubel, G. Von Freymann, M. Wegener, S. Pereira, K. Busch, C. M. Soukoulis, *Nat. Mater.* **2004**, *3*, 444.
- [219] J. Bekesi, J. Meinertz, J. Ihlemann, P. Simon, *Appl. Phys. A* **2008**, *93*, 27.
- [220] M. J. Madou, *Manufacturing Techniques for Microfabrication and Nanotechnology*, CRC Press, Boca Raton, FL **2011**.
- [221] N. Jiang, *Microelectron. Eng.* **2017**, *168*, 41.
- [222] A. Broers, W. Molzen, J. Cuomo, N. Wittels, *Appl. Phys. Lett.* **1976**, *29*, 596.
- [223] A. Broers, J. Harper, W. Molzen, *Appl. Phys. Lett.* **1978**, *33*, 392.
- [224] K. Yamazaki, H. Namatsu, *Jpn. J. Appl. Phys.* **2004**, *43*, 3767.
- [225] M. Isaacson, A. Muray, *J. Vac. Sci. Technol.* **1981**, *19*, 1117.
- [226] G. Lérondel, S. Kostcheev, J. Plain, in *Plasmonics: From Basics to Advanced Topics*, Springer Series in Optical Sciences, Vol. 167 (Eds: S. Enoch, N. Bonod), Springer, Berlin **2012**, pp. 269–316.
- [227] Australian National Fabrication Facility, Electron Beam Lithography, [https://anff.act.anu.edu.au/HTML/HTM\\_old/detail/EBL.htm#Top](https://anff.act.anu.edu.au/HTML/HTM_old/detail/EBL.htm#Top) (accessed: March **2023**).
- [228] A.-P. Blanchard-Dionne, M. Meunier, *J. Vac. Sci. Technol., B: Nanotech. Microelectron.: Mater., Process., Meas., Phenom.* **2015**, *33*, 061602.
- [229] H. Deckman, J. Dunsmuir, *Appl. Phys. Lett.* **1982**, *41*, 377.
- [230] A. S. Dimitrov, K. Nagayama, *Langmuir* **1996**, *12*, 1303.
- [231] C. Wang, M. Shim, P. Guyot-Sionnest, *Appl. Phys. Lett.* **2002**, *80*, 4.
- [232] O. Aftenieva, M. Sudzius, A. Prudnikau, M. Adnan, S. Sarkar, V. Lesnyak, K. Leo, A. Fery, T. A. König, *Adv. Opt. Mater.* **2023**, *11*, 2202226.
- [233] M. Wahle, K. Brassat, J. Ebel, J. Bürger, J. K. Lindner, H.-S. Kitzerow, *Opt. Express* **2017**, *25*, 22608.
- [234] J. C. Hulteen, D. A. Treichel, M. T. Smith, M. L. Duval, T. R. Jensen, R. P. Van Duyne, *J. Phys. Chem. B* **1999**, *103*, 3854.
- [235] H. Yabu, *Langmuir* **2013**, *29*, 1005.

- [236] M. Maldovan, E. L. Thomas, *Periodic Materials and Interference Lithography: For Photonics, Phononics and Mechanics*, John Wiley & Sons, New York 2009.
- [237] A. Rodriguez, M. Echeverría, M. Ellman, N. Perez, Y. K. Verevkin, C. S. Peng, T. Berthou, Z. Wang, I. Ayerdi, J. Savall, *Microelectron. Eng.* **2009**, 86, 937.
- [238] M. Campbell, D. Sharp, M. Harrison, R. Denning, A. Turberfield, *Nature* **2000**, 404, 53.
- [239] L. Cai, X. Yang, Y. Wang, *J. Opt. Soc. Am. A* **2002**, 19, 2238.
- [240] Y. K. Pang, J. C. W. Lee, C. T. Ho, W. Y. Tam, *Opt. Express* **2006**, 14, 9013.
- [241] S. Sarkar, J. Joseph, *Proc. SPIE* **2020**, 11402, 38.
- [242] S. Sarkar, K. Samanta, J. Joseph, *J. Opt.* **2020**, 22, 085105.
- [243] S. Behera, S. Sarkar, J. Joseph, *Opt. Lett.* **2018**, 43, 106.
- [244] S. Sarkar, K. Samanta, J. Joseph, *Opt. Express* **2020**, 28, 4347.
- [245] S. Y. Chou, P. R. Krauss, P. J. Renstrom, *Appl. Phys. Lett.* **1995**, 67, 3114.
- [246] S. Y. Chou, P. R. Krauss, *Microelectron. Eng.* **1997**, 35, 237.
- [247] M. Cottat, N. Lidgi-Guigui, I. Tijunelyte, G. Barbillon, F. Hamouda, P. Gogol, A. Aassime, J.-M. Lourtioz, B. Bartenlian, M. L. de la Chapelle, *Nanoscale Res. Lett.* **2014**, 9, 623.
- [248] J. Chen, Y. Li, K. Huang, P. Wang, L. He, K. R. Carter, S. R. Nugen, *ACS Appl. Mater. Interfaces* **2015**, 7, 22106.
- [249] M. Colburn, S. C. Johnson, M. D. Stewart, S. Damle, T. C. Bailey, B. Choi, M. Wedlake, T. B. Michaelson, S. Sreenivasan, J. G. Ekerdt, *Proc. SPIE* **1999**, 3676, 379.
- [250] M. Modaresialam, Z. Chehadi, T. Bottein, M. Abbarchi, D. Gross, *Chem. Mater.* **2021**, 33, 5464.
- [251] C. Valsecchi, L. E. Gomez Armas, J. Weber de Menezes, *Sensors* **2019**, 19, 2182.
- [252] H. Y. Jung, S. Y. Hwang, B. J. Bae, H. Lee, *J. Vac. Sci. Technol., B: Nanotechnol. Microelectron.: Mater., Process., Meas., Phenom.* **2009**, 27, 1861.
- [253] A. Cattoni, J. Chen, D. Decanini, J. Shi, A.-M. Haghiri-Gosnet, in *Recent Advances in Nanofabrication Techniques and Applications* (Ed: B. Cui), IntechOpen, London **2011**, p. 139.
- [254] J. A. Rogers, R. G. Nuzzo, *Mater. Today* **2005**, 8, 50.
- [255] Y. Nazirizadeh, F. von Oertzen, K. Plewa, N. Barié, P.-J. Jakobs, M. Guttmann, H. Leiste, M. Gerken, *Opt. Mater. Express* **2013**, 3, 556.
- [256] M. D. Fagan, B. H. Kim, D. Yao, *Adv. Polym. Technol.* **2009**, 28, 246.
- [257] M. M. Greve, T. O. Håvardstun, B. Holst, *J. Vac. Sci. Technol., B: Nanotechnol. Microelectron.: Mater., Process., Meas., Phenom.* **2013**, 31, 06F410.
- [258] M. Rahaman, S. Moras, L. He, T. I. Madeira, D. R. T. Zahn, *J. Appl. Phys.* **2020**, 128, 233104.
- [259] J. Martinez-Perdigero, A. Retolaza, D. Otaduy, A. Juarros, S. Merino, *Sensors* **2013**, 13, 13960.
- [260] F. López-Tejeira, S. G. Rodrigo, L. Martín-Moreno, F. J. García-Vidal, E. Devaux, T. W. Ebbesen, J. R. Krenn, I. Radko, S. I. Bozhevolnyi, M. U. González, *Nat. Phys.* **2007**, 3, 324.
- [261] W. Yue, Z. Wang, Y. Yang, L. Chen, A. Syed, K. Wong, X. Wang, *J. Micromech. Microeng.* **2012**, 22, 125007.
- [262] E. Menumerov, S. D. Golze, R. A. Hughes, S. Neretina, *Nanoscale* **2018**, 10, 18186.
- [263] K. Ueno, S. Juodkazis, V. Mizeikis, K. Sasaki, H. Misawa, *J. Am. Chem. Soc.* **2006**, 128, 14226.
- [264] P. Zheng, H. Tang, B. Liu, S. Kasani, L. Huang, N. Wu, *Nano Res.* **2019**, 12, 63.
- [265] P. Zheng, S. K. Cushing, S. Suri, N. Wu, *Phys. Chem. Chem. Phys.* **2015**, 17, 21211.
- [266] L. E. G. Armas, J. W. Menezes, M. Huila, K. Araki, H. E. Toma, *Plasmonics* **2017**, 12, 1015.
- [267] S. Kasani, P. Zheng, N. Wu, *J. Phys. Chem. C* **2017**, 122, 13443.
- [268] D. Eschimese, F. Vaurette, D. Troadec, G. Leveque, T. Melin, S. Arscott, *Sci. Rep.* **2019**, 9, 7682.
- [269] P. Zheng, S. Kasani, N. Wu, *Nanoscale Horiz.* **2019**, 4, 516.
- [270] V. S. Volkov, S. I. Bozhevolnyi, E. Devaux, J.-Y. Laluet, T. W. Ebbesen, *Nano Lett.* **2007**, 7, 880.
- [271] H. C. Jeon, T. Y. Jeon, T. S. Shim, S. M. Yang, *Small* **2014**, 10, 1490.
- [272] B. Liu, X. Yao, S. Chen, H. Lin, Z. Yang, S. Liu, B. Ren, *Adv. Funct. Mater.* **2018**, 28, 1802263.
- [273] A. K. Ghosh, S. Sarkar, L. J. Nebel, O. Aftenieva, V. Gupta, O. Sander, A. Das, J. Joseph, S. Wießner, T. A. König, *Adv. Funct. Mater.* **2021**, 31, 2101959.
- [274] A. K. Ghosh, S. Sarkar, T. Tsuda, S. Chae, A. Knapp, M. Nitschke, A. Das, S. Wießner, T. A. König, A. Fery, *Adv. Funct. Mater.* **2023**, 33, 2210172.
- [275] J. P. Schmidt, S. E. Cross, S. K. Buratto, *J. Chem. Phys.* **2004**, 121, 10657.
- [276] D. Distler, in *Encyclopedia of Materials: Science and Technology* (Eds: K. H. J. Buschow, R. W. Cahn, M. C. Flemings, B. Ilsschner, E. J. Kramer, S. Mahajan, P. Veyssiére), Elsevier, Amsterdam **2001**, p. 2769.
- [277] G. Urbina-Villalba, J. Toro-Mendoza, A. Lozsán, M. García-Sucre, in *Interface Science and Technology* (Ed: D. N. Petsev), Vol. 4, Elsevier, Amsterdam **2004**, p. 677.
- [278] S. J. Tan, M. J. Campolongo, D. Luo, W. Cheng, *Nat. Nanotechnol.* **2011**, 6, 268.
- [279] Y. Yin, Y. Lu, B. Gates, Y. Xia, *J. Am. Chem. Soc.* **2001**, 123, 8718.
- [280] J. Zhang, Y. Li, X. Zhang, B. Yang, *Adv. Mater.* **2010**, 22, 4249.
- [281] M. R. Jones, K. D. Osberg, R. J. Macfarlane, M. R. Langille, C. A. Mirkin, *Chem. Rev.* **2011**, 111, 3736.
- [282] R. van Dommelen, P. Fanzio, L. Sasso, *Adv. Colloid Interface Sci.* **2018**, 251, 97.
- [283] C. Hamon, L. M. Liz-Marzán, *Chemistry* **2015**, 21, 9956.
- [284] R. A. Hughes, E. Menumerov, S. Neretina, *Nanotechnology* **2017**, 28, 282002.
- [285] C. Kuemin, L. Nowack, L. Bozano, N. D. Spencer, H. Wolf, *Adv. Funct. Mater.* **2012**, 22, 702.
- [286] V. Flauraud, M. Mastrangeli, G. D. Bernasconi, J. Butet, D. T. Alexander, E. Shahrai, O. J. Martin, J. Brugger, *Nat. Nanotechnol.* **2017**, 12, 73.
- [287] P. Offermans, M. C. Schaafsma, S. R. Rodriguez, Y. Zhang, M. Crego-Calama, S. H. Brongersma, J. Gómez Rivas, *ACS Nano* **2011**, 5, 5151.
- [288] V. Kravets, F. Schedin, A. Kabashin, A. Grigorenko, *Opt. Lett.* **2010**, 35, 956.
- [289] B. Špačková, J. Homola, *Opt. Express* **2013**, 21, 27490.
- [290] Y. Du, L. Shi, M. Hong, H. Li, D. Li, M. Liu, *Opt. Commun.* **2013**, 298, 232.
- [291] F. Liu, X. Zhang, *Biosens. Bioelectron.* **2015**, 68, 719.
- [292] M. Eitan, Z. Iluz, Y. Yifat, A. Boag, Y. Hanein, J. Scheuer, *ACS Photonics* **2015**, 2, 615.
- [293] R. W. Wood, *London, Edinburgh Dublin Philos. Mag. J. Sci.* **1902**, 4, 396.
- [294] X. Liu, J. Wang, J. Gou, C. Ji, G. Cui, *Nanoscale Res. Lett.* **2018**, 13, 1.
- [295] K. Akiyoshi, Y. Y. Tanaka, T. Ishida, T. Shimura, T. Tatsuma, *ACS Appl. Nano Mater.* **2018**, 1, 5994.
- [296] J. Becker, A. Trügler, A. Jakab, U. Hohenester, C. Sönnichsen, *Plasmonics* **2010**, 5, 161.
- [297] B. D. Thackray, V. G. Kravets, F. Schedin, G. Auton, P. A. Thomas, A. N. Grigorenko, *ACS Photonics* **2014**, 1, 1116.
- [298] R. Adato, A. A. Yarik, J. J. Armsden, D. L. Kaplan, F. G. Ornenetto, M. K. Hong, S. Erramilli, H. Altug, *Proc. Natl. Acad. Sci. USA* **2009**, 106, 19227.
- [299] R. R. Gutha, S. M. Sadeghi, A. Hatef, C. Sharp, Y. Lin, *Appl. Phys. Lett.* **2018**, 112, 223102.

- [300] X. Zhang, S. Feng, J. Zhang, T. Zhai, H. Liu, Z. Pang, *Sensors* **2012**, 12, 12082.
- [301] D. Nau, A. Seidel, R. Orzekowsky, S.-H. Lee, S. Deb, H. Giessen, *Opt. Lett.* **2010**, 35, 3150.
- [302] T. J. Palinski, G. W. Hunter, A. Tadimety, J. X. Zhang, *Opt. Express* **2019**, 27, 16344.
- [303] C. Bauer, H. Giessen, *Nanophotonics* **2020**, 9, 523.
- [304] S. Murai, E. Cabello-Olmo, R. Kamakura, M. E. Calvo, G. Lozano, T. Atsumi, H. n. Míguez, K. Tanaka, *J. Phys. Chem. C* **2020**, 124, 5772.
- [305] B. Winzek, V. Emelianov, A. Radke, H. Guo, D. Nau, H. Giessen, presented at Photonic Crystals and Fibers, Congress on Optics and Optoelectronics, Warsaw, Poland, October **2005**.
- [306] N. Li, T. D. Canady, Y. Lu, M. Kohli, A. M. Smith, B. T. Cunningham, presented at Optical Sensors, Washington DC, United States, June **2020**.
- [307] L. Polavarapu, J. Pérez-Juste, Q.-H. Xu, L. M. Liz-Marzán, *J. Mater. Chem. C* **2014**, 2, 7460.
- [308] D. Solis Jr, B. Willingham, S. L. Nauert, L. S. Slaughter, J. Olson, P. Swanglap, A. Paul, W.-S. Chang, S. Link, *Nano Lett.* **2012**, 12, 1349.
- [309] T. König, R. Kodiyath, Z. A. Combs, M. A. Mahmoud, M. A. El-Sayed, V. V. Tsukruk, *Part. Part. Syst. Charact.* **2014**, 31, 274.
- [310] T. Sun, W. Song, Z. Qin, W. Guo, P. Wangyang, Z. Zhou, Y. Deng, *Photonics* **2023**, 10, 60.
- [311] X. Kaichen, Z. Chentao, L. T. Hsiao, W. Puqun, Z. Rui, J. Rong, H. Minghui, *Guangdian Gongcheng* **2017**, 44, 185.
- [312] D. Nandi, M. Z. Islam, M. Gupta, *J. Opt. Soc. Am. B* **2022**, 39, 2705.
- [313] P. Sun, C. Zhou, W. Jia, J. Wang, C. Xiang, Y. Xie, D. Zhao, *J. Phys. D: Appl. Phys.* **2020**, 53, 145101.
- [314] D. Y. Lei, J. Li, A. I. Fernández-Domínguez, H. C. Ong, S. A. Maier, *ACS Nano* **2010**, 4, 432.
- [315] M. Vala, C. T. Ertsgaard, N. J. Wittenberg, S.-H. Oh, *ACS Sens.* **2019**, 4, 3265.
- [316] B. Liu, S. Chen, J. Zhang, X. Yao, J. Zhong, H. Lin, T. Huang, Z. Yang, J. Zhu, S. Liu, *Adv. Mater.* **2018**, 30, 1706031.
- [317] X. Ao, D. Wang, T. W. Odom, *ACS Photonics* **2019**, 6, 2612.
- [318] X. Ao, X. Xu, J. Dong, S. He, *ACS Appl. Mater. Interfaces* **2018**, 10, 34817.
- [319] Y. Wang, L. Xiong, M. Tian, G. Li, *Appl. Opt.* **2021**, 60, 11205.
- [320] W.-K. Kuo, J. Tongpakpanang, P.-H. Kuo, S.-F. Kuo, *Opt. Express* **2019**, 27, 3867.
- [321] M. Abutoama, I. Abdulhalim, *Opt. Express* **2015**, 23, 28667.
- [322] S. Joseph, S. Sarkar, J. Joseph, presented at 2020 5th IEEE International Conference on Emerging Electronics (ICEE), New Delhi, India, November **2020**.
- [323] S. Joseph, S. Pandey, S. Sarkar, J. Joseph, *Nanophotonics* **2021**, 10, 4175.
- [324] S. Pandey, N. Baburaj, S. Joseph, J. Joseph, *ISSS J Micro Smart Syst.* **2022**, 11, 113.
- [325] S. Joseph, S. Sarkar, S. Khan, J. Joseph, *Adv. Opt. Mater.* **2021**, 9, 2001895.
- [326] R. Ameling, L. Langguth, M. Hentschel, M. Mesch, P. V. Braun, H. Giessen, *Appl. Phys. Lett.* **2010**, 97, 253116.
- [327] M. Hentschel, M. Saliba, R. Vogelgesang, H. Giessen, A. P. Alivisatos, N. Liu, *Nano Lett.* **2010**, 10, 2721.
- [328] N. A. Mirin, K. Bao, P. Nordlander, *J. Phys. Chem. A* **2009**, 113, 4028.
- [329] C.-Y. Chen, I.-W. Un, N.-H. Tai, T.-J. Yen, *Opt. Express* **2009**, 17, 15372.
- [330] N. Liu, T. Weiss, M. Mesch, L. Langguth, U. Eigenthaler, M. Hirscher, C. Sonnichsen, H. Giessen, *Nano Lett.* **2010**, 10, 1103.
- [331] A. E. Cetin, H. Altug, *ACS Nano* **2012**, 6, 9989.
- [332] N. Kongsuwan, A. Demetriadou, R. Chikkaraddy, J. J. Baumberg, O. Hess, *EPJ Appl. Metamat.* **2018**, 5, 6.
- [333] G.-C. Li, Y.-L. Zhang, J. Jiang, Y. Luo, D. Y. Lei, *ACS Nano* **2017**, 11, 3067.
- [334] D. O. Sigle, S. Kasera, L. O. Herrmann, A. Palma, B. de Nijs, F. Benz, S. Mahajan, J. J. Baumberg, O. A. Scherman, *J. Phys. Chem. Lett.* **2016**, 7, 704.
- [335] M. Bahramipanah, S. Dutta-Gupta, B. Abasahl, O. J. F. Martin, *ACS Nano* **2015**, 9, 7621.
- [336] B. Luk'Yanchuk, N. I. Zheludev, S. A. Maier, N. J. Halas, P. Nordlander, H. Giessen, C. T. Chong, *Nat. Mater.* **2010**, 9, 707.
- [337] D. Dregely, M. Hentschel, H. Giessen, *ACS Nano* **2011**, 5, 8202.
- [338] M. Rahmani, B. Luk'yanchuk, M. Hong, *Laser Photonics Rev.* **2013**, 7, 329.
- [339] J. Ye, F. Wen, H. Sobhani, J. B. Lassiter, P. Van Dorpe, P. Nordlander, N. J. Halas, *Nano Lett.* **2012**, 12, 1660.
- [340] F. Hao, P. Nordlander, Y. Sonnenfeld, P. V. Dorpe, S. A. Maier, *ACS Nano* **2009**, 3, 643.
- [341] K.-H. Su, Q.-H. Wei, X. Zhang, J. Mock, D. R. Smith, S. Schultz, *Nano Lett.* **2003**, 3, 1087.
- [342] R. Chikkaraddy, B. de Nijs, F. Benz, S. J. Barrow, O. A. Scherman, E. Rosta, A. Demetriadou, P. Fox, O. Hess, J. J. Baumberg, *Nature* **2016**, 535, 127.
- [343] J.-S. G. Bouillard, W. Dickson, D. P. O'Connor, G. A. Wurtz, A. V. Zayats, *Nano Lett.* **2012**, 12, 1561.
- [344] P. Alabella, B. Garcia-Cueto, F. González, F. Moreno, P. C. Wu, T.-H. Kim, A. Brown, Y. Yang, H. O. Everitt, G. Videen, *Nano Lett.* **2011**, 11, 3531.
- [345] A. Amirjani, E. Rahbarimehr, *Microchim. Acta* **2021**, 188, 57.
- [346] B. I. Karawdeniya, A. M. Damry, K. Murugappan, S. Manjunath, Y. N. D. Bandara, C. J. Jackson, A. Tricoli, D. Neshev, *Chem. Rev.* **2022**, 122, 14990.
- [347] J. Grandidier, G. C. Des Francs, S. Massenot, A. Bouhelier, L. Markey, J.-C. Weeber, C. Finot, A. Dereux, *Nano Lett.* **2009**, 9, 2935.
- [348] J. Cai, Y. J. Zhou, Y. Zhang, Q. Y. Li, *Opt. Express* **2018**, 26, 25460.
- [349] O. Aftenieva, J. Brunner, M. Adnan, S. Sarkar, A. Fery, Y. Vaynzof, T. A. König, *ACS Nano* **2023**, 17, 2399.
- [350] A. P. Alivisatos, *J. Phys. Chem.* **1996**, 100, 13226.
- [351] A. M. Smith, S. Nie, *Acc. Chem. Res.* **2010**, 43, 190.



**Swagato Sarkar** is a researcher at Leibniz Institute for Polymer Research Dresden (IPF Dresden). He received his M.Sc. from the Indian Institute of Technology Madras (Department of Physics, 2014) and his Ph.D. from the Indian Institute of Technology Delhi (Department of Physics, 2021). During the Ph.D. program, Swagato went to IPF Dresden as a guest scientist for two years in 2018 and 2020. Since 2021, he has been a postdoctoral researcher in the research group König (King's Lab). His area of research includes photonic crystals and metamaterials, 1D and 2D subwavelength grating-based structures, colloidal plasmonics, and hybrid opto-plasmonic designs for sensing and light harvesting.



**Tobias A.F. König** is a Freigeist-fellow and an independent research group leader at the IPF Dresden and Privatdozent at the Technical University Dresden, which is equivalent to an Assistant Professor. He received his Diploma from the University of Hamburg (Institute for Laser Physics, 2008) and his Ph.D. from the University of Freiburg (Institute of Microsystems Engineering, 2011). He then worked as a post-doctoral researcher at Georgia Tech, Atlanta, USA (School of Materials Science and Engineering, 2014) and the University of Bayreuth (Institute of Physical Chemistry, 2015). His research focuses on the large-scale self-assembly of nanoscaled colloids and their characterization, using electromagnetic simulation and spectroscopic methods for nanophotonic applications.